A method for validating a transperineal ultrasound system for intrafraction monitoring of the prostate during external beam radiotherapy

Author: Stephen Gibson

The University of Adelaide

Faculty of Sciences

Submission Date

15th of March 2019

Table of Contents

A method for validating a transperineal ultrasound system for intrafraction monitoring of the prostate during external beam radiotherapy 1

Table of Contents 2

Glossary of terms 5

Table of Figures 6

Abstract 9

Declaration 11

Acknowledgments 11

Chapter 1 : Introduction 13

1.1 A brief history of EBRT for prostate cancer 13

1.2 IGRT, Inter- and Intra-fraction motion management 13

1.3 Intrafraction motion management techniques 14

1.4 Clarity Autoscan 4D-TPUS 15

1.5 Validating the Clarity Autoscan using a scanning water tank 15

1.6 Research goals 16

Chapter 2 : Literature Review 17

2.1 Prostate mobility 17

2.2 Prostate intrafraction motion and treatment margins 18

2.3 Examples of intrafraction motion management techniques 21

2.4 Benefits of TPUS for 4D-IGRT 26

2.5 Clarity Autoscan 4D-TPUS evaluations 28

2.6 Patient positioning and interfraction motion management for prostate EBRT 31
2.7 4D-TPUS Quality Control 35
Chapter 3 : Determining the feasibility of using a scanning tank for Clarity Autoscan verification 37
3.1 Introduction 37
3.2 Method 38
3.3 Results 43
3.4 Discussion 43
Chapter 4 : Position correction algorithm for refraction in 2-Dimensions 47
4.1 Introduction 47
4.2 Method 47
4.3 Results 60
4.4 Discussion 68
4.5 Summary 72
Chapter 5 : Position correction algorithm for refraction in 3-dimensions 73
5.1 Introduction 73
5.2 Method 73
5.3 Results 81
5.4 Discussion 82
5.5 Summary 90
Chapter 6 : Dosimetric effect of interrupting the beam and shifting the patient 91
6.1 Introduction 91
6.2 Method 91

6.3 Results 97

6.4 Discussion 101

6.5 Summary 102

Chapter 7 : Conclusion 103

7.1 Future work 104

Appendix: Supplementary Quality Control tests 107

Bibliography 122

Glossary of terms

4D-TPUS	Four-dimensional Transperineal Ultrasound
AFC	The Clarity Auto-Fusion and Contouring workstation is where US and CT images are fused and the US prostate contoured
AP (Ant-Post)	In the anterior-posterior direction relative to a patient in the HFS orientation
EBRT	External Beam Radiotherapy
EM	Electromagnetic – used in reference to EM beacons (aka RF transponders)
HFS	Indicates the head-first supine patient orientation for treatment or imaging
IGRT	Image-guided Radiotherapy – in this work this term specifically refers to the use of imaging for pre-treatment patient positioning
IMRT	Intensity-Modulated Radiation Therapy
Interfractional	Between treatment fractions
Intrafractional	Within or during a single treatment fraction
kV	Kilovoltage
LR (Left-Right)	In the left-right direction relative to a patient in the HFS orientation
Linac	Linear Accelerator
MU	Monitor Units – the unit of dose output of a linear accelerator
MV	Megavoltage
PMMA	Poly(methylmethacrylate)
QA	Quality Assurance
QC	Quality Control
RF	Radiofrequency – used in reference to RF transponders (see EM)
SI (Sup-Inf)	In the superior-inferior direction relative to a patient in the HFS orientation
US	Ultrasound
VMAT	Volumetric Modulated Arc Therapy

Table of Figures

Figure 1: Rear view of Clarity Autoscan probe affixed to base plate (left) and frontal view (right) showing probe-mounted reflectors (red) and ceiling-mounted IR cameras (yellow). 23

Figure 2: Side view of Autoscan probe attached to base plate. 24

Figure 3: Clarity QC phantom aligned to room lasers 25

Figure 4: Clarity screenshot with Live Guidance feature for probe position reproducibility highlighted 33

Figure 5: Experimental setup for Chapter 3 – treatment 40

Figure 6: Empty MP3-XS tank on treatment couch with rubber ball 40

Figure 7: tracking the Clarity QC phantom on graph paper 42

Figure 8: Reverse angle of setup showing tracking cameras suspended from ceiling 43

Figure 9: Geometric distortion due to time-of-flight and refraction in PMMA 46

Figure 10: Refraction through a medium ($v_t > v_i$) 48

Figure 11: Tank wall thickness at a range of different locations 49

Figure 12: Bi-layer 2D refraction model 52

Figure 13: Speed of sound in water as function of temperature 55

Figure 14: Solutions to reverse calculation with v_t = 2750 m/s (left) and v_t = 2270 m/s (right) 57

Figure 15: Experimental setup for verification of the 2D algorithm showing improved prostate analogue 59

Figure 16: Processing of anterior-posterior positional data showing ranges used for average position calculation 60

Figure 17: Example correction calculations for anterior-posterior series 62

Figure 18: Mean lateral difference from nominal before and after correction, plus corrected longitudinal differences (± 1 SD) 63

Figure 19: Mean longitudinal (SI) differences from nominal before and after correction, and vertical offset after correction (± 1 SD) 64

Figure 20: Mean vertical (AP) differences from nominal before and after correction, and longitudinal offset after correction (± 1 SD) 66

Figure 21: Effect of speed of sound in PMMA on total geometric error 67

Figure 22: Effect of tank wall thickness on total geometric error 68

Figure 23: Example of lateral 'profile' exhibiting periodic behaviour indicative of a dependence on sweep direction 69

Figure 24: Positional data update frequency variation with time 71

Figure 25: Rotation of the refraction plane about the X-axis. 74

Figure 26: Acquisition of lateral profiles (blue) with corrected values (orange) 78

Figure 27: MATLAB application for calculating and displaying raw (blue) and refraction-corrected (red) Clarity position data 79

Figure 28: Profile example showing data windows used for mean position calculation 80

Figure 29: Vector plot showing difference from nominal before and after refraction correction ... 81

Figure 30: Error magnitude as a function of distance of nominal position from the Clarity origin . 82

Figure 31: Corrected geometric error distribution of all points within the given radial distance from the Clarity origin (excluding points with tracking confidence < 0.5) 83

Figure 32: Ratio of corrected to raw geometric error magnitudes versus raw geometric error magnitude 84

Figure 33: Error magnitude as a function of distance from Clarity probe 85

Figure 34: Correlation between error magnitude and mean quality index..... 85

Figure 35: Relationship between θ and magnitude of corrected geometric error..... 87

Figure 36: Example of lateral profile showing position dependence on sweep direction 88

Figure 37: Experimental setup for dose measurements 92

Figure 38: Clarity display showing tracking volume surrounding chamber thimble in sagittal (left) and coronal (centre) planes..... 92

Figure 39: Response beam hold delay calculated from MU after beam hold triggered..... 99

Figure 40: General purpose ultrasound phantom target diagram 108

Figure 41: Transverse view of Clarity QC phantom showing internal structures (not to scale) .. 113

Figure 42: Clarity acquisition interface including imaging parameter controls..... 115

Figure 43: Medium_Coarse settings (left) and modified settings for sensitivity test (right) 119

Figure 44: Axial and lateral scaling assessment at the AFC workstation using the grid tool..... 120

Abstract

Introduction

The Clarity Autoscan 4D transperineal ultrasound (TPUS) system (Elekta, Sweden) for prostate motion management employs a vertically-oriented 2D ultrasound array that is continuously swept mechanically to repeatedly produce 3D images containing the prostate [1]. The target position relative to a pre-fraction reference scan is determined multiple times per second. Other investigators have studied the tracking accuracy of the system using displacements of ≤10 mm from the initial normalisation point typical to a clinical treatment [1-4].

The primary aim of this work was to utilise clinically available equipment to compare the target positions reported by the Clarity Autoscan system to known target positions over the full imaging volume. A scanning dosimetry water tank was used, however refraction in the 20 mm PMMA wall of the tank presented a significant complication. The potential variation in target dose due to intervention based on the Clarity prostate motion management was also investigated.

Method

A prostate analogue was mounted to the scanning mechanism of a MP3-XS scanning water tank (PTW, Germany). The Clarity probe was positioned externally against the wall of the scanning tank in the treatment orientation. The scanning mechanism was programmed to make in-plane, cross-plane and diagonal 'profiles' in the horizontal plane ranging approximately ±30 mm from the isocentre. Seven sets of these four 'profiles' were acquired between ±30 mm in the vertical direction yielding data throughout a 60 cm-sided cube centred on the isocentre. A bi-layer 3D refraction correction algorithm was derived to account for refraction caused by differences between the speed of sound in both PMMA and water from the speed of sound in soft tissue assumed by the Clarity system.

The prostate analogue was then replaced with a Farmer-type ionisation chamber and monitored by the Clarity system during beam delivery. Programmed movements of the chamber triggered manual or automatic suspension of the beam and the resulting measured doses compared.

Results

Without refraction correction the maximum difference in the reported positions from the programmed positions was 9.3 mm and the mean(±SD) difference was 4.0±1.8 mm. Refraction correction reduced this to a maximum of 3.4 mm, and a mean(±SD) of 1.0±0.5 mm. The worst results were at the peripheries of the imaged volume and near the transducer where the Clarity system had difficulty maintaining tracking due to narrowing of the swept imaging volume. At the lateral (left-right) and vertical (anterior-posterior) extremities, the prostate analogue images were visibly distorted which may have affected the accuracy of the Clarity centroid position calculation.

There was no significant difference in measured dose between manual and automatic beam suspension in a 10x10 cm^2 field when the target moved along the beam axis. Furthermore, there was only a minimal difference in measured dose to the centre of the 'prostate' between intervention and no intervention when the 'prostate' was programmed to move ±20 mm along the beam axis during a 180 MU 10x10 cm^2 field beam. However, it was found that there was a delay of 5.4±0.9 s between threshold crossing and beam suspension which could become significant at higher dose rates.

Conclusions

The target positions reported by the Elekta Clarity Autoscan system can be validated using a programmable scanning water tank by employing a refraction correction if care is taken in the initial positioning of the transducer. Further improvement might be achieved by using a smaller target analogue and associated volume to reduce the effect of the refraction-induced distortion on the Clarity centroid calculation.

Intervention following detected prostate motion along the beam axis will have minimal effect on the dose to the centre of the prostate; however, motion in any direction will compromise target coverage and dose minimisation to healthy tissue.

Declaration

I certify that this work contains no material which has been accepted for the award of any other degree or diploma in my name, in any university or other tertiary institution and, to the best of my knowledge and belief, contains no material previously published or written by another person, except where due reference has been made in the text. In addition, I certify that no part of this work will, in the future, be used in a submission in my name, for any other degree or diploma in any university or other tertiary institution without the prior approval of the University of Adelaide and where applicable, any partner institution responsible for the joint-award of this degree.

I give permission for the digital version of my thesis to be made available on the web, via the University's digital research repository, the Library Search and also through web search engines, unless permission has been granted by the University to restrict access for a period of time.

I acknowledge the support I have received for my research through the provision of an Australian Government Research Training Program Scholarship.

Signed: Date: 27/02/2019

Acknowledgments

Many thanks to Dr Scott Penfold, Dr Louis Fourie and Dr John Baines for their invaluable guidance, and for their tireless efforts reviewing this work.

Above all, undying love and gratitude to my wife, Rebecca, for your endless patience and for being a single parent over the years spent on this endeavour.

To Jacob, Elijah and Tristan, for your inspiration and motivation, and making me so proud.

Chapter 1: Introduction

1.1 A brief history of EBRT for prostate cancer

X-radiation has been employed in the treatment of prostate cancer since the early 20th century. In 1913 Pasteau and Degrais proposed that radium could be inserted into the urethra or rectum, marking the first attempt at employing "brachytherapy" for prostate cancer [5]. Shortly thereafter the practice of direct insertion of radioactive "seeds" into the prostate was developed – a practice that is still used today. Megavoltage (MV) photon external beam radiation therapy (EBRT) emerged as a by-product of the US nuclear weapons program in the 1950s when cobalt-60 produced in nuclear power reactors began to be used for this purpose. Around the same time researchers at Stanford Medical Centre realised that their linear accelerator could be used for the treatment of localised carcinoma of the prostate but with the added advantage of greater skin-sparing due to the potential for higher photon energies than cobalt-60.

With evermore powerful computers and imaging technologies has also come the ability to image, identify, plan and treat the target volume with ever-increasing precision and accuracy. External beam treatment of prostate cancer has evolved from single beam treatments, through "4-field brick" and 3D conformal, to intensity modulated step-and-shoot (IMRT), modulated arc (VMAT) and stereotactic (SBRT or SABR) techniques. The standard of care for external beam radiotherapy of the prostate in Australia in 2019 is trending from IMRT toward VMAT.

1.2 IGRT, Inter- and Intra-fraction motion management

With the advent of conformal and intensity modulated techniques, one of the larger potential uncertainties is in the ability to precisely and repeatably position the patient such that the treatment fields will coincide on the target volume. This is made more difficult in the case of the prostate as experience with modern imaging techniques has shown that the prostate can move both between (interfraction) and during (intrafraction) treatments by more than a centimetre in relation to the bulk habitus [6], and thereby also any external markers such as tattoos that may be used for positioning the patient for treatment. It has therefore become an imperative of the development of modern radiotherapy techniques to improve the precision and accuracy of patient positioning.

Image-guided radiotherapy (IGRT) has developed considerably over the past two decades, with kilovoltage (kV) cone-beam imaging systems capable of 2D planar or 3D cone-beam computed

tomography (CBCT) reconstruction now the standard on new medical accelerators. This affords a range of options for setting up the patient for treatment based on the anatomy as presented for treatment each day, as well as managing patient or organ motion during treatment. The American National Cancer Institute (NCI) website defines IGRT as *"A procedure that uses a computer to create a picture of a tumor (sic) to help guide the radiation beam during radiation therapy [7]."* However, throughout this work the much narrower definition of image guidance for interfraction motion management only will be used, as this appears to be what has been adopted by the Elekta Clarity Autoscan system.

The Clarity Autoscan 4D transperineal ultrasound (TPUS) system (Elekta, Sweden) has been designed not only to allow prostate motion to be monitored and accounted for during a treatment beam (intrafraction), but also between treatment fractions (interfraction). Therefore, when not using the system for interfraction management (i.e. intrafraction only), the software requires the "*non-IGRT mode*" option to be ticked. This instructs the system that an alternative method of patient positioning will be used such as kV-imaging and changes the Clarity workflow in ways that will be discussed later.

Intrafraction motion monitoring enables intervention when the volume that is being tracked moves outside of predefined thresholds. Theoretically, this means that either smaller error margins can be used around the target volume to reduce dose to healthy tissue, or the dose delivered to the target can be increased or 'escalated'.

1.3 Intrafraction motion management techniques

Three main approaches to motion management have emerged in recent years: implanted electromagnetic (EM) beacons, intrafraction kV imaging, and 4D TPUS. The EM beacon approach utilises an antenna positioned over the patient and encapsulated radiofrequency (RF) transponders or 'beacons' that are small enough to be inserted directly into the prostate [8]. This is similar to gold seeds traditionally implanted to improve localisation under interfraction kV imaging. The intrafraction kV imaging approach makes use of the on-board kV imaging systems that are standard on most modern linear accelerators to image the target throughout the treatment, while software analyses the images to locate the gold seeds [9]. The 4D TPUS technique employs mechanically-swept 2D ultrasound array to repeatedly reconstruct images of the volume encompassing the target in near-real time [1].

Necessarily, there are various advantages and disadvantages to each approach: for instance, the antennae that receive the signals from the EM beacons have a limited range which impacts on patient suitability due to their physical size. Treatment fields may traverse through the antennae, so must be accounted for in treatment planning. Depending on the treatment modality, whether it be step-and-shoot or continuous arc, the kV intrafraction approach is only able to detect near-real time motion in two dimensions. The 4D-TPUS method may suffer from greater latency than the other two approaches.

1.4 Clarity Autoscan 4D-TPUS

The Elekta Clarity 3D transabdominal ultrasound (TAUS) system for target localisation has been around for the better part of 2 decades. It utilises a handheld ultrasound probe with which the user makes a freehand sweep over the volume of interest to acquire volumetric data. The location and orientation of the probe within the simulation or treatment room is tracked via an array of infrared reflectors on the probe and a pair of stereoscopic infrared cameras fixed to the ceiling. This enables the position and orientation of the probe, and hence the target, relative to the treatment isocentre to be determined, and improves the volumetric reconstruction.

The Clarity Autoscan 4D TPUS is an extension of the Clarity 3D system, wherein the transducer is no longer swept freehand, but mechanically. This enables continuous acquisition throughout the treatment delivery without exposing an operator to significant radiation risk. The system also includes a dedicated Auto-contouring and Fusion (or AFC) workstation, which hosts the Clarity server for patient image and tracking data storage. Lachaine and Falco [1] provide an excellent introduction to the system, including the results of their validation work using a phantom on a motion platform. They also describe the series of phantom, probe and room calibration processes necessary for the system to be used. However, it has been determined from clinical experience that it would be beneficial to establish a more rigorous set of quality control tests to supplement the manufacturer's recommendations (see Appendix).

1.5 Validating the Clarity Autoscan using a scanning water tank

As will be discussed in the next chapter, various methods of validating the positional accuracy of the Clarity Autoscan system have been demonstrated in the literature; however, it was desirable to find a validation method that *a)* used equipment readily available in the clinic, *b)* can cover as much as possible of the full range of expected intrafraction prostate motion, and *c)* can precisely

set the position of the object being tracked. For these reasons it was decided that a scanning water tank used for reference dosimetry might be useful since most clinical departments will have at least one. Furthermore, the MP3-XS system used for this study can be programmed to move to a sequence of positions with a precision of 0.1 mm in each axis.

The main impediment to using the scanning water tank for validating the Clarity-reported target positions is the different acoustic impedances of the materials involved – more specifically, the differences between the speed in soft tissue assumed by the ultrasound system of 1540 m/s, and the speeds of sound in the tank wall material (poly (methyl methacrylate) or PMMA) and the water filling the tank. These differences not only result in refraction occurring at the interfaces but also displacement aberrations due to the differences in the "time-of-flight". This is because the ultrasound operates in pulse-echo mode, whereby the time between pulse emission and echo detection – each performed by the same transducer elements – determines the distance of the source of the echo from the transducer elements. If the actual speed of sound in a material differs significantly from that assumed by the system, then the system will misinterpret the physical distance between the source of the echo and the transducer.

1.6 Research goals

The purpose of this work is to develop a method of validating the tracking accuracy of the Clarity Autoscan 4D-TPUS system throughout a clinically useful volume using equipment typical to a radiotherapy medical physics department. This will be achieved by using programmed movements of a prostate analogue in a scanning water tank designed for dosimetry of a medical linear accelerator. This will require a 3D refraction correction algorithm to be developed to account for refraction in the wall of the scanning tank. Once this has been achieved the impact of the inherent latency in the Clarity Autoscan scanning mechanism will be investigated including on dose to the target due to target motion and Clarity-triggered beam interruption.

Chapter 2: Literature Review

2.1 Prostate mobility

Improvements in imaging technology available for treatment planning by the late 1980's began to reveal that the prostate was not a stationary organ, as had previously been assumed. Ten Haken *et al*. [10] calculated potential dosimetric effects of interfraction prostate motion as early as 1991, observing that the variability in rectal and bladder filling between fractions was the main source of this motion. In 1995 Crook *et al*. [11] reported an assessment of intraprostatic gold seed position relative to bony landmarks using films from both initial and boost planning sessions. After ruling out independent seed migration it appeared that the average prostate motion between these two time points was greater than 5 mm in both the posterior and inferior directions, and that this posteroinferior motion correlated to lesser rectal and bladder filling. In nearly a third of patients the base of the prostate was displaced more than 10 mm posteriorly.

By 2005 there had been numerous studies regarding prostate motion and how it related to treatment planning. Thomas Byrne [6] produced an extensive review of 49 articles published between 1982 and 2005. He confirmed the early findings regarding the correlation between bladder and rectal filling and prostate motion and further noted the minimal effect of respiratory motion on prostate position. The magnitude of prostate motion reported by the works reviewed varied considerably. However, there were significant differences between the studies in both the number of patients examined and the methodology employed, with many of the studies pre-dating the broad usage of gold seeds or of ultrasound for prostate localisation. Of the 11 imaging studies reviewed that included statistical analysis, the maximum total prostate motion range reported was 35 mm [12]. However, this was a significant outlier compared to the other reports which ranged from approximately 2 to 20 mm.

In 2015 Ballhausen *et al*. [13] demonstrated that intra-fraction prostate motion can be treated as a random walk by showing that the variance in prostate position increased linearly over time. The tendency was for the prostate to drift away from the isocentre during a treatment fraction and hence shorter fractions would reduce the effect of the prostate motion. Based on their findings they concluded that fixed margins will tend to over-compensate at the beginning of the fraction and under-compensate at the end of the fraction. Considering this, along with the significant inter- and

intra-patient prostate motion variability that they found, they concluded that online tracking and position correction would be the preferred approach for prostate intrafraction motion management.

2.2 Prostate intrafraction motion and treatment margins

2.2.1 Margin calculation

Systematic and random errors at all stages of radiotherapy, from treatment planning to delivery, are accounted for by the addition of a margin around the clinical target volume (CTV) [14] yielding the planning target volume (PTV). An appropriate margin may be determined using, for example, the Van Herk formalism [15], which is a weighted sum of the total systematic (Σ) and random (σ) errors in which the systematic errors are weighted significantly more heavily than the random errors. Van Herk [16] points to uncertainty in target delineation as an example of a systematic error since the delineation error will propagate to all subsequent treatments. Organ motion is described as introducing both a systematic and a random component, as the random positional error at the time of simulation will also propagate throughout all treatments as a systematic error, while the daily organ position will be random.

2.2.2 Target coverage and normal tissue toxicity

If sources of error can be reduced or eliminated then the treatment margin required to account for all systematic and random errors may be reduced, yielding positive clinical benefits. Balter *et al*. [17] reported in 1993 that using MV portal imaging to reposition the patient to correct for setup errors greater than 10 mm resulted in a 6 mm margin reduction, sparing 10% of the volume of rectum and bladder from high radiation dose. Sripadam *et al*. [18] used the rectal wall as a surrogate for prostate position in pre-fraction CBCT imaging and reported that rectal motion during prostate EBRT may reduce the dose coverage of the CTV while increasing the volume of rectum in the high dose region by up to 25 percent. They referenced the work of Zelefsky *et al*. [19] who showed that dose escalation to the prostate was possible while reducing acute and late rectal toxicities using the intensity-modulated radiotherapy (IMRT) technique, due to the improved dose conformance to the PTV relative to conformal radiotherapy. In a similar way, careful reduction of the treatment margin will improve the dose conformance to the CTV so one would expect similar benefits.

It has been shown [20, 21] that IGRT using CBCT and fiducial markers can facilitate significant margin reduction resulting in improved target coverage and less dose to OARs. Others [22, 23] have quantified the benefits of margin reduction that IGRT facilitates by comparing the OAR toxicity and tumour control outcomes between patients treated with and without IGRT. Alternatively, Raziee *et al*. [24] showed that instead of reducing the treatment margins, IGRT enabled target dose escalation, improving the 5-year biochemical recurrence rates with no change in the degree of metastasis or toxicity.

2.2.3 Reducing margins by management of motion

Beltran *et al*. [25] noted a decade ago that "Intrafraction prostate motion is a limiting factor for margin reduction." Intrafraction monitoring of 3-dimensional organ motion coupled with some form of intervention, such as beam gating or target-following dynamic MLC (DMLC), can therefore be expected to permit a reduction in the applied margin. The appropriate use of reduced uncertainty margins can lead to reduced toxicity in organs at risk (OAR) such as the rectum.

However, not everyone is convinced that intrafractional prostate motion management can lead to significant reductions in treatment margins. Li *et al*. [26] investigated the potential gains from real-time target monitoring and intervention, considering beam gating, DMLC tracking and real-time couch corrections without beam interruption. They found that significant margin reductions for the general population could only be achieved if rotations were also accounted for, and were critical of the findings of Litzenberg *et al*. [27], who claimed a potential margin reduction to 1.5 mm when using implanted markers for patient setup and a 3 mm threshold for motion intervention. Li *et al*. had studied a considerably larger patient cohort and pointed out that Litzenberg *et al*. had considered no other source of geometrical uncertainty than intrafractional motion in their margin calculations.

Li *et al*. did concede that for the 7 out of 105 patients that they studied who had the largest intrafraction motion, management of that motion could justify a considerable reduction in margin of 9.5 mm to 7.6 mm posteriorly for a 3 mm intervention threshold, or down to 4.6 mm for an adaptive 4D treatment (i.e. compensating for translations *and* rotations in real-time via couch tilt or MLC adaption). Considering the findings of Ballhausen *et al*. above, that the prostate tends to randomly walk away from the starting position over time, it is important to note that the typical duration of the

treatment fractions studied by Li *et al*. was 10 to 20 minutes while Litzenburg *et al*. monitored each patient for only 8 minutes.

Lachaine and Falco stated in their 2013 paper introducing the Elekta Clarity 4D-TPUS system [1] that management of intrafraction motion was of particular importance to hypofractionated regimes and stereotactic ablative radiotherapy (SABR), in which the entire treatment dose is delivered in only a few fractions. They prefaced this by noting that hyperfractionated regimes will tend to blur the effect of intrafraction organ motion; furthermore, one would assume that the high dose per fraction of hypofractionation or SABR will also lead to longer treatment times and hence greater organ motion than during, at least, a standard VMAT technique.

In 2018 Pang *et al*. [28] published data on duration-dependent margins based on their analysis of intrafraction prostate motion using a 4D-TPUS. Naturally they concluded that a VMAT technique was preferable over IMRT due to the reduced treatment times from approximately 10 minutes to 3-4 minutes, permitting reduced treatment margins. They provide margins calculated for both treatment types, but in both cases, they are considerably smaller than those calculated by Li *et al*. They also provide supplementary material in which an example is given of the geometric uncertainties used to derive the recommended margins, however only intrafraction motion is listed, so it is unclear if they have used the same approach as that which Li *et al*. were critical of in the work of Litzenberg *et al*.

A review of target margins in use in radiotherapy of prostate cancer by Yartsev & Bauman [29] in 2016 found that a wide variety of margins were in clinical use, correlating with the techniques being employed for patient positioning. They state that the literature would support the use of a 5 mm margin posteriorly and 8 mm in all other directions, in conjunction with fan-beam CT or CBCT for pre-treatment guidance. Unfortunately, the search criteria employed did not yield very many publications that included intrafraction motion management (6 out of 155 using EM beacons) and none using 4D-TPUS. It was noteworthy, however, that the two works by Li *et al*. and Litzenberg *et al*. discussed above were indicative of the extremes of the margins being utilised clinically in conjunction with EM beacons.

2.3 Examples of intrafraction motion management techniques

Numerous approaches to intrafraction motion management have been discussed in the literature, falling generally into three categories: those requiring only “standard” equipment (e.g. kilovoltage intrafraction monitoring or KIM); those requiring additional hardware to standard equipment (e.g. Clarity 4D-TPUS); and treatment systems that are specifically designed for 3D or 4D IGRT (e.g. MRI-Linac).

2.3.1 IGRT using standard equipment

Keall *et al*. [9] published a review article in 2018 posing the question of whether a tipping point has been reached concerning the ubiquitous utilisation of real-time radiotherapy delivery. They considered only clinically implemented approaches to real-time IGRT on linacs equipped with the three main patient monitoring systems that were considered standard at the time of publication: EPID-based MV imaging, kV imaging and respiratory monitoring. Each of the three clinical approaches that they discussed involved varying degrees of intrafraction kV imaging: *1)* kV intrafraction monitoring (KIM); *2)* combined MV and kV imaging (MV/kV); and *3)* combined optical and sparse monoscopic imaging with kV (COSMIK).

The KIM method employs a probabilistic approach to overcoming the limitations of the 2D kV image acquisition by calculating the most probable 3D trajectory of implanted fiducials based on the latest 2D image. This approach requires continuous acquisition of kV images throughout the treatment fraction leading to a non-trivial increase in radiation dose to the patient. The MV/kV approach takes advantage of the orthogonal arrangement of the kV and MV imaging systems by combining continuous MV imaging with kV images acquired every 20° of arc angle.

The COSMIK method utilises the Varian RPM optical tracking system, correlating the 3D motion of an infrared reflector placed on the patient to organ motion caused by respiration during a pre-treatment CBCT. During treatment the optical system continues to monitor the patient’s respiration at 20 Hz while planar kV images are acquired only once every 3 seconds (The framerate for the Elekta XVI CBCT system is 5.5 Hz while the Varian system is 11 Hz). The images are used to correct for baseline drift in the correlation model – which maps the reflector motion during CBCT to internal motion in the CBCT – in near-real-time.

The authors point out that not only do all three methods involve additional dose due to kV imaging, they also rely on implanted fiducial markers and discuss the inherent costs and risks associated with them. They too note that particularly for prostate cancer patients it is currently standard practice to implant fiducial markers to improve pre-treatment setup accuracy for external beam radiotherapy.

2.3.2 Calypso 4D IGRT system

In 2006 Willoughby *et al*. [8] described the first human use of the Calypso 4D localisation system which utilises electromagnetic transponders (or EM beacons) implanted within the prostate and a noncontact AC magnetic array for positional detection, demonstrating comparable localisation accuracy to x-ray techniques. The utility of this system, which has the advantage over x-ray techniques of no additional radiation dose to the patient, has since been demonstrated by a number of authors as summarised by Shah *et al*. [30]. It does, however, have several limitations. For instance a minimum of two transponders must be invasively implanted within the prostate [30] and are known to produce artefacts in MR imaging used for disease management and follow-up [4]. While this is accepted practice due to the wide adoption of gold seed fiducial markers in prostate cancer for pre-treatment positioning, other techniques such as ultrasound may permit the elimination of this invasive procedure. Furthermore, the maximum distance from the geometric centre of the transponders to the magnetic array is approximately 17 cm which will exclude larger patients. Lastly, the Calypso system is not compatible with Elekta linear accelerators, or more specifically the Elekta treatment couch.

2.3.3 MRI for 4D IGRT

Lagendijk *et al*. [31] discussed the possible integration of a high-field MRI scanner with a linac in 2008; almost a decade later the first patient was treated with the Elekta Unity MRI-Linac [32]. In 2013 Bjerre *et al*. [33] described how orthogonal pairs of 2D images acquired via cine-MRI could be used to track the 3D trajectory of a soft-tissue target structure, and were able to accurately track the 3D motion of the left kidney as a proof of this concept. Now that these integrated MRI-Linac systems are clinically available there should be no impediment to this technique being extended to other applications in the future such as prostate intrafraction motion.

2.3.4 Clarity Autoscan 4D-TPUS for intrafraction motion management

In 2012 at the American Society for Radiation Oncology 54th Annual Meeting an oral presentation by Abramowitz *et al*. [2] and a poster by Wallace *et al*. [34] outlined the prototyping and feasibility of the Clarity Autoscan 4D-TPUS system for intrafraction prostate motion management. It was the 2013 paper by Lachaine and Falco [1], however, that provided an in-depth introduction to the system. They described a 2D ultrasound transducer array that is mechanically swept to image a volume that includes the prostate and some of the urinary bladder, utilising the perineum as an ultrasonic window. The housing containing the transducer has an array of reflectors fixed to it (highlighted in both views of Figure 1) allowing the position of the array to be tracked by a pair of stereoscopic infrared cameras attached to the ceiling in both CT-simulation room and treatment rooms.

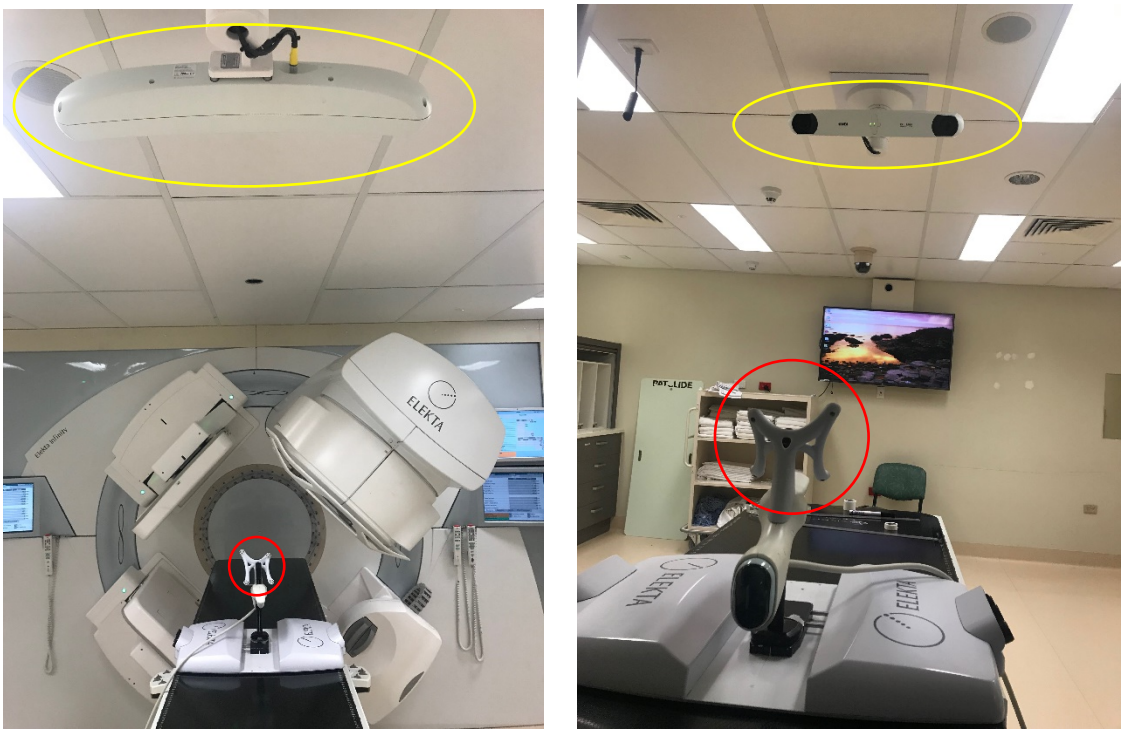

Figure 1: Rear view of Clarity Autoscan probe affixed to base plate (left) and frontal view (right) showing probe-mounted reflectors (red) and ceiling-mounted IR cameras (yellow).

The system comes with a base plate (Figure 2) and cushions over which the patient's legs are positioned. The Clarity probe has a vertical post attached to it which connects the base plate. The position of the post is adjustable laterally and longitudinally via the adjustment knobs visible in

Figure 2 to facilitate optimal positioning of the probe against the perineum. The Autoscan probe is affixed to the post with a further three degrees of freedom: vertical movement up and down the post via the trigger and limited rotations vertically and laterally via a button on the underside of the grip. Once the patient is in position with their legs over the base plate the probe is attached to the base plate and adjusted for optimal image acquisition. Once the probe is in position it does not move again: the scanning of the ultrasound imaging plane is achieved by an internal mechanism, with the transducer sweeping internally relative to the probe housing. If the patient were to inadvertently move the probe the during acquisition this will be compensated for via the IR-tracking.

Figure 2: Side view of Autoscan probe attached to base plate.

Lachaine and Falco gave a detailed description of the processes involved in calibrating the system, centring around a dedicated phantom that is also used for daily quality control testing. Calibration is a three-step process: The first step is the phantom characterization in which the Clarity QC phantom is scanned using x-ray computed tomography to establish the locations of the internal structures of the phantom relative to fiducial markers embedded in the phantom housing that will represent the Clarity coordinate system. Secondly, in the room calibration the position and orientation of the ceiling mounted cameras relative to the linac coordinate system is determined by aligning the Clarity QC phantom to the room lasers and capturing the spatial positions of the

reflectors on the QC phantom. The third and final step is the probe calibration in which a 3D image of the internal structures of the Clarity QC phantom is acquired with the probe. The probe calibration establishes the relationship between the reflector array on the probe and the ultrasound image coordinate system. Hence, the position of a given voxel in the room coordinate system can be determined from the position in the ultrasound frame via:

$$r_R = {}^{R}T_T \, {}^{T}T_P \, {}^{P}T_F r_F \quad (1)$$

where ${}^{P}T_F$ is the image-Frame-to-Probe-reflectors coordinate transformation, ${}^{T}T_P$ is the Probe-to-camera (aka Tracker) coordinate transformation, and ${}^{R}T_T$ is the Tracker-to-Room coordinate transformation.

The phantom characterization is repeated monthly to account for the gradual motion of the internal phantom structures due to drying-out of the phantom material. Daily QC is performed with the phantom aligned to the room lasers and a 3D image of the phantom acquired. This process checks both the room setup and probe calibration and applies a 1 mm tolerance to each in all cardinal directions.

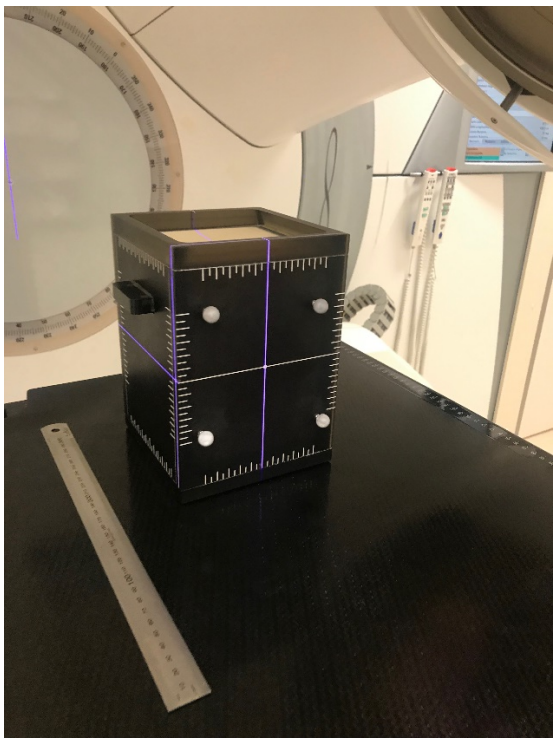

Figure 3: Clarity QC phantom aligned to room lasers

For intrafraction monitoring of prostate motion, a 3D ultrasound image is acquired daily via a single sweep of the transducer prior to the commencement of treatment. This is then registered to a similar 'reference' image acquired at the time of treatment simulation and the required patient shifts are determined. At this point the operator can either reposition the patient using these Clarity shifts or utilise an alternative IGRT technique (e.g. CBCT and fiducial markers) and zero out the Clarity shifts once the patient has been repositioned. Tracking is then commenced, and the treatment initiated. Each sweep of the transducer takes approximately 2.5 seconds, however the 3D images are reconstructed and registered more frequently (approximately 1.43 Hz) as new radial 'slices' are acquired. If the target volume crosses user-defined thresholds either a warning will be displayed on the Clarity console or, if the facility has the Elekta Response beam gating system, a beam hold is generated.

Unlike diagnostic ultrasound systems Clarity Autoscan only operates in B-mode; however, the sweeping mechanism enables it to acquire images in 2D, 3D or 4D format. Live 2D imaging is used for initial positioning of the probe relative to internal anatomical structures and, if at treatment, relative to the probe position used at simulation. 3D mode is used at treatment simulation to acquire a reference image, and 4D mode is for intrafraction monitoring. Employing a 5 MHz transducer, the frequency can be adjusted to change the focus depth.

There are no known contra-indications for US-guided RT, and unlike systems such as EM beacons where there are physical limitations, no reported limitations were found for the Clarity Autoscan system. However, the latter part of this work will investigate a potential drawback of this approach regarding boundary-crossing detection latency due to the transducer sweep period.

2.4 Benefits of TPUS for 4D-IGRT

2.4.1 Ultrasound

As discussed above, the benefits of ultrasound for intrafraction motion management include improved soft tissue contrast and no additional radiation dose. Additionally, the daily pre-treatment 3D ultrasound, which is a necessary part of the workflow, enables the radiation therapists to assess the level of bladder filling compared to that at the time of planning simulation [35]. Furthermore, one of the most unique elements of the introduction of the high-field MRI-Linac is the future availability of online quantitative imaging techniques. When 3D ultrasound is already part of the workflow there is the potential for extension of this technique to, for instance, elastography to

assess tumour response online [36, 37]. While the Clarity Autoscan system does require the purchase and installation of some additional hardware, the cost is limited compared to the purchase of a dedicated IGRT system such as an MRI-Linac or Cyberknife.

2.4.2 Transperineal

Three dimensional transabdominal ultrasound was established over a decade ago for interfraction motion management [38, 39]. At that time, it was unsuitable for intrafraction motion management as it would require an operator to remain in the room during treatment. Bell *et al*. [40] have proposed a robotic system for transabdominal ultrasound guidance; however, the advantage of the transperineal approach is that the whole system is well clear of the gantry and cannot obstruct the beams. Furthermore, image quality in transabdominal ultrasound of the prostate relies on sufficient bladder filling and can suffer from shadowing due to the pubic symphysis [1]. The physical distance to the prostate can also be significantly less via the perineum depending on the size of the patient, permitting improved resolution.

Salter *et al*. [41] investigated the potential alignment error from using transabdominal ultrasound for patient positioning due to tissue variations and found that for every 10 mm of fat between the probe and the transducer the target would appear approximately 0.7 mm further from the transducer than it truly was. Fontanarosa *et al*. [42-44] confirmed this by demonstrating that transabdominal ultrasound could benefit from a simulation CT-based density correction to account for speed-of-sound variations in different tissues, which yielded shifts of up to 3.6 mm toward the transducer. As this is almost entirely due to imaging through adipose tissue, transperineal imaging should significantly reduce this effect, although no studies were found to have investigated this.

Transrectal ultrasound is used for guiding the placement of fiducial markers in prostate EBRT patients and could conceivably be used for image guidance; however, it is somewhat invasive and may not be well tolerated over a full course of treatment. Furthermore, as with transabdominal ultrasound the rectal probe could be in the path of some of the treatment beams [45].

2.5 Clarity Autoscan 4D-TPUS evaluations

2.5.1 In silico *investigations*

Lachaine & Falco [1] modified a commercially available ultrasound quality control phantom, adding an extra acoustic window and optical markers for positional tracking of the phantom. A programmable motion stage was used to move the whole phantom ±10 mm in the anterior-posterior direction and ±5 mm in the left-right direction while being continuously tracked using the Clarity system. A gel pad was then placed between the probe and the acoustic window to enable measurements in the superior-inferior direction over a range of ±4 mm. The mean ± SD differences from the programmed positions that they reported are listed in Table 1 below.

Abramovitz *et al*. [2] used a tank filled with water and Zerdine hydrogel, and a submerged programmable motorised target. Attached to the target were EM beacons and optical markers on a stem which extended out of the water and enabled motion tracking for comparison with the Clarity-reported target positions. The target was programmed to move using patient motion profiles taken from the literature. Data from the three tracking modes were compared with the programmed motion in each axis. They reported that 95% of the maximum distance variation was within 1.3 mm of programmed motion and concluded that the Clarity system could accurately and reproducibly track the motion of their prostate analogue.

More recently Yu *et al*. [3] used a male pelvic phantom designed for multi-modality imaging and a motion platform. They made movements in the phantom of ±3 mm in the superior-inferior and left-right directions while the phantom position was optically tracked. The results are listed in Table 1. They also found a delay in the optical positional tracking of the Clarity system of approximately 0.2 seconds.

Finally, Han *et al*. [4], continuing the work of Yu *et al*., reported the results of further *in silico* measurements performed to validate a proposed *in vivo* evaluation (discussed below), noting that no previous assessments of the Clarity Autoscan tracking accuracy had been performed in patients. This time the pelvic phantom on the motion platform was implanted with radiopaque fiducial markers. Orthogonal kV images were used to determine the initial positions of the fiducial markers in the phantom and portal images continuously acquired throughout a simulated treatment. Meanwhile, 4D-TPUS was used to monitor intrafraction translations in the phantom induced by the

motion platform. The 4D-TPUS tracking results were used to project updated fiducial positions throughout treatment into the plane of the electronic portal imaging device (EPID) and compared to the 2D EPID-measured positions. They concluded that the precision of their method of comparing 4D-TPUS reported positions against that of EPID-reported fiducial markers was 1.1 mm or better.

Table 1: Results of previous in silico *4D-TPUS evaluations*

Study	*Method*	*Range of Motion Tested*	*Results*
Lachaine & Falco 2013 [1]	U/S QC phantom on motion platform; optical tracking.	AP: ±10 mm LR: ±5 mm SI: ±4 mm	AP: -0.2 ± 0.2 mm LR: 0.2 ± 0.4 mm SI: 0.0 ± 0.2 mm
Abramowitz *et al*. 2012 [2]	Water phantom; RF beacons & optical markers on a stem.	Clinical prostate motion datasets from literature	Mostly within 1 mm (max 1.3 mm)
Yu *et al*. 2017 [3]	Pelvic phantom on motion platform; optical tracking.	LR/SI: ±3 mm	LR: 0.25 (0.23 RMS) mm SI: 0.18 (0.45 RMS) mm
Han *et al*. 2018 [4]	Pelvic phantom on motion platform including implanted fiducials; optical tracking.	SI (?): ±4 mm (programmed motion direction(s) unclear from paper)	SI (?): ≤ 1.1 mm Mean difference in EPID pixel coordinates [u,v] (mm): [0.0 ± 0.4, 0.0 ± 0.3]

2.5.2 In vivo *investigations*

The 2012 study by Wallace *et al*. [34] mentioned above discussed the final stages of prototyping and assessment of the Clarity Autoscan system, whereby 4D-TPUS was used in 10 patients to optimise hardware and software components of the system, followed by 5 patients using the optimised configuration. All 15 patients also received TAUS post-treatment. TPUS and TAUS image clarity was assessed and scored between 0 and 3. On average, in the final 5 patients TPUS (2.8) was found to more clearly define the apex of the prostate than in TAUS (1.4), which appeared to be due to shadowing in some patients by the pubic symphysis during TAUS. Clarity of rectum and bladder neck were comparable between modalities, however while the penile bulb was virtually

unresolvable on TAUS (average score 0.1 out of 3) it was clearly defined using TPUS (2.6 out of 3). Staff and patient acceptance was also documented and found to be excellent for all patients.

A 2013 study by Abramowitz *et al*. [46] described the results of a clinical trial comparison to RF transponders in which 7 patients were monitored during treatment using both RF transponders and 4DTPUS simultaneously. They found high concordance between the non-invasive 4DTPUS system and RF transponders (see Table 2).

Richardson & Jacobs [47] reported the first clinical assessment of 4D-TPUS in the United Kingdom in 2017. They analysed data from 526 treatment fractions for 20 patients to assess the extent of intrafraction prostate motion with consideration of three different intervention thresholds of 3 mm, 7 mm and 10 mm. They found that every patient had at least one 3 mm prostate excursion. In only 2% of fractions did the prostate move by 10 mm or more, occurring at least once in 35% of patients. Posterior excursions were found to be by far the most common. In one patient the prostate was seen to be outside of the 3 mm posterior threshold for 92% of his treatment time.

As mentioned in section 2.5.1, Han *et al*. [4] performed *in vivo* and *in silico* evaluations of the Clarity Autoscan 4D-TPUS prostate motion monitoring system. The *in vivo* procedure followed the *in silico* process described above. They reported results of the assessment of 195 fractions or almost 40 hours of simultaneous intrafraction monitoring by both 4D-TPUS and portal imaging. They reported a variation in agreement between predicted (2D TPUS projection) and 'actual' (portal-imaged) fiducial marker positions of between 1.3 and 3.3 mm. They concluded that 4D-TPUS prostate motion management yielded an average reduction in the maximum prostate localisation error of 20%.

In 2018 Grimwood *et al*. [48] followed a similar approach to Han *et al*., comparing intrafraction prostate motion monitored by 4D-TPUS to 2D portal images acquired at 5 time points during treatment. Intraprostatic fiducial marker positions were determined in pre-fraction CBCT and intrafraction translations from 4D-TPUS used to update the marker positions and project them into the plane of the EPID. The projected positions were then compared to the imaged positions, returning a median difference of 0.6 mm, with 95% limit of agreement at 2.5 mm. Furthermore, they found that confidence in the Clarity-reported motion was robust to changes in image quality, but did degrade under poor probe placement.

The accuracy of the Clarity Autoscan has been shown to be comparable to RF transponders and EPID for intrafraction motion monitoring. Further evaluations have been conducted focusing on the use of 4D-TPUS for pre-fraction patient positioning, which will be discussed in the next section.

Table 2: Results of previous in vivo *4D-TPUS evaluations*

Study	*Method of Assessment*	*Result*
Abramowitz *et al*. [46]	TPUS vs RF transponders RMS difference / standard deviation between 4D-TPUS and RF transponders during treatment	RMS ± SD mm: AP: 0.1 ± 0.8 mm LR: 0.1 ± 0.4 mm SI: 0.2 ± 0.55 mm
2018 Han *et al*. [4]	TPUS vs EPID TPUS-measured translations of fiducial markers projected into the plane of the EPID and compared to EPID-measured motion.	Mean ± SD displacements: AP: -0.6 ± 1.1 mm LR: -0.1 ± 0.7 mm SI: 0.3 ± 0.7 mm
Grimwood *et al*. [48]	TPUS vs EPID TPUS-measured translations of fiducial markers projected into the plane of the EPID and compared to EPID-measured motion.	Median difference: 0.6 mm 95% LoA: 2.6 mm Median absolute error: 1.0 mm

2.6 Patient positioning and interfraction motion management for prostate EBRT

2.6.1 Standard methods of interfraction motion management

According to the IAEA Human Health Report no. 11, *Strategies for the Management of Localized Prostate Cancer: A Guide for Radiation Oncologists* [49], the current minimum standard of care for patient positioning for prostate EBRT is to use an electronic portal imaging device (EPID) to match the bony anatomy of the pelvis to a digitally reconstructed radiograph (DRR) derived from CT simulation data. While this is considered more accurate than the previous method of aligning to

tattoos marked at simulation time, there was some evidence to suggest it yielded only a marginal improvement. According to Beltran *et al*. [25] this approach made no difference to the margin expansion calculation in the superior-inferior (SI) and anterior-posterior (AP) directions. They did show, however, that when combined with intraprostatic gold seeds a large margin reduction could be achieved and concluded that intrafraction prostate motion was a limiting factor on margin reduction. In the absence of fiducial markers, soft-tissue matching of 3D CBCT to simulation CT can be employed with similar results [50], but with concomitant imaging dose.

While much less widely adopted, pre-fraction ultrasound imaging for prostate patient position correction has been around for some time. Development of the B-mode acquisition and targeting, or BAT system was reported by Lattanzi *et al*. almost two decades ago [38, 51]. The BAT system utilises a handheld ultrasound transducer to acquire orthogonal planes of the prostate transabdominally while being optically tracked via stereoscopic infrared cameras. The Clarity 3D TAUS built on this concept. Rather than imaging two orthogonal planes, multiple images acquired via a freehand sweep of the 2D probe are reconstructed into a volumetric tomograph. Furthermore, the Clarity system introduced TAUS imaging to the simulation process to eliminate the effects inter-modality imaging [52]. Reviews of these systems are mixed; for example, Lattanzi *et al*. concluded that shifts determined by the BAT system were comparable to those determined via CT, whereas Robinson *et al*. [53] concluded that the geometric accuracy of the Clarity 3D-TAUS system was not sufficient for it to be used for IGRT.

2.6.2 Interfraction motion management using Clarity Autoscan 4D-TPUS

The Clarity Autoscan 4D-TPUS system has been designed to reduce or eliminate several sources of error in the earlier systems. Transperineal imaging produces improved image clarity and reduces speed-of-sound variations compared to transabdominal imaging. The robotic sweeping mechanism eliminates the possibility of insufficient lateral sampling as discussed by Molloy *et al*. [52] in the first report of the American Association of Physicists in Medicine (AAPM) ultrasound task group. The integrated couch fixation platform and “Live Guidance” visual software cue for probe position reproducibility (Figure 4) reduces the effect of variations in tissue displacement due to varying probe pressure.

The standard workflow for the Clarity Autoscan system involves a pre-fraction ultrasound image which is registered to an ultrasound image acquired during treatment simulation. Molloy *et al*.

emphasised the importance of using the same imaging modality for treatment simulation as for interfraction motion management. They acknowledged the existence of speed of sound variation and refraction artefacts in ultrasound imaging. However, they concluded that providing there has not been a significant anatomical change (e.g. bladder or rectum filling, change in probe pressure) these may be neglected if the pre-fraction ultrasound image is registered to an ultrasound image acquired during treatment simulation. Additionally, they reported that prostate volumes contoured on CT are consistently larger than on ultrasound and point to this as a further reason for registration of pre-fraction ultrasound to simulation ultrasound.

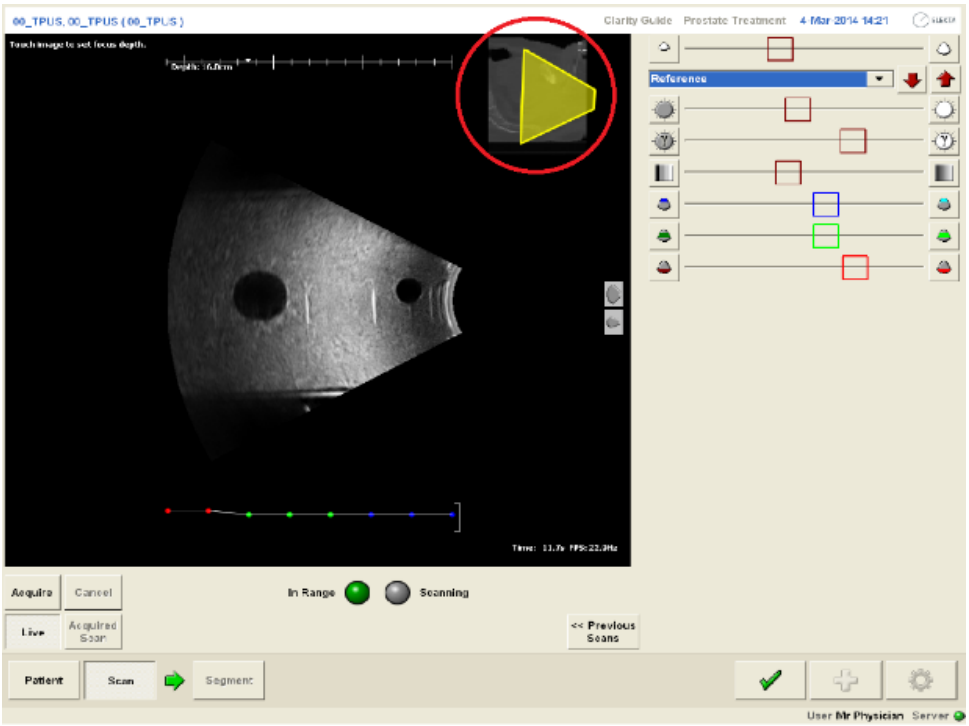

Figure 4: Clarity screenshot with Live Guidance feature for probe position reproducibility highlighted

Fargier-Voiron *et al*. [54] compared pre-treatment shifts derived from pre-fraction CBCT registered to simulation CT (CBCT/CT) and those determined by pre-fraction TPUS registered to simulation TPUS (TPUS/TPUS). They reported a high concordance between CBCT/CT localisation and TPUS/TPUS localisation. Furthermore, they examined inter-operator variability (IOV) and the impact and variability of probe pressure, providing extensive statistical analyses. They found the effects of IOV to be almost identical between the two modalities. While undue probe pressure is still identified as a source of uncertainty in TPUS, the work makes no reference to the "Live

Guidance" software feature and one wonders if this was added following this publication. Critically, they reported that the correlation between CBCT and TPUS localisation was larger than between CBCT and marker-based 2D kV or MV systems.

Zaragori *et al*. [55] calculated treatment margins for 4 different prostate motion management arrangements: 1) CBCT/CT with fiducial markers (FM) for interfraction motion only; 2) CBCT/CT with FM and intrafraction monitoring (IFM) using 4D-TPUS; 3) TPUS/TPUS interfraction motion management with IFM; and 4) TPUS/TPUS corrected by average offset from CBCT/CT over first 5 days, IFM. They found that IFM (2) enabled significant reduction in the already small margins calculated for the "gold standard" approach (1). They also found that correcting the TPUS/TPUS setup based on five days of CBCT/CT localisation (4) enabled treatment margins to be reduced by approximately one third. Trivedi *et al*. [56] compared prostate gland localisation using TPUS to CT and found no significant statistical difference between reported positions from the two modalities, however they cautioned that further evaluation was needed before it was adopted for IGRT.

2.6.3 Dosimetric impact of motion and intervention

Over the past decade a number of retrospective studies have been conducted examining the dosimetric impact of intrafraction prostate motion [57-62]. Each used intrafraction monitoring data acquired via Calypso, kV or MV imaging to perform 4D dose reconstruction post-delivery to assess dose coverage of the CTV, with one study also considering the dose to the organs-at-risk (OAR). Chapter 6 of this work will attempt to examine several aspects of the dosimetric impact of beam suspension and intervention based on intrafraction monitoring with the Clarity Autoscan 4D-TPUS during physical dose measurements *in silico*.

Chapter 6 will also attempt to augment the work of Jermoumi *et al*. [63] who reported on the effect of beam gating on treatment accuracy of an Elekta linear accelerator. Their work focused on Elekta's Active Breathing Coordinator (ABC) solution for the Deep Inspiration Breath Hold (DIBH) technique for left-sided breast patients, in combination with the Elekta Response gating kit. They used open field measurements and SBRT plans delivered to an ion chamber array to assess the effect on the dose distribution of different gating windows, monitor units and beam hold times. The Response gating kit can also be used with the Clarity Autoscan system, so some aspects of this arrangement will be assessed.

2.7 4D-TPUS Quality Control

Tomé *et al*. [39] commented on the lack of attention directed toward quality assurance amidst the proliferation of new IGRT systems in 2002. They presented an anthropomorphic phantom test that simulated well the clinical workflow, however it did not produce any image quality or system constancy metrics that might indicate a gradual degradation of system components. The AAPM ultrasound task group had released its first report in 1998 [64] enumerating quality control tests for real-time B-mode (i.e. brightness-mode or 2D-mode) ultrasound in the diagnostic setting. They presented a comprehensive list of recommended tests, including some that are now obsolete concerning film processors and cathode ray display monitors. However, other tests such as for image quality have remained relevant and so were adopted in subsequent guidance by the AAPM in task group reports number 128 [65], which focuses on brachytherapy applications, and report number 154 [52] dealing with ultrasound guidance for prostate EBRT.

Report 154 was prompted by the emergence of transabdominal ultrasound IGRT. As the Clarity Autoscan 4D-TPUS system evolved from Elekta's Clarity 3D TAUS IGRT system, this report is particularly relevant to the 4D Autoscan system. Therefore, with the exception of inter-operator variability considerations regarding the hand-held probe for the Clarity 3D system, the quality control program developed in the Appendix of this work will draw heavily from report number 154 while making reference to the earlier work.

Chapter 3: Determining the feasibility of using a scanning tank for Clarity Autoscan verification

3.1 Introduction

The ability of the Clarity Autoscan 4D Transperineal Ultrasound system to track intrafraction target motion has been investigated in several other studies [1-4, 34, 47, 48, 54], however in each study only small deviations from a normalisation position were examined. In clinical practice it is not always possible to perfectly position the probe to be centred and aligned to the coordinate system of the linear accelerator due to patient anatomy. It would therefore be useful to assess the tracking ability of the system throughout a larger volume encompassing not only worst-case clinical prostate motion but also allowing a further margin to allow for a normalisation position that is not located in the centre of the ultrasound imaging volume.

In this chapter the feasibility of using the scanning system in a water tank intended for reference dosimetry of a linear accelerator to verify the near-real time position of the prostate during external beam radiotherapy was determined. To do so, the clinical process was replicated using phantoms, with the exception of the treatment planning stage in the treatment planning system. Hence it was necessary to complete the three stages of simulation, registration/contouring, and "treatment". This will facilitate a qualitative assessment of the scale of the refraction distortion would assist in the development of a refraction correction algorithm in Chapter 4.

Patient simulation involves both a 3-dimensional transperineal ultrasound acquired using the Elekta Clarity Autoscan system and a conventional CT scan, both performed with the patient in the treatment position in a CT-Simulator. To reduce the potential for patient or target motion between scans they are conducted as temporally close to one another as possible. Both datasets are then sent to the Clarity Auto-Fusion and Contouring (AFC) workstation where the ultrasound reference dataset is registered to the CT planning dataset and the prostate is contoured. Finally, at the linac the reference ultrasound dataset including contour information is retrieved from the Clarity server and registered to the daily ultrasound acquisition. It is at this point that shifts can be made based on the daily registration. Alternatively, another method can be used to determine shifts, such as CBCT, and the Clarity shifts can be zeroed before commencing treatment. Clarity refers to this second approach as non-IGRT mode – this is a slight misnomer as image guidance is still being used for setup, it is just not the Clarity system being used. Regardless, at the commencement of

treatment the prostate position has been normalised to report zero offsets in each cardinal direction.

3.2 Method

3.2.1 Simulation – Ultrasound

The scanning tank was positioned on the patient couch inferiorly to the gantry of the CT-Simulator in a similar manner to the linac setup shown in Figure 5. It was not possible to have the tank inside the CT bore and still position the Clarity probe near to the centre of the CT field of view. This was because the couch would need to be set at its lowest position making the probe too low to be seen by the stereoscopic cameras mounted to the ceiling.

In order to replicate the Clarity 3-dimensional simulation scan, a crude prostate analogue was constructed by impaling a table tennis ball on a brachytherapy needle and suspending it in the water of the scanning tank. This approach was only used for the ultrasound component of the initial simulation session where no phantom movement was needed: more rigid arrangements were used for later studies. One end of the brachytherapy needle was wrapped with multiple layers of micropore tape to pack out the thickness sufficiently to be held by the scanning system that is designed to hold farmer-type ionisation chambers.

The Clarity probe was mounted to its base unit, which was positioned sufficiently close to the tank to permit the Clarity probe to be placed against the external inferior wall of the tank. Ample ultrasound gel was applied between the front of the probe and the tank wall. Every effort was made to align the probe to the external lasers to minimise the possibility of asymmetric refraction effects. However, as it is not necessary clinically to align the probe to the lasers the probe housing is only designed for ergonomics and aesthetics with no external alignment markings, so this was difficult to achieve with great accuracy. The simulation ultrasound was acquired and sent to the AFC workstation.

3.2.2 Simulation – CT

It was not necessary to have a prostate analogue in the simulation CT scan. The ultrasound containing the analogue can be registered to a CT dataset on the AFC workstation and the "prostate" contoured on the ultrasound only. Hence a stack of solid water – typically used for constancy measurements of linear accelerator radiation output – was positioned on the couch to

simulate the patient and scanned using the departmental scanning protocol for prostate external beam radiotherapy. This too was transferred to the Clarity AFC workstation to become the reference CT dataset for fusion with reference ultrasound dataset.

3.2.3 Fusion & Contouring

As mentioned above, the simulation or reference ultrasound scan was registered to the simulation CT on the AFC workstation. While there were no common land marks to register to, for the purposes of this work it was only necessary to have the prostate analogue of the ultrasound somewhere in the middle of the solid water in the CT dataset. However, this did require a significant superior shift in the ultrasound dataset due to the ultrasound scan being performed outside of the CT gantry. Ordinarily the prostate would then be contoured based on information from both datasets, however in this case the 'prostate' was contoured on the ultrasound dataset alone and the contour copied to the CT dataset. Once approved, the reference ultrasound and contour information, or "positioning reference", was then sent to the Clarity server so that it could be retrieved by the mobile cart for 'treatment' at the linac.

3.2.4 "Treatment"

The PTW MP3-XS scanning water tank is conveniently small enough to be placed on top of the treatment couch of a linear accelerator for most reference dosimetry applications, but is too small for profile measurements of fields larger than approximately 10 cm x 10 cm. The Clarity validation measurements reported herein could conceivably be performed in a full-size scanning water tank however it would take a little more ingenuity to position the Clarity Autoscan probe against the side of the tank in the treatment orientation.

The brachytherapy needle was not rigid enough to reliably transfer the programmed movements of the tank scanning system to the prostate analogue. As a result, the prostate analogue used for the simulation processes was different from those used for the positional data acquisition on the linear accelerator for the remainder of the project. This is not expected to have had any bearing on the outcome of the studies since the intrafraction monitoring is relative to the pre-treatment reference scan at the linear accelerator and any offsets are zeroed out before treatment commences.

A more rigid prostate analogue was constructed for the 'treatment' stage by boring a hole into a rubber ball with a diameter of approximately 20 mm and inserting the housing of a ballpoint pen into the hole. The pen housing enabled the ball to be vertically offset by more than 100 mm from the aluminium scanning mechanism to prevent it from interfering with the ultrasound images. The rubber ball was chosen for its ready availability and the assumption that it would have similar properties to the water, yet different enough to be differentiated in the acquired images.

Figure 5: Experimental setup for Chapter 3 – treatment

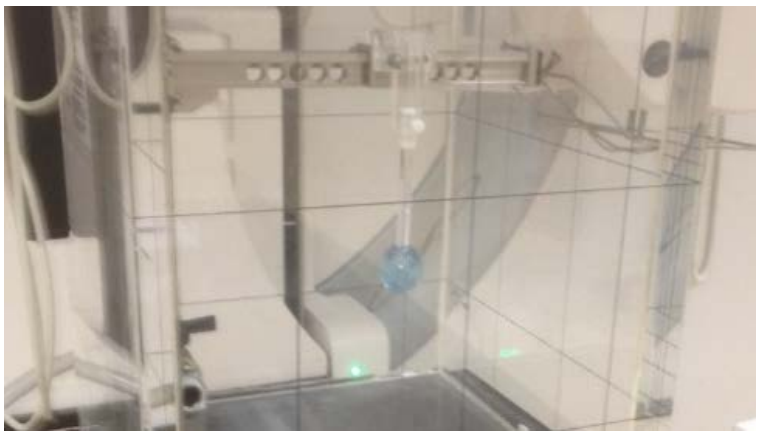

Figure 6: Empty MP3-XS tank on treatment couch with rubber ball

The tank was filled with water before levelling with a clinometer and aligning to the room lasers in case the weight of the water caused any displacement due to sagging of the treatment couch. The scanning mechanism was then used to position the rubber ball to also coincide with the intersection of the room lasers. The Clarity probe was then positioned as for the simulation, taking care to keep the probe as orthogonal as possible to the surface of the tank and at a height that would have the ball roughly centred in the sagittal plane relative to the probe field-of-view. The couch position indicator (CPI – not shown in images) was then placed on the couch beside the Clarity probe, in view of the cameras – it was not necessary to affix it to the couch as there would be no patient to potentially bump it during acquisition.

The Clarity system was then powered on and automatically connected to the server. Once logged in, the "non-IGRT mode" box was checked to indicate that Clarity would not be used for 'patient' positioning, and the 'patient' created at the simulation stage was selected from the patient list. The live scan mode was then initiated in which the transducer is not sweeping but held stationary within the probe at its central position, and a pseudo-sagittal plane repeatedly imaged and displayed in real-time. This 2-dimensional "Live scan" mode is used solely to reposition the probe as close as possible to where it was at the time of simulation, as detected by the infrared camera and reflector system. Additionally, the software provides a repositioning aid (Figure 4) which can help in achieving the simulation position.

Once the probe was positioned, tracking mode was initiated. The system then began the sweeping scans of the 4D mode acquisition. After a brief interval a system prompt was displayed requesting notification of when IGRT had been completed. For a clinical patient treatment this would be when orthogonal kV images or CBCT would be acquired and appropriate shift calculated by comparison to simulation CT. Since the prostate analogue was visible without the need for imaging this step was skipped by confirming IGRT completion in the prompt. A second prompt then appeared requesting confirmation of when the shifts had been made. Since no shifts were actually made, this prompt was also immediately confirmed – it was at this point that the displayed positional offsets in each of the cardinal directions were zeroed out (I.e. normalised).

The system was now in its continuous monitoring mode ready for treatment to commence; however, rather than beaming on, the scanning system of the tank was used to displace the prostate analogue from the normalisation point in each of the cardinal directions and the reported

displacements viewed on the Clarity display monitor. A 30 mm displacement of the prostate analogue was chosen in order to encompass a worst-case motion of the prostate during treatment of up to 20 mm, plus a further 10 mm to allow for clinical probe positioning that is not perfectly aligned to the coordinate system of the linear accelerator. The probe often has a slight translation and/or rotation relative to the superior-inferior axis of the linear accelerator coordinate system due to uncertainty in operator positioning and proximity to the patient's thighs.

3.2.5 Confirmation of tracking 30 mm lateral offset using QC phantom

Finally, in order to confirm that the Clarity system could indeed accurately track an object out to a lateral displacement of up to 30 mm, the system was used to monitor the vendor-supplied phantom used for daily QC and room setup calibration procedures while the phantom was manually moved laterally by 30 mm in first the left then right direction. A large sheet of graphing paper was taped to the treatment couch beneath the phantom (Figure 8 and Figure 9) enabling the phantom to be positioned to within approximately ±0.3 mm.

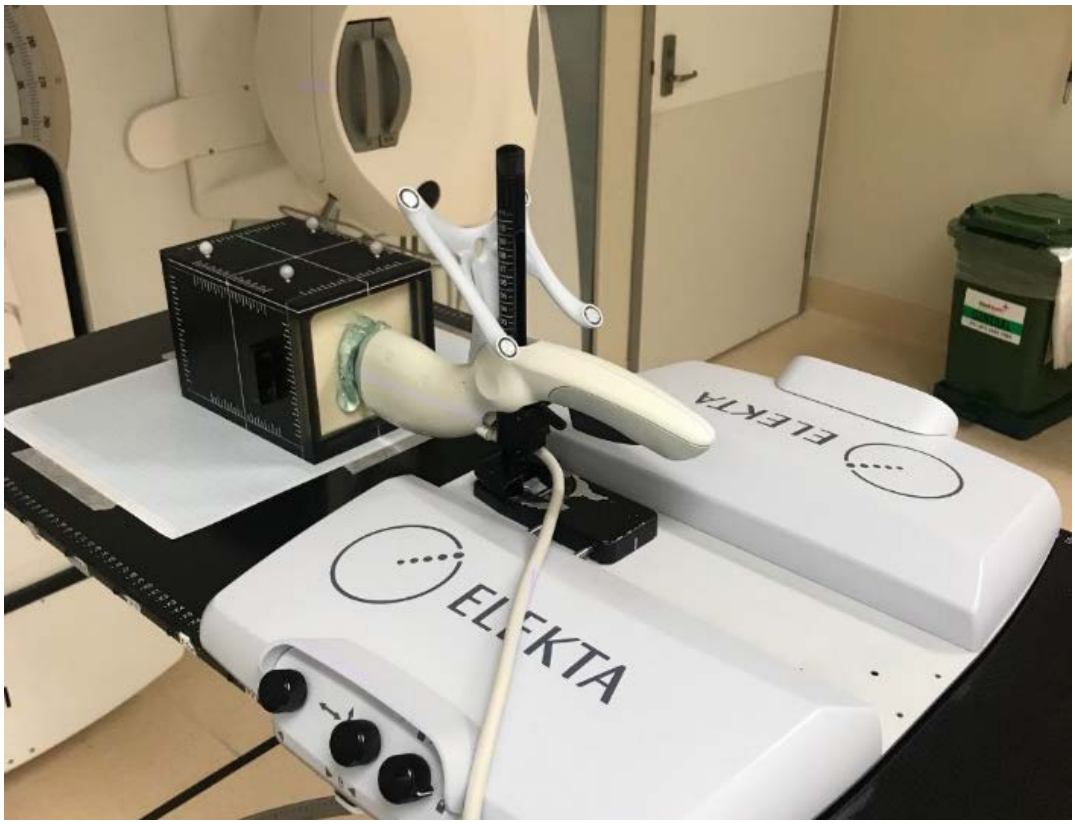

Figure 7: tracking the Clarity QC phantom on graph paper

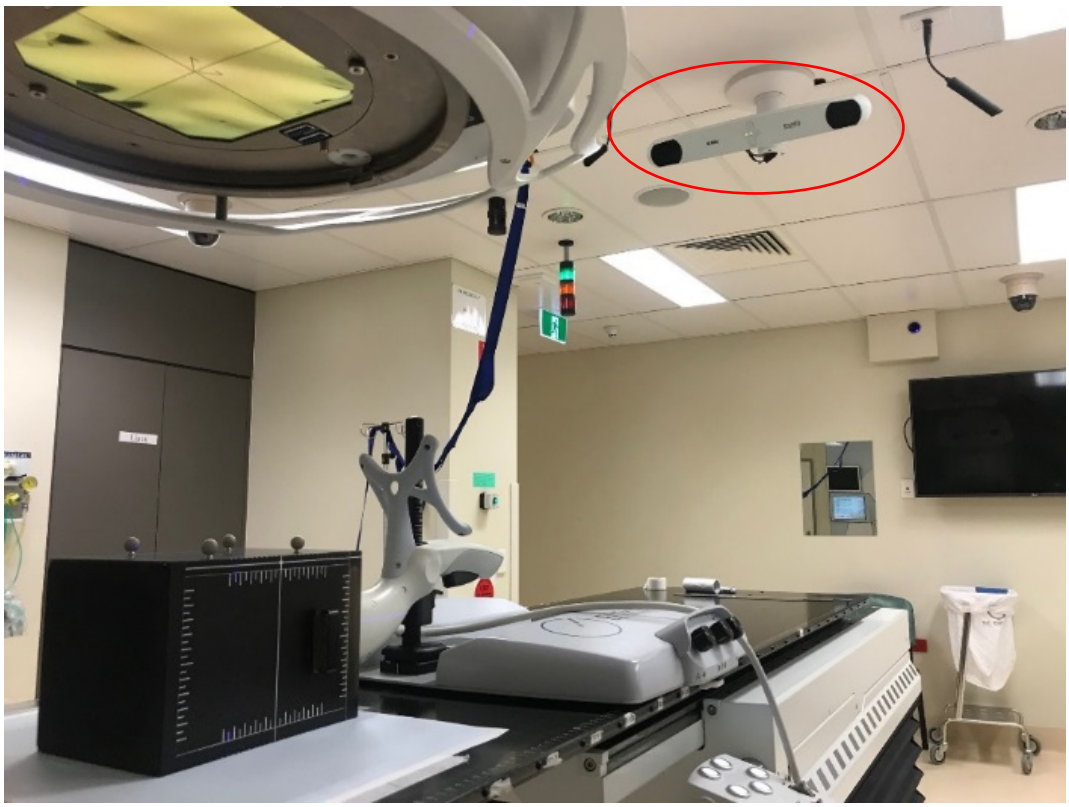

Figure 8: Reverse angle of setup showing tracking cameras suspended from ceiling

3.3 Results

The prostate analogue within the scanning water tank was driven laterally by 30 mm in both directions as described above, however the displacement reported by the Clarity system was only 24.5 mm in each direction. In order to confirm that this difference was primarily due to refraction in the wall of the scanning tank, the Clarity QC phantom was monitored while it was manually displaced by 30±0.3 mm in both lateral directions. Clarity reported displacements of 30.2 mm and 30.0 mm in the left and right directions respectively.

3.4 Discussion

3.4.1 Tracking speed limit

The first attempt at moving the prostate analogue was to move it 30 mm toward the patient left (assuming head-first supine or HFS orientation), however the system lost tracking within a few seconds. It became clear that in order to move the analogue and maintain tracking, either the step size or the speed of the movement had to be reduced. It was easier to make smaller steps than to reduce the speed of the motion in the tank control software. It was also evident that the further the

analogue was from the normalisation point the smaller the size of the steps required. Near the middle, steps of 10 mm could be made while maintaining tracking whereas beyond 20 mm, the steps had to be reduced to 5 mm. This became important in the subsequent studies when programming multiple positions so that whole 'profiles' could be acquired without interruption.

Maintaining tracking will also be affected by the size of the tracking volume. The software essentially records the voxel intensity pattern within the contoured volume to be tracked, plus a margin of 2 cm, in the pre-treatment reference scan [1]. While the system is monitoring the target the software repeatedly looks for this voxel intensity pattern to identify the target location. It seems that continuous tracking is more likely the greater the overlap of this pattern between subsequent volume acquisitions. A larger tracking volume will have a greater chance of overlapping with itself in subsequent reconstruction updates and therefore may be more likely to maintain continuous tracking.

3.4.2 Position update delay

While the volume is continuously being reconstructed to include every new slice that is acquired, the finite sweep time means that the reported position only updates on average every 2.5 seconds. While this was already known it was not anticipated that occasionally, if the object being tracked is significantly displaced laterally and the sweep happens to pass it by just as it is moving, registering little or no change in position, the position may only update as much as 5 seconds later. This, again, becomes useful to know when programming movements for sequential position acquisition.

3.4.3 Offset scaling

As a result of the tracking speed limit found above, the analogue was moved in 5 mm steps until 30 mm to patient left was reached, pausing between each step to ensure the new position had been picked up by the system. The position reported by the Clarity system at this point was approximately 24.5 mm or about 20% less than the programmed offset. As described previously, it was anticipated that the PMMA wall of the tank would be the main impediment to using the tank for this purpose since its density is significantly higher than that of water. Furthermore, by confirming that the Clarity system was able to accurately track an object within the Clarity QC phantom while displaced by ±30 mm laterally, the Clarity-reported value of 24.5 mm could then be used to calibrate the algorithm developed in Chapter 4.

3.4.4 Offset symmetry

The analogue was then moved to positions 30 mm either side of the normalisation point in the patient right, anterior and posterior directions. It was observed that the reported offsets at each position agreed with that at the patient left to within a small margin (approximately ±0.2 mm). The agreement between the reported lateral and vertical (anterior-posterior) offsets was unexpected since the probe is comprised of a 2-dimensional, vertically oriented transducer that sweeps laterally. Hence the transducer elements are more dispersed in the vertical direction than laterally and it was thought that there would be more refraction seen in the lateral direction than the vertical direction. This result gave added confidence that a relatively simple, non-directionally dependent correction algorithm which treats the transducer as a point source may be useful.

The analogue was then moved to positions 30 mm from the normalisation point in the superior and inferior directions. It was observed that there was minimal difference between the nominal and reported positions at these locations, with the larger of the two at the inferior position nearer to the probe. This was as expected since the largest deviations due to refraction should be seen laterally or vertically, with increasing angle away from the superior-inferior axis. The differences along the superior-inferior axis are due to the small difference in time-of-flight correction along the 'ray' path as there is no refraction occurring. Furthermore, since the programmed displacements were relative to a normalised point approximately 70 mm from the transducer, the bulk of the offset due to differences in time-of-flight had already been zeroed out of the measurements.

3.4.5 Prostate analogue distortion

The assumption of the ultrasound imaging system that the speed of sound throughout the imaged volume is a constant 1540 m/s caused the prostate analogue to be visibly elongated, even when centred (Figure 9, B). At higher angulations the elongated prostate analogue appeared to be rotated relative to the centred image (Figure 9, A and C). This may have been caused by differential refraction across the volume at higher angles away from the sagittal plane as well as the sound waves reflecting off both the front and the rear surfaces of the prostate analogue relative to the source of the sound waves. It is possible that this apparent distortion could have a negative impact on the ability of the software to accurately calculate the centroid position of the tracking volume.

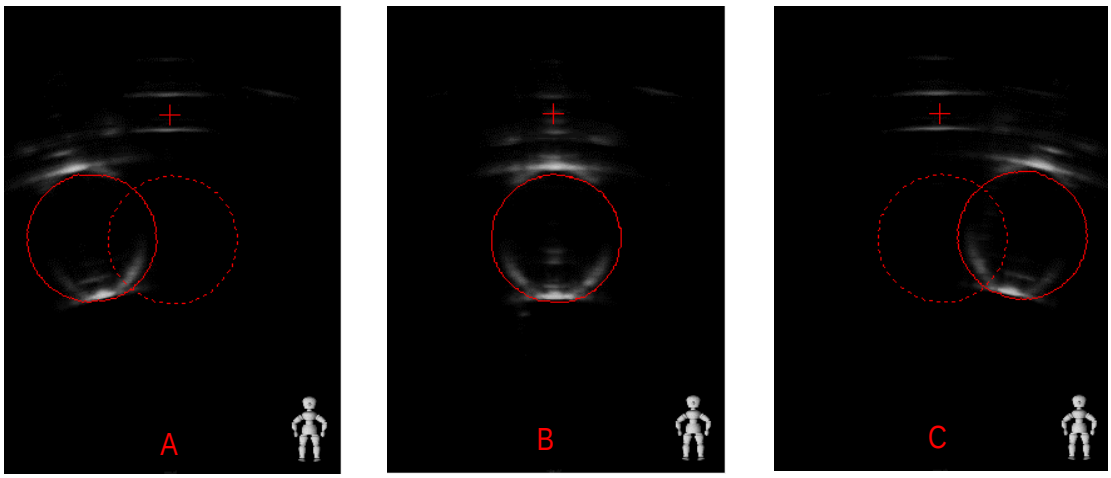

Figure 9: Geometric distortion due to time-of-flight and refraction in PMMA

3.4.6 Summary

The purpose of this first study was to determine whether a prostate analogue could be reliably tracked with the Clarity Autoscan 4D transperineal ultrasound system whilst attached to the scanning mechanism of a dosimetry water tank. If so, this arrangement could be used to validate the prostate position reported by the system. It was found that it was possible to do so, but that refraction of the sound waves in the wall of the scanning tank produced significant positional inaccuracy. In order to use the scanning tank to verify the reported positions of the Clarity Autoscan system, a correction algorithm would need to be developed to correct for the distortion due to refraction. However, the observations suggest that a simple bi-layer refraction correction which treats the transducer as a point source and receiver might be useful.

This study has confirmed that it is possible to track a prostate analogue within a PMMA water tank. The discrepancies between actual surrogate motion and detected motion will be used to develop an algorithm to correct for the refraction in the tank wall and in programming the data acquisition to test the algorithm.

Chapter 4: Position correction algorithm for refraction in 2-Dimensions

4.1 Introduction

As shown in Chapter 3, ultrasound refraction in the PMMA wall of the scanning water tank introduced significant geometric error when attempting to validate the Clarity positioning system. Hence the purpose of this second study was to develop a two-dimensional (2D) correction algorithm that could account for refraction in the PMMA tank wall and phantom water, and then to compare corrected Clarity positional measurements with programmed displacements along each axis as reported by the Clarity system: X (Superior-Inferior or longitudinal), Y (Left-Right or lateral) and Z (Anterior-Posterior or vertical). The algorithm was developed in three phases: derivation, calibration and testing.

The algorithm will initially be calibrated based on the observation from study 1 that a programmed lateral offset of 30 mm was reported by the Clarity Autoscan system as approximately only 24.5 mm. Under certain assumptions a 2D algorithm would be sufficient to account for any offsets along these axes due to refraction, so positional data were collected in each of the three axes to test the algorithm. Each series of axial measurements served a different purpose: the lateral 'profile' tested the algorithm in the direction of mechanical sweep of the 2-dimensional transducer array; the vertical 'profile' tested the algorithm in the direction parallel to the transducer array; and the longitudinal 'profile' tested the offset due purely to the thicknesses and speeds of sound of the PMMA and water as there was minimal lateral or vertical offset.

4.2 Method

4.2.1 Derive 2D correction algorithm to account for refraction in PMMA

According to the Law of Refraction, or Snell's law, the angle at which a ray representing the path of light or sound transmitted through a material, θ_t, is given by [66]

$$\theta_t = sin^{-1}\left(\frac{v_i}{v_t} \times sin\,\theta_i\right), \qquad (2)$$

where in the present case v_i and v_t are the speeds of sound in the incident (water) and transmitted (PMMA) materials respectively, and θ_t is the angle at which a ray representing the wave front passes through the transmission material (PMMA). Consequently, if the speed of sound in the transmission material is greater than the speed of sound in the surrounding material, as is the case

for PMMA and water, the transmitted angle, θ_t, between the refracted path in the PMMA and the long axis will be greater than the angle of incidence, θ_i, between the perceived path and the long axis. Figure 10 demonstrates this for a pane of PMMA in water.

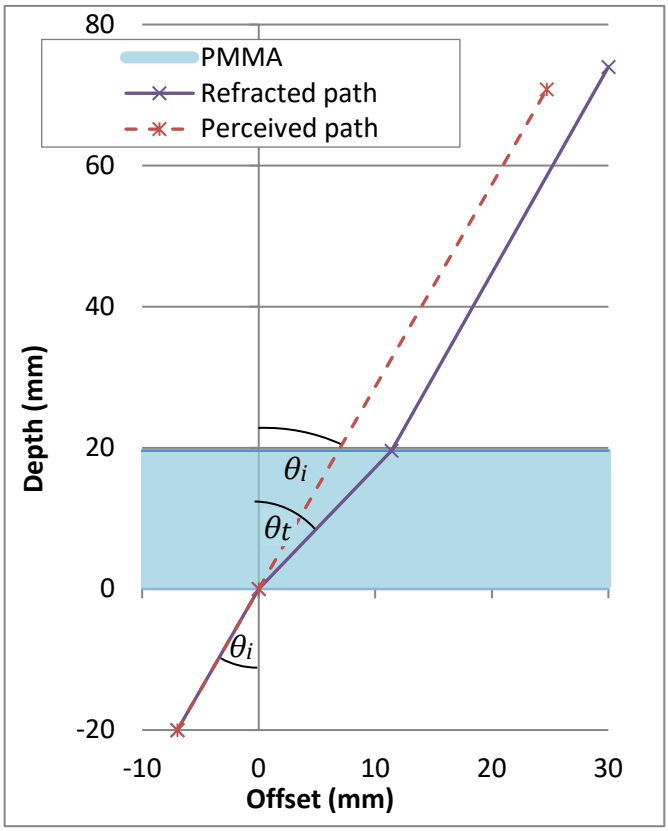

Figure 10: Refraction through a medium ($v_t > v_i$)

I. Assumptions

The 2D correction algorithm is a simple implementation of Snell's Law, but in order to apply it to the experimental setup the following assumptions were required.

A. Uniform thickness of PMMA throughout the tank wall

The thickness of the PMMA wall of the scanning tank contributes to the accuracy of the refraction correction, particularly at more oblique angles of incidence. A series of measurements were made of the thickness of the inferior wall along the top edge at 2 cm intervals from right to left using Vernier callipers. As it was not possible to access the other edges nor the centre, it was assumed that the entire wall of the tank was of the same thickness as the average of the measurements. The average was 19.4 mm, which was slightly less than the nominal thickness according to the

manufacturer of 20 mm. It is conceivable that the wall thickness might vary by as much as a millimetre, so by varying the wall thickness as input in the final algorithm it should be possible to estimate the effect of wall thickness on the final results.

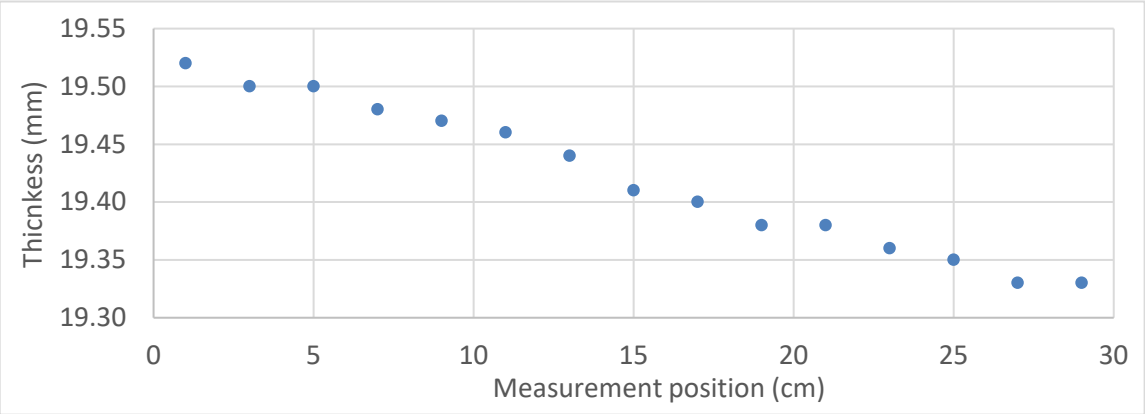

Figure 11: Tank wall thickness at a range of different locations

B. Clarity probe is a point source/receiver of sound 'rays'

Without any knowledge of the internal construction of the Clarity probe it was assumed to be a point-source transmitter and receiver, and that point assumed to be at the point of contact of the Clarity probe and PMMA. Furthermore, it was assumed that the concaved shape of the ultrasound beam does not lead to deviations from a ray-path passing linearly through the Fresnel (near-field) and Fraunhofer (far-field) regions, but instead was treated as one would treat the refraction of light.

This enabled a simple bi-layer arrangement to be derived for the 2D refraction correction in the tank wall and the water. It is impossible to say what effect the internal construction may have on the accuracy of the final model, particularly given the known lateral sweeping action of the ultrasound transducer. Therefore, in subsequent representations of Figure 10 (e.g. *Figure 12*) the portions of the graph below the X-axis will be ignored and only the back (superior) surface of the PMMA will be displayed.

C. Clarity probe central axis aligns with scanning tank longitudinal axis

There was potential for a systematic error if the alignment of the longitudinal axis of the Clarity coordinate system did not perfectly coincide with the longitudinal axis of the programmed motions in the scanning tank. This is because the origins of both the Clarity and scanning tank coordinate systems are redefined for each session 'pre-treatment' through following steps:

i. Tank is positioned and levelled to align to the room lasers;
ii. 'Prostate' positioned to isocentre as defined by lasers;
iii. Tank coordinate system zeroed so that its origin is at isocentre;
iv. Clarity probe aligned as closely as possible to the room lasers with the 'prostate' in the centre of its FOV;
v. Clarity coordinate system zeroed so that its origin is at isocentre and therefore coincides with the tank scanning system origin.

The *orientations* of each coordinate system, however, are established differently: The Clarity co-ordinate system orientation is predefined by the room setup calibration process that is only performed at installation, when the lasers are adjusted, or the cameras have moved; whereas the scanning tank orientation is determined by the tank levelling process performed during the experimental setup. Hence it is possible that the longitudinal axes of the Clarity system and the scanning tank will not be perfectly parallel, and that the reported positions due to movements in the longitudinal direction may display an offset that will be interpreted as a small refraction which may not actually exist. While this was noted, there was no way of measuring whether they were parallel during the setup; all that could be done was to visually align the probe to the room lasers as best as possible with the prostate analogue roughly centred in the Clarity FOV. It was assumed that the resulting effect would be minimal.

D. Distortion of the prostate analogue at more oblique angles has no effect on reported tracking position

Figure 9 in Chapter 3 showed how the prostate analogue was distorted due to refraction and the time-of-flight artefact in the PMMA. This is expected to have a negative effect on the ability of the Clarity system to accurately determine the centroid location of the prostate analogue as it can only determine translations and rotations, not distortions. Therefore, since the magnitude of this error cannot be determined, it will be assumed that it will either be negligible or will be adequately compensated for by using a slower-than-expected speed of sound in PMMA as a calibration factor (see section IV.C).

E. Angle of incidence detected by the probe equal to the refracted angle in water

When calculating the angles of refraction, all offsets and angles are relative to the ultrasound source/detection point at the exterior face of the tank wall, at the origin in *Figure 12*. In the point

source approximation, it is assumed that the layer below the origin, effectively within the probe, is water (I.e. the negative portion of the depth axis in Figure 10). Therefore, it is assumed that the angle made by a refracted ray path through the water in the tank to the position of the true object will be equal to the angle of incidence as detected by the Clarity system, reported via the positional offsets. For this assumption to hold true the two surfaces of the PMMA must be perfectly flat and perfectly parallel. As it is not possible to measure the thickness across the entire tank wall this cannot be know for certain, however it is regarded as a reasonable approximation.

II. Forward calculation: start with actual position

The problem was first modelled simply as a bi-layer refraction in 2-dimensions, starting with a nominal position of the prostate analogue (green line in Figure 12), and working back through the layers to the origin. Once the refracted path to the true object was found, the 'reported' position could then be projected from the origin using the time-of-flight along the refracted path and the angle made in the water (red line in Figure 12), remembering that the projected path would be assumed to be through soft tissue by the Clarity software.

An iterative approach was used to find the refracted path through the PMMA and the water in the tank (purple line in Figure 12) based on the assumed speeds of sound in water and PMMA. The angle of incidence, θ_i, was found that produced the correct lateral displacement for a given PMMA wall thickness, p, and perpendicular depth to the nominal point through the water only, d_w.

With the source point as the origin (Figure 12), the angle to the true object (angle green line makes with depth axis) is given by

$$\theta_{nom} = tan^{-1}(d/x)\,, \tag{3}$$

where x is the nominal lateral offset and $d = p + d_w$ is the total perpendicular depth to the nominal position.

If we define $R_{i,t} = \frac{v_i}{v_t}$, as the ratio of the wave velocities in each material, then if the angle of incidence (not shown in Figure 12) is equal to the angle of the ray in the water (see Figure 10), the total lateral offset, x, is the sum of the lateral offsets in the PMMA and the water. Therefore, from first principles using Snell's Law the total lateral displacement, x, can be found given p, d_w, θ_i and $R_{i,t}$:

$$x = p\,tan\left(sin^{-1}\left(R_{i,t}\,sin\,\theta_i\right)\right) + d_w\,tan\,\theta_i\,. \qquad (4)$$

Since $R_{i,t}$, p and d_w, are constant for a given position, an iterative method can be used to find the angle of incidence, θ_i, which yields the expected value of x at that position as mentioned above.

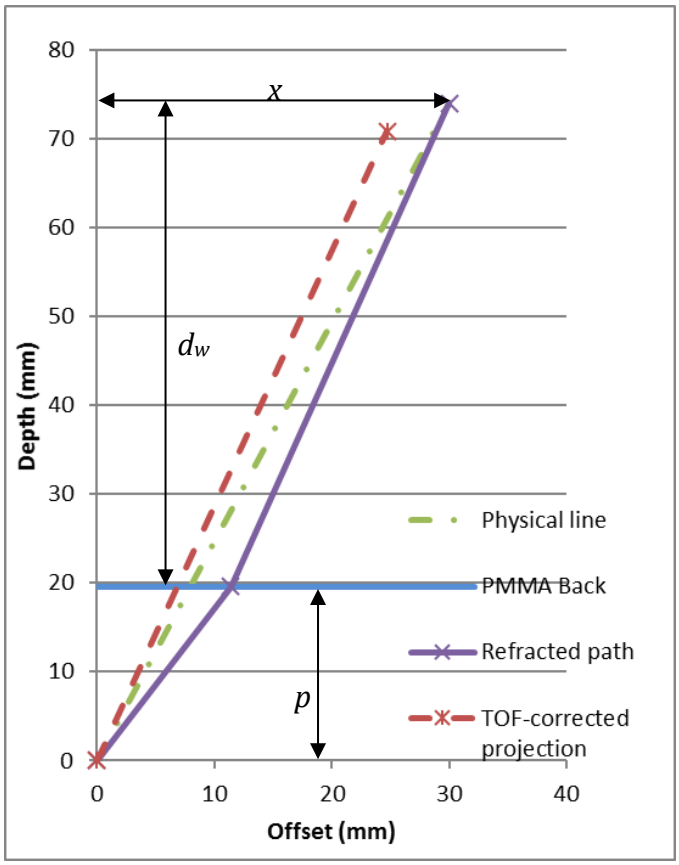

Figure 12: Bi-layer 2D refraction model

Once the angle of incidence has been determined, the angle that the ray takes through the tank wall material can be readily calculated from Eq. (2). Using these angles and the perpendicular depths in the PMMA and the water from Eq. (3), the lengths of the two segments of the refracted path through the PMMA and the water can be calculated.

Once the segment lengths are known, the time taken for the wave to traverse the refracted path – or "time-of-flight" – can be calculated by dividing by the known wave velocities in each material. Finally, using the total time-of-flight along the refracted path, the angle of incidence and the standard speed of sound in soft-tissue, v_{st} = 1540 m/s, the position at which the ultrasound system

will ‘perceive’ the tracking volume and the time taken for the wave to arrive there can be calculated. This is the red line in Figure 12.

III. Reverse calculation: start with US-measured position

The forward calculation served to frame the problem without any proper data having been collected, by enabling the calculation to start from a known, nominal position. However, to implement a correction to measured data the algorithm needs to start with the ‘incorrect’ position and from it find the nominal position. So, the forward calculation was reverse-engineered to find a usable correction method.

The perceived distance to the Clarity origin by the ultrasound system will differ from the nominal value due to the increased speed of sound in the PMMA (and a marginal difference between that of water and soft-tissue), i.e. the ultrasound system will underestimate the physical depth of the Clarity origin because of the reduced time-of-flight, t_{origin}, since the average of the wave velocities in the PMMA and water are faster than the standard speed of sound in soft tissue. Therefore, the ultrasound-measured depth to the Clarity origin, d_{US}, had to be calculated first, by calculating the sum of the times-of-flight through the PMMA and water to the nominal depth, d, then multiplying by the speed of sound in soft tissue:

$$d_{US} = v_{st} \times \left(p/v_p + d_w/v_w\right). \tag{5}$$

The angle of incidence is then just

$$\theta_i = tan^{-1}(x/d_{US}) \tag{6}$$

and the total time-of-flight from the model origin to the reported location is

$$t_{tot} = \frac{\sqrt{x^2 + {d_{US}}^2}}{v_{st}}. \tag{7}$$

The transmitted angle through the PMMA, θ_t, can be determined from the angle of incidence, θ_i, and the thickness of PMMA, p, is a model constant; therefore, the path length through the PMMA at the angle θ_t is

$$l_{PMMA} = p/cos\,\theta_t\,, \tag{8}$$

and the coordinates of the exit point of the ray from the back of the PMMA are

$$(x_{exit}, y_{exit}) = \left(\frac{\theta_i}{|\theta_i|} \times \left({l_{PMMA}}^2 - p^2 \right)^{\frac{1}{2}}, p \right). \quad (9)$$

The time-of-flight through the PMMA at the angle θ_t is

$$t_{PMMA} = l_{PMMA} / v_{PMMA}\,. \quad (10)$$

This can be used to calculate the time-of-flight in the water only, t_w, by subtracting t_{PMMA} from the total time-of-flight, t_{tot}. Once t_w is known the path length in water can be determined by multiplying by the wave velocity in water:

$$l_w = v_w \times t_w = v_w \times (t_{tot} - t_{PMMA}). \quad (11)$$

The angle of incidence can now be used to project into the water from the coordinates of the exit point of the ray from the PMMA (from Eq. (9)) out towards the nominal position. The corrected position of the centroid of the tracking volume can therefore be determined from first principles as a function of θ_i, l_w, l_{PMMA} and p:

$$(x, y) = \left(l_w \sin\theta_i + \frac{\theta_i}{|\theta_i|} \times \left({l_{PMMA}}^2 - p^2 \right)^{\frac{1}{2}}, p + \left({l_w}^2 - (l_w \sin\theta_i)^2 \right)^{\frac{1}{2}} \right). \quad (12)$$

IV. Calibrate in 2D

In order to apply the algorithm to a physical problem several constants had to first be determined: a) the thickness of the PMMA wall of the scanning tank, b) the speed of sound in the water filling the tank, and c) the speed of sound in the PMMA wall of the tank.

A. Tank wall thickness

The PMMA thickness was measured at multiple locations along the top edge using Vernier callipers, as described in Assumption I.A above. It is assumed to be constant at 19.4 mm.

B. Speed of sound in water

The speed of sound in the water filling the tank was calculated using the 5th-order polynomial fit to the temperature-dependent curve described by Marczak in 1997 [67]. The Marczak formulation was compared to two other sources [68, 69] and all were in reasonable agreement with each other within the range of 20°C to 25°C (Figure 13). The Marczak formulation was chosen due to the lack of data between 0 and 22.5 in the Smith and Lawson data, and the unknown origin of the

Engineering Toolbox data. Furthermore, the 5th-order polynomial was assumed to be more accurate than a linear interpolation between the discrete data points of the other two sources.

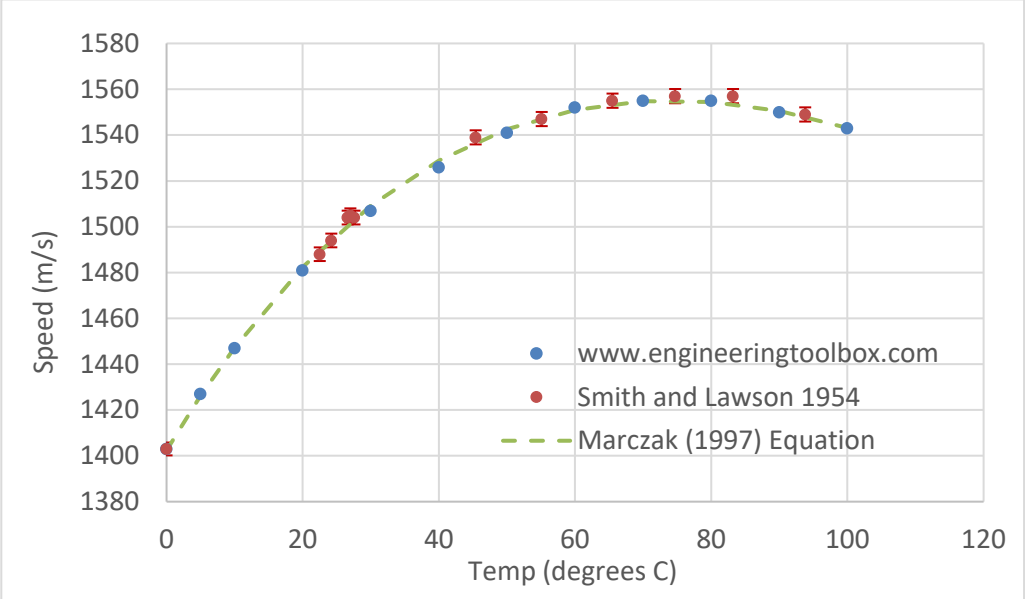

Figure 13: Speed of sound in water as function of temperature

Employing the temperature-dependent determination of the speed of sound in water required the water temperature in the tank to be measured during the data acquisition for the test phase of this second study and for the next study in Chapter 5. This was performed using a NATA-calibrated digital thermocouple that is used routinely for dosimetry measurements in the scanning tank.

C. Speed of sound in PMMA

The speed of sound in the tank wall material is the final unknown in the algorithm as the speed of sound in water is well known, and the physical dimensions of the experimental setup were measured and reported in Chapter 3. Several sources were found for the speed of sound in PMMA, yielding a range of different values. PMMA is also known by numerous trade names including Plexiglas and Perspex, and may also be known as acrylic [70]; however, acrylic does not exclusively refer to PMMA and may also refer to other polymers with similar properties. Table 3 lists the values given by different sources in chronological order of publication.

The IEEE-reported value of 2750 m/s was likely the most reliable for the tank wall material and appears to be supported by Xia *et al*. The value for Plexiglas was assumed to be a typographical

error (i.e. should have read 2700) whereas the value for Acrylic was dismissed as potentially referring to a polymer other than PMMA.

Table 3: Speed of sound in PMMA from various sources including uncertainties where given

Source	*Published*	*Description*	*Wave velocity (m/s)*
US defence nuclear agency [71]	1972	Poly (methyl methacrylate) (PMMA) (Plexiglas)	2270 (elastic) 2470 (longitudinal)
General motors technical centre (for US naval ordinance laboratory) [72]	1972	Polymethylmethacrylate	2690 ± 2%
IEEE conference proceedings [73]	2003	PMMA	2750 (5 MHz, 20° C)
Xia *et al*. [74]	2013	PMMA	2757 ± ≈50 (SD)
Class instrumentation LTD [75]	2013	Plexiglas	1700
RSHydro [76]	2018	Acrylic	1430

The reverse calculation algorithm was solved for v_t = 2750 m/s using a speed of sound in water of v_i = 1488.4 m/s and the physical dimensions as reported in Chapter 3 (see Table 4 below). However, this resulted in an unsatisfactory disagreement with the nominal position of the object (Figure 14 and Table 5).

Table 4: Constants used to solve the reverse calculation

Constant	*Value*
Speed of sound in water, v_i	1488.4 m/s
Total nominal depth, d	74.0 mm
Thickness of PMMA, p	19.4 mm
Perpendicular depth in water, d_w	54.6 mm
Perceived lateral displacement	30.0 mm

The elastic wave velocity reported by Christman *et al*. [71] of v_i = 2270 m/s resulted in a sub-millimetre geometric error. Equation (3) was then solved iteratively to determine the value of the speed of sound in PMMA, v_t, that would minimise the geometric offset, again using the speed of sound in water and physical dimensions from Chapter 3. Assuming the remaining geometric offset could be due to the simplicity of the algorithm or the uncertainty introduced by the above assumptions, it was decided that for the remainder of the work the elastic wave value reported by Christman *et al*. of 2270 m/s would be used for the speed of sound in the tank wall material. This decision was taken with the understanding that it was likely compensating for inaccuracies in the model such as the impact on centroid position calculation discussed later (see section 4.3.4).

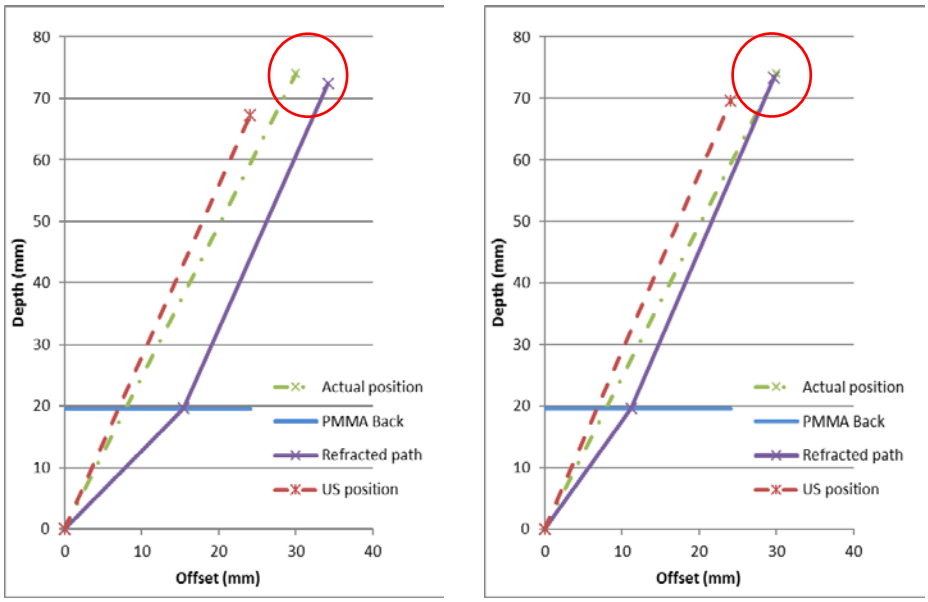

Figure 14: Solutions to reverse calculation with v_t = 2750 m/s (left) and v_t = 2270 m/s (right)

Table 5: Results of the reverse calculation

Speed of sound in PMMA, v_t	*2750.0 m/s*	*2270.0 m/s*	*2301.0 m/s*
Ratio of transmitted to incident velocities, $R_{t,i}$	1.848	1.525	1.546
Calculated angle of incidence, θ_i	19.55°	18.95°	19.00°
Calculated angle of transmission, θ_t	38.18°	29.69°	30.21°
Lateral difference from expected	4.09 mm	-0.39 mm	-0.13 mm
Longitudinal difference from expected	-1.56 mm	-0.60 mm	-0.65 mm
Total geometric offset	*4.38 mm*	*0.71 mm*	*0.66 mm*

4.2.2 Test in 2D

After the initial tests of Chapter 3, version 2 of the prostate analogue involving the rubber ball was rendered unusable after the ball split in two due to the internal pressure of the pen housing. With the necessary development of a new prostate analogue, it was decided to take the opportunity to conduct a more careful end-to-end test including re-simulation.

V. Improved Prostate Analogue

Version 3 of the prostate analogue involved a table tennis ball injected with saline using a syringe. The injection hole was sealed with superglue which also attached a 150 mm Perspex rod to the ball. The rod was of just the right diameter to be held firmly using the PTW Trufix attachment for holding a Farmer-type ionisation chamber in the water tank scanning mechanism. This was a significant improvement over the previous prostate surrogates which each had to be wrapped with numerous layers of micropore tape to be held by the Trufix attachment.

VI. Re-simulation

As described previously the simulation was a two-step process: first the new prostate analogue was scanned with the Clarity ultrasound while held in the scanning water tank, as previously, then the new analogue was removed from the scanning tank and positioned in a smaller water tank with no scanning mechanism for the CT simulation. This was necessary as the scanning mechanism would result in unsatisfactory artefacts during CT reconstruction.

VII. Experimental setup and data collection

A. Software

The experimental setup was the same as described in Chapter 3 with the scanning mechanism connected to a laptop on which the PTW Mephysto software suite was installed (Figure 15). This software has many functions, including the ability to remotely program a series of positions as well as the time spent at each position. Three separate series of positions and pauses were programmed into Mephysto, with a 10 second pause every 2 mm between -30 mm and +30 mm, along each of the longitudinal, vertical and lateral axes. Given that the Autoscan transducer sweeps approximately every 2.5 seconds it was assumed that 10 seconds would be enough time to obtain good data on the Clarity-reported position of the analogue at each position.

Figure 15: Experimental setup for verification of the 2D algorithm showing improved prostate analogue

B. Exporting Clarity position data

In order to accurately compare the nominal, programmed positions to the positions measured by the Clarity system the log of measured positions was downloaded from the Clarity server as a csv file. Each line item in the CSV file has ten data elements as described in Table 6.

C. Data processing

For each series the SecondsFromMidnight, CouchRelativeX, CouchRelativeY and CouchRelativeZ elements were extracted from the .csv file for processing. A start time was chosen to coincide with the middle of the first step in each series and a time increment obtained through trial and error that produced subsequent data points near the middle of each step (see example in Figure 17). Due to the sweeping nature of the data acquisition the steps are not all same width. There were occasionally half steps where the imaging plane had passed over the analogue as it moved to the next position; Therefore, a narrow window of only 2 seconds was used in which to calculate the mean reported position at each step (depicted by the error bars in Figure 16).

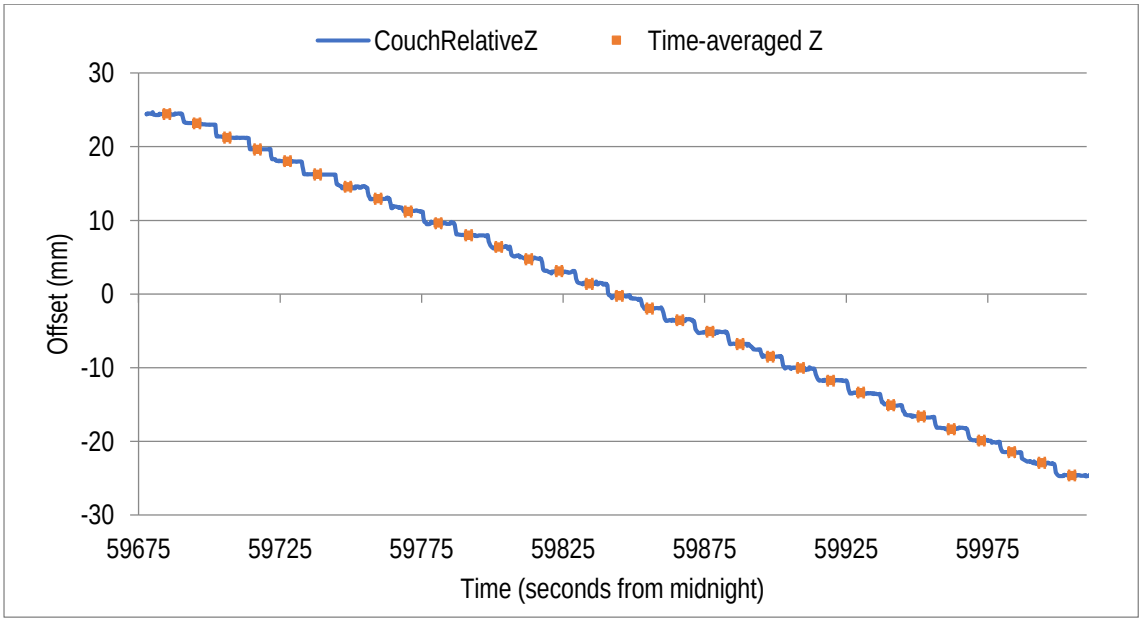

Figure 16: Processing of anterior-posterior positional data showing ranges used for average position calculation

The mean positions in the direction of programmed motion and one other axis were used as input into the 2D algorithm for each of the three datasets (see example in Figure 17). Note that the *Total perpendicular depth* value in the calculations in Figure 17 should be equal to the total physical depth of the centroid position of the analogue from the external inferior surface of the tank, which in the case of this second study was 74 mm.

4.3 Results

The purpose of this second study was to develop from first principles a 2D refraction algorithm to correct the positional measurements as reported by the Clarity Autoscan system when measuring through approximately 20 mm of PMMA. Theoretically the 2D correction could be applied to all points in the sagittal and coronal planes that include the Clarity normalisation point. However, for this phase of the project the 2D correction algorithm was tested using only data collected along each of the three cartesian axes. This made it simpler to correlate any offsets from the programmed positions to displacements in only one axis.

Table 6: Elements of Clarity CSV tracking data file

Element name	*Description*	*Example*
Iso8601time	Date and time of element acquisition in iso-8601 format	2018-06-10t17:09:50.910
SecondsFromMidnight	Acquisition time in seconds since midnight	61790.91
Xshift	Raw superior-inferior tracking position	-1163.07
Yshift	Raw left-right tracking position	-1.61856
Zshift	Raw anterior-posterior tracking position	0.696817
CouchRelativeX	Final superior-inferior tracking position incorporating couch movements using the couch position indicator (CPI)	0.055729
CouchRelativeY	As above for left-right axis	-0.11231
CouchRelativeZ	As above for anterior-posterior axis	-0.2424
Quality	Tracking quality index. Tracking considered poor if less than 0.5, and lost if less than 0.2	0.924072
HasCouchRelativePosition	True if the CPI was visible during the acquisition of this line item	True

Water temp (°C)	22		Ratio of speeds - PMMA:water, $R_{PMMA,w}$	1.525	
Speed of sound in water (Marczak 1997), c_w	**1488.4**	ms^{-1}			
Speed of sound in PMMA, c_{PMMA}	**2270**	ms^{-1}	Critical angle, θ_c	41.0	degrees
Speed of sound in soft tissue, c_{st}	**1540**	ms^{-1}			
Origin:			TOF thru PMMA @ θ_i=0	8.55	µs
Centre of object from external face of tank	74	mm	TOF thru water to origin with θ_i=0	36.68	µs
Thickness of PMMA, t	19.4	mm	US measured depth of origin	69.66	mm
Perpendicular water traverse distance, d	54.6	mm	Diff from actual depth	4.34	mm

Marczak (1997) Equation

m_0	1.40E+03
m_1	5.038813
m_2	-5.80E-02
m_3	3.29E-04
m_4	-1.40E-06
m_5	2.79E-09

	US-measured		Set																Diff from set	
seconds from midnight	SI (mm)	AP (mm)	SI (mm)	AP (mm)	Time (s)	Angle to US pos, θ_i (deg)	US path length (mm)	Total TOF (µs)	Refracted angle, θ_t (deg)	Dist thru PMMA @ θ_t (mm)	Vertical offset of exit pt (mm)	TOF thru PMMA @ θ_t (µs)	Remaining TOF in water (µs)	Dist travelled in water (mm)	Vertical offset in water (mm)	Perpendicular depth in water	Total perpendicular depth	Total vertical offset (mm)	Perpendicular depth (mm)	Vertical offset (mm)
59685.0	-0.56	24.43	0.00	30.00	0.00	19.2	74.35	48.28	30.08	22.42	11.24	9.877	38.400	57.152	18.78	53.98	73.38	30.02	-0.62	0.02
59695.7	-0.39	23.17	0.00	28.00	10.66	18.3	73.78	47.91	28.61	22.10	10.58	9.735	38.174	56.816	17.84	53.94	73.34	28.42	-0.66	0.42
59706.3	-0.33	21.24	0.00	26.00	21.32	16.9	73.14	47.49	26.29	21.64	9.58	9.532	37.958	56.496	16.41	54.06	73.46	25.99	-0.54	-0.01
59717.0	-0.32	19.64	0.00	24.00	31.98	15.7	72.68	47.20	24.33	21.29	8.77	9.380	37.816	56.284	15.21	54.19	73.59	23.98	-0.41	-0.02
59727.6	-0.24	18.03	0.00	22.00	42.64	14.5	72.19	46.87	22.40	20.98	7.99	9.243	37.631	56.008	13.99	54.23	73.63	21.99	-0.37	-0.01
59738.3	-0.21	16.23	0.00	20.00	53.30	13.1	71.72	46.57	20.19	20.67	7.13	9.106	37.467	55.765	12.62	54.32	73.72	19.75	-0.28	-0.25
59749.0	-0.14	14.56	0.00	18.00	63.96	11.8	71.30	46.30	18.14	20.42	6.36	8.993	37.305	55.523	11.34	54.35	73.75	17.69	-0.25	-0.31
59759.6	-0.18	12.94	0.00	16.00	74.62	10.5	71.02	46.12	16.14	20.20	5.61	8.897	37.221	55.399	10.09	54.47	73.87	15.71	-0.13	-0.29
59770.3	-0.11	11.20	0.00	14.00	85.28	9.1	70.66	45.89	13.99	19.99	4.84	8.808	37.078	55.186	8.75	54.49	73.89	13.59	-0.11	-0.41
59780.9	-0.07	9.62	0.00	12.00	95.94	7.9	70.39	45.71	12.03	19.84	4.13	8.738	36.970	55.024	7.52	54.51	73.91	11.65	-0.09	-0.35
59791.6	-0.04	7.99	0.00	10.00	106.60	6.5	70.15	45.55	10.01	19.70	3.42	8.678	36.872	54.879	6.25	54.52	73.92	9.68	-0.08	-0.32
59802.3	0.00	6.39	0.00	8.00	117.26	5.2	69.95	45.42	8.01	19.59	2.73	8.630	36.793	54.761	5.00	54.53	73.93	7.73	-0.07	-0.27
59812.9	0.03	4.73	0.00	6.00	127.92	3.9	69.78	45.31	5.93	19.50	2.01	8.592	36.721	54.654	3.70	54.53	73.93	5.72	-0.07	-0.28
59823.6	0.08	3.11	0.00	4.00	138.58	2.6	69.64	45.22	3.90	19.45	1.32	8.566	36.655	54.556	2.44	54.50	73.90	3.76	-0.10	-0.24
59834.2	0.07	1.37	0.00	2.00	149.24	1.1	69.60	45.20	1.72	19.41	0.58	8.550	36.645	54.541	1.08	54.53	73.93	1.66	-0.07	-0.34
59844.9	0.04	-0.25	0.00	0.00	159.90	-0.2	69.62	45.21	-0.31	19.40	-0.11	8.546	36.659	54.561	-0.19	54.56	73.96	-0.30	-0.04	-0.30
59855.6	0.02	-1.96	0.00	-2.00	170.56	-1.6	69.67	45.24	-2.46	19.42	-0.83	8.554	36.683	54.598	-1.54	54.58	73.98	-2.37	-0.02	-0.37
59866.2	0.01	-3.56	0.00	-4.00	181.22	-2.9	69.73	45.28	-4.46	19.46	-1.51	8.572	36.709	54.636	-2.79	54.56	73.96	-4.30	-0.04	-0.30
59876.9	-0.03	-5.10	0.00	-6.00	191.88	-4.2	69.88	45.37	-6.39	19.52	-2.17	8.600	36.775	54.734	-4.00	54.59	73.99	-6.17	-0.01	-0.17
59887.5	-0.04	-6.80	0.00	-8.00	202.54	-5.6	70.02	45.47	-8.51	19.62	-2.90	8.641	36.829	54.815	-5.32	54.56	73.96	-8.22	-0.04	-0.22
59898.2	-0.06	-8.49	0.00	-10.00	213.20	-6.9	70.23	45.60	-10.63	19.74	-3.64	8.695	36.906	54.930	-6.64	54.53	73.93	-10.28	-0.07	-0.28
59908.9	-0.14	-10.03	0.00	-12.00	223.86	-8.2	70.51	45.79	-12.53	19.87	-4.31	8.755	37.032	55.117	-7.84	54.56	73.96	-12.15	-0.04	-0.15
59919.5	-0.20	-11.75	0.00	-14.00	234.52	-9.6	70.84	46.00	-14.66	20.05	-5.07	8.834	37.164	55.313	-9.18	54.55	73.95	-14.25	-0.05	-0.25
59930.2	-0.23	-13.37	0.00	-16.00	245.18	-10.8	71.16	46.21	-16.65	20.25	-5.80	8.920	37.285	55.494	-10.43	54.50	73.90	-16.23	-0.10	-0.23
59940.8	-0.26	-15.08	0.00	-18.00	255.84	-12.2	71.52	46.44	-18.75	20.49	-6.59	9.025	37.416	55.689	-11.74	54.44	73.84	-18.33	-0.16	-0.33
59951.5	-0.34	-16.61	0.00	-20.00	266.50	-13.3	71.94	46.71	-20.62	20.73	-7.30	9.131	37.583	55.937	-12.91	54.43	73.83	-20.21	-0.17	-0.21
59962.2	-0.38	-18.34	0.00	-22.00	277.16	-14.7	72.40	47.01	-22.73	21.03	-8.13	9.266	37.748	56.182	-14.23	54.35	73.75	-22.36	-0.25	-0.36
59972.8	-0.49	-19.89	0.00	-24.00	287.82	-15.8	72.91	47.35	-24.58	21.33	-8.87	9.398	37.948	56.480	-15.40	54.34	73.74	-24.28	-0.26	-0.28
59983.5	-0.62	-21.44	0.00	-26.00	298.48	-17.0	73.48	47.71	-26.42	21.66	-9.64	9.543	38.168	56.808	-16.57	54.34	73.74	-26.21	-0.26	-0.21
59994.1	-0.71	-22.91	0.00	-28.00	309.14	-18.0	74.01	48.06	-28.18	22.01	-10.39	9.695	38.361	57.094	-17.68	54.29	73.69	-28.07	-0.31	-0.07
60004.8	-0.81	-24.62	0.00	-30.00	319.80	-19.3	74.64	48.47	-30.20	22.45	-11.29	9.888	38.582	57.424	-18.94	54.21	73.61	-30.23	-0.39	-0.23

Figure 17: Example correction calculations for anterior-posterior series

4.3.1 Left-Right axis

Positional data were collected along the left-right (lateral) axis every 2 mm between -30 mm and +30 mm. As this was a lateral scan there were no programmed movements in the vertical and longitudinal directions; therefore, these data would be expected to remain zero if the experimental setup and correction were perfect. Figure 18 shows the difference after correction of the lateral and longitudinal positions from the set values. The corrected longitudinal values have been included in Figure 18 as they were also output from the 2D lateral correction calculation since it took 2D data as input. For both the lateral and vertical series discussed below, the longitudinal components were used as the secondary axis, and for the longitudinal correction the vertical components were used. In each case the secondary axis was chosen based on which of the remaining two axes exhibited a greater range of motion and would therefore better represent what was happening physically during the data acquisition.

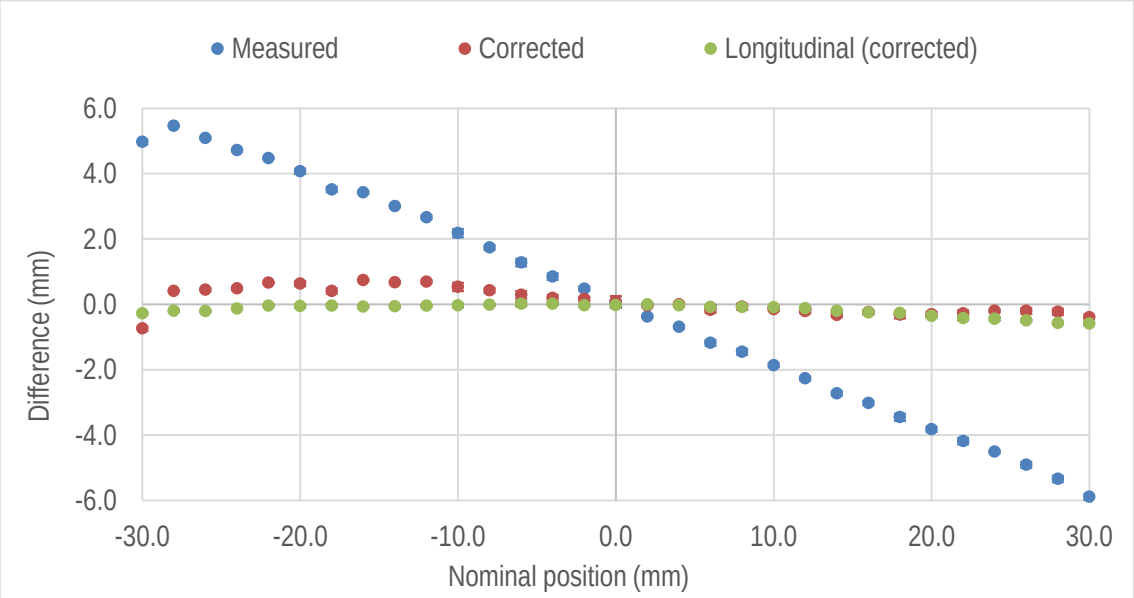

Figure 18: Mean lateral difference from nominal before and after correction, plus corrected longitudinal differences (± 1 SD)

Aside from the initial data point at -30 mm, the corrected lateral differences (orange) still appear to exhibit a downward trend from left to right of a little more than 1 mm over the full 60 mm range of motion. In addition to this these data appear to be more variable than the longitudinal difference values. If the apparent trend is real, then this could be caused by a slight rotation in either the

probe or Clarity coordinate system relative to the tank axis (see next section for more detail). Furthermore, the asymmetry of the curvature, with approximately 0.6 mm offset at the negative end compared to approximately 0.3 mm at the positive end, suggests there may have been a slight translation in addition to a possible rotation in the orientation of the probe.

Longitudinal differences in Figure 18 exhibit a curvature away from the front (inferior wall) of the tank at the peripheries of up to 0.6 mm. While this suggests a slight error in the correction algorithm, it represents less than 1 percent of the total distance from the source to the peripheral point and is likely a result of the simplicity of the model including its assumptions enumerated previously.

4.3.2 Superior-Inferior axis

Positional data were collected along the superior-inferior axis every 2 mm starting at 30 mm superior to the isocentre. Unfortunately, a mistake in the initial positioning of the tank did not leave sufficient room to measure all the way to 30 mm inferior to the isocentre, so data were only collected between –30 mm and +10 mm. Figure 19 shows that after correction all positions in the superior-inferior direction are within ±0.15 mm of the nominal position.

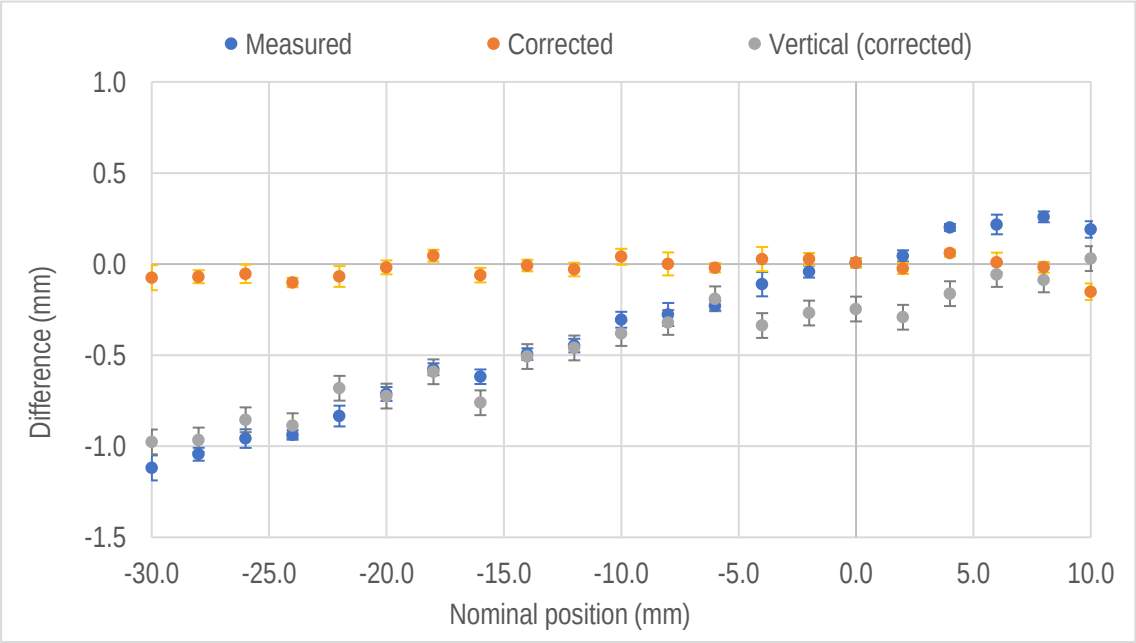

Figure 19: Mean longitudinal (SI) differences from nominal before and after correction, and vertical offset after correction (± 1 SD)

If the central axis of the Clarity probe and the longitudinal axis of the Clarity coordinate system had been aligned exactly to the longitudinal axis of the tank there would be no angulations in the collection geometry for this scan, and the algorithm would only be correcting for time-of-flight in this direction, not refraction. In practice this is not the case as it was difficult to precisely align the Clarity probe with the linac coordinate system. Furthermore, the nominal positions are relative to the coordinate system of the scanning tank mechanism, which was aligned as carefully as possible to the linac coordinate system as represented by the room lasers.

On the other hand, the Clarity-reported positions are defined in the Clarity coordinate system, which is relative to the position and orientation of the infrared cameras and defined by a calibration process called the "Room Setup"; therefore, a misalignment between these coordinate systems through an erroneous calibration could explain the slope in the vertical offset data in Figure 19. Analysis suggested a potential tilt in the Clarity coordinate system relative to the tank scanning mechanism of approximately 1.4 degrees. The Clarity Room Setup calibration procedure was redone following this study, which appeared to improve the agreement between the two coordinate systems in the next study.

4.3.3 Anterior-Posterior axis

Positional data were collected along the vertical axis every 2 mm between -30 mm and +30 mm. Figure 20 shows the uncorrected and corrected positions of the vertical profile, and the corrected longitudinal positions, and looks very similar to Figure 18 for the lateral profile.

Once again, the geometric error in the positions in the direction of motion before correction are sloping linearly across the full range, however after correction this slope is all but eliminated. The perpendicular depth differences also exhibit similar curvature to those in Figure 18 above for the lateral profile.

4.3.4 Checking the model calibration

The slopes in the lateral and vertical offsets, and the curvature in the longitudinal offsets in Figure 18 and Figure 20 were all sensitive to the geometric and physical parameters of the model. The speed of sound in water is well known and the total distance to the analogue from the inferior surface of the tank was physically measured to within ±1 mm. The two remaining key parameters

were also the least well defined: the thickness of the tank wall and the speed of sound in PMMA. In a perfect model it would be possible to tune these parameters to eliminate the slopes and curvatures in the figures above. Unfortunately, there was an inverse relationship between these: for example, considering Figure 18, tuning the model to reduce the slope in the corrected lateral positional differences increased the curvature in the corrected longitudinal positions, and *vice versa*.

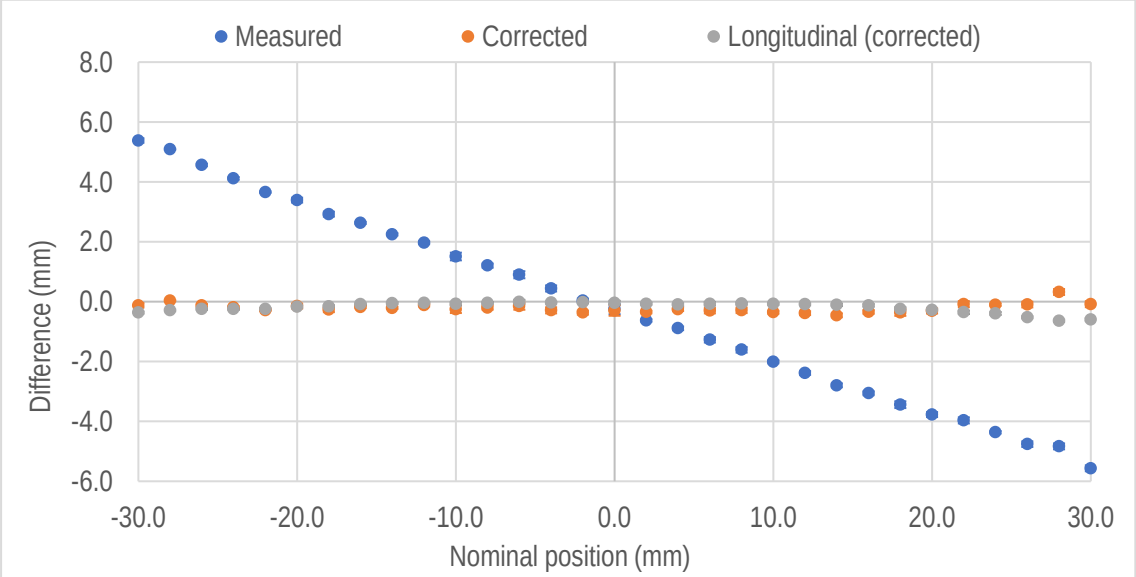

Figure 20: Mean vertical (AP) differences from nominal before and after correction, and longitudinal offset after correction (± 1 SD)

As observed in section 3.4.4 above, the scale of the distortion at the peripheries in the lateral direction was roughly equal to that in the vertical direction. Therefore, in order to assess the effect of these two parameters on the model output, the longitudinal components of the geometric error at the four extreme points in the lateral and vertical profiles were averaged, as were the four extreme lateral and vertical components, giving a mean longitudinal offset of -0.72 mm and a mean lateral/vertical offset of 24.55 mm. This single uncorrected point representing the four most extreme points in the axes of the transverse plane was then used in the 2-dimensional model to assess the effect of independently changing the speed of sound in PMMA and the thickness of the tank wall.

The offset results in the longitudinal 'profile' are almost completely insensitive to these two parameters since the first step in the algorithm is to calculate the time-of-flight to the Clarity origin

and set this as the Clarity-measured starting position. For this reason, the effect of these parameters on only the lateral and vertical profiles will be discussed.

I. Speed of sound in PMMA

Figure 21 shows the dependence of the 2-dimensional model on the speed of sound in the tank wall. The refraction correction was calculated for the point (-0.72, 24.55) for a range of different values for the speed of sound in the PMMA. The sum of the squares (grey) of the resulting components at each point (blue and orange) was plotted and a 5th-order polynomial was fitted. The sum of squares was used rather than the physically representative square-root of the sum of squares as it yielded a parabola-like curve that was easier to fit to while maintaining the same minimum turning point. The first order derivative function was determined from the polynomial fit parameters and the point where the derivative was equal to zero was found.

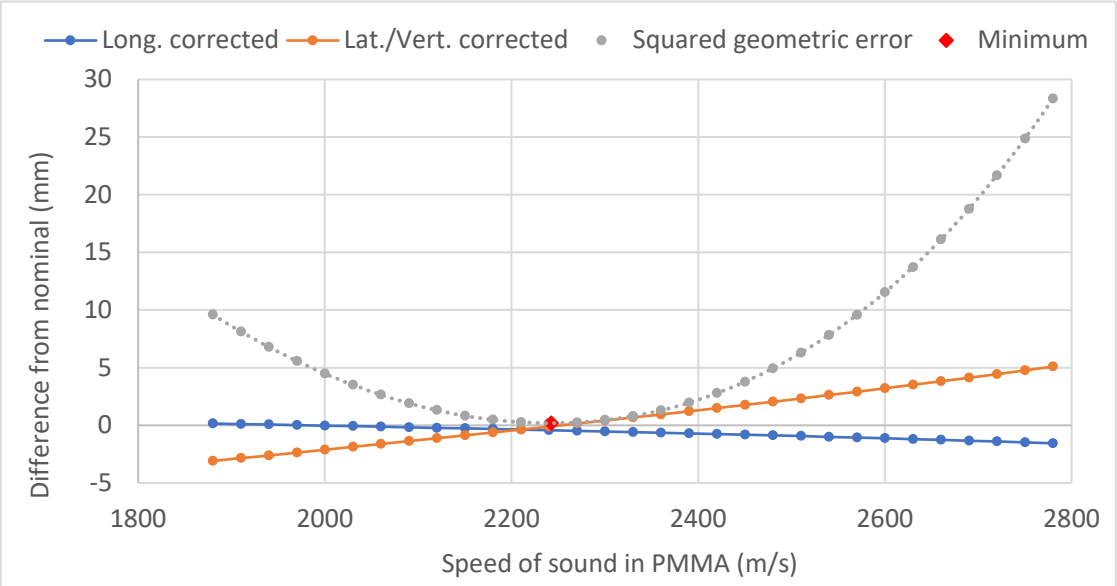

Figure 21: Effect of speed of sound in PMMA on total geometric error

While maintaining a tank wall thickness of 19.4 mm a minimum total geometric error of 0.44 mm was found for a speed of sound in the PMMA of 2242.3 m/s. This is very close to the value of 2270 m/s used throughout this work which, using the same analysis, produced a total geometric error of 0.50 mm. Note also from Figure 21 that the published value for the speed of sound in PMMA of 2750 m/s discussed in section 4.2.1 corresponds to a geometric error of approximately $\sqrt{25} = 5$ mm.

The optimal speed of sound in PMMA that minimised the 2D offset was found using two different methods: first an iterative calculation using data processing software, then a manual approach using interpolation of multiple calculated points. The average of the two results is v_t = 2271 m/s; therefore, the elastic wave velocity reported by Christman *et al*. of 2270 m/s, will be used for the remainder of the work.

II. Tank wall thickness

The analysis described above was repeated for the tank wall thickness while maintaining a speed of sound in PMMA of 2270 m/s. The minimum was again 0.44 mm and was found at a thickness of 18.76 mm (Figure 22). The thickness measured along the top edge of the tank wall of 19.4 mm yielded a displacement of 0.5 mm.

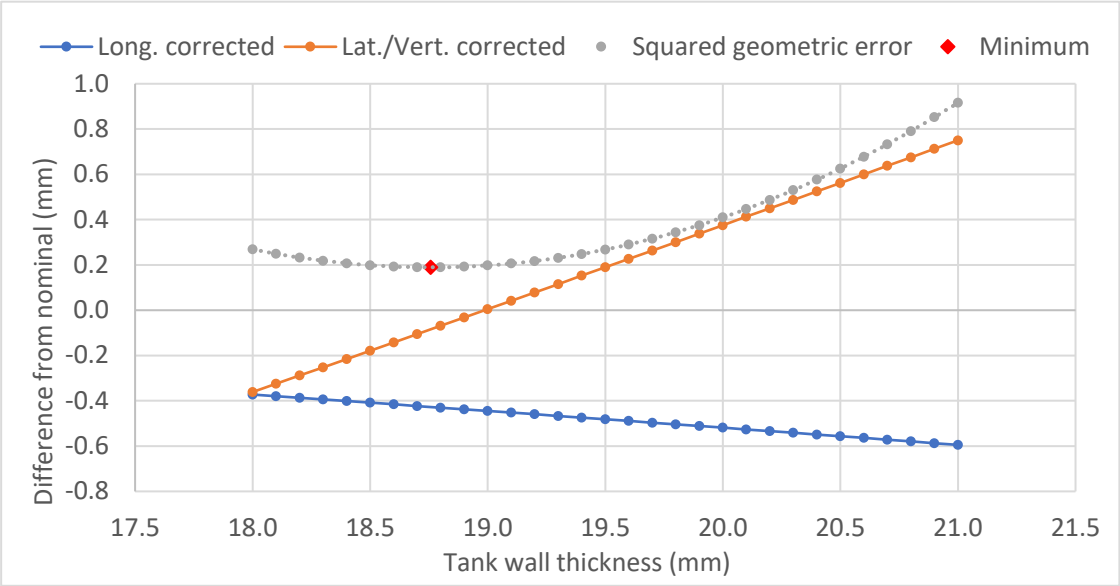

Figure 22: Effect of tank wall thickness on total geometric error

4.4 Discussion

A 2D refraction correction algorithm was developed and successfully tested on data points collected along the three cardinal axes. After correction, all data points were within 1 mm of the nominal positions programmed into the scanning mechanism of the water tank, with the exception of one outlier at one extremity of the lateral data. As mentioned above, since this was a 2D algorithm positional data from a second axis was also used as input into the correction calculation. This was not essential given the small offsets in the other directions, however given the apparent slight

misalignment of the Clarity and scanning tank coordinate systems found earlier it did yield some improvement in the results. The following observations will assist in the development of the experiment moving into Chapter 5.

I. Effect of sweep direction on lateral position

The variability in the lateral positions observed in Figure 18 may be the result of a phenomenon only observed during the next study, in which the reported lateral position of the tracked volume can vary by up to 1 mm depending on the direction of sweep of the ultrasound transducer (Figure 23). This phenomenon was later confirmed via communication from the manufacturer.

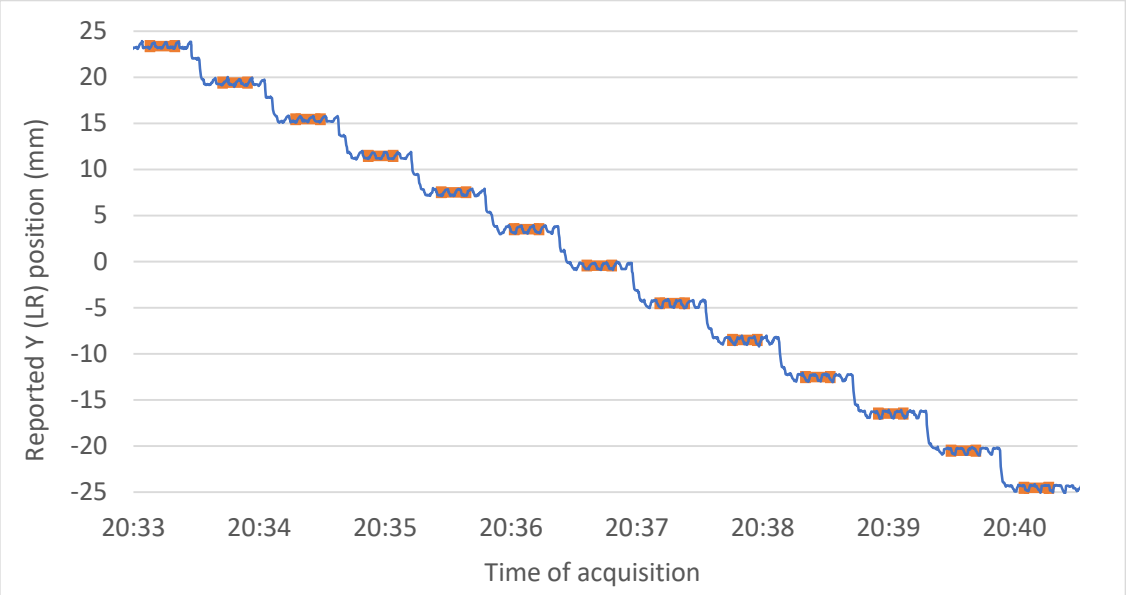

Figure 23: Example of lateral 'profile' exhibiting periodic behaviour indicative of a dependence on sweep direction

The frequency of the 1 mm-amplitude oscillations evident on top of the 30 second stepped pattern in Figure 23 is 2.5 seconds, corresponding to the sweep frequency of the Clarity probe transducer. The orange bars indicate the 10 second periods used in Chapter 5 to find the average position at that location, however this study used a 2 second period, which could potentially have fit within either a peak or a trough of this oscillation. Note also that as the analogue was stepped from left to right the peaks of the 2.5 second oscillation widened, and the troughs became narrower. This is because the changing lateral offset of the analogue changes the point in time within each sweep when the new position is acquired.

Unfortunately, using only a 2 second period for this study meant that the average lateral positions could have varied by as much as 1 mm depending on where the 2 second periods fell across the acquisition. Therefore, this directional dependence could have contributed to both the slope in the data and the more variable appearance of these data compared to the longitudinal data in Figure 19. The most likely explanation is that the slope is primarily due to a rotation or translation of the probe and that the directional dependence made the data more inconsistent.

Results of image quality testing reported in the Appendix suggest that the spatial resolution in the reconstructed direction is quite poor compared to the other two axes, yielding only 3-4 mm in that test. This will further confound the lateral positioning accuracy and may somehow contribute to the directional dependence.

II. Tracking volume limits

While not obviously reflected in the data reported in this chapter, it was observed at the time of acquisition that movements outside of ±30 mm in the lateral and vertical directions near the front of the tank tended to result in the system losing track of the analogue. Tracking was typically only regained once the analogue was moved back to near the normalisation point. One might expect this to be worse nearer to the inferior wall of the tank where the refraction would exaggerate the distortion of the analogue and the width of the volume swept out by the imaging plane would be narrower. Therefore, tracking is restricted in all directions except for the superior direction – whether by physical proximity to the tank wall, limited scan angle or distortion of the analogue. Considering the male anatomy, it was decided that tracking beyond approximately 120 mm superiorly from the probe would not be clinically relevant and so the 3-dimensional algorithm in Chapter 5 would be assessed using points throughout a roughly 60 x 60 x 60 mm^3 volume centred on the Clarity origin.

III. Improving position statistics

In addition to the problems described above from averaging over only 2 seconds of positional data in the presence of a dependence on sweep direction, the number of data points within the 2 second window as a result of the frequency of the software reconstructing the volume can vary considerably as well. The average number of points within each window for all the reported positions was 8, with a minimum of only 3. Furthermore, the reconstruction update frequency was found to be

periodic, varying between as much as 1 and 200 updates per second (Figure 24). This was initially assumed to be somehow related to the sweeping mechanism, however the period is slightly greater at 2.95 seconds, so it is unclear what is causing this. Due to these findings it was determined that, for testing the 3D algorithm in Chapter 5, the hold time at each position would be expanded to 30 seconds and a 10 second window used in the middle of the pause to find the average position. To compensate for the additional acquisition time needed, the distance between data points for future work will be expanded to 5 mm.

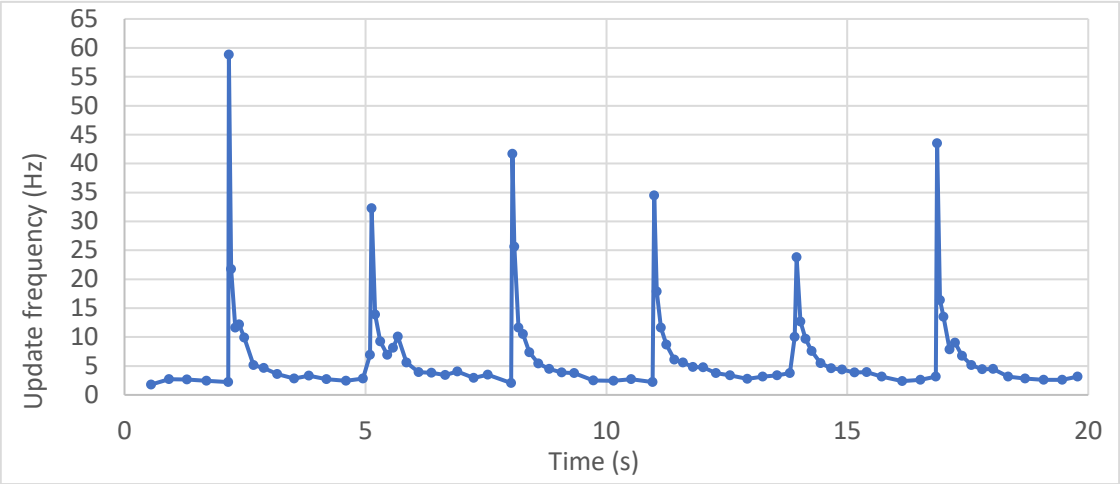

Figure 24: Positional data update frequency variation with time

I. Coordinate system misalignment

One potential cause of the slope in the vertical positions seen in the assessment of the longitudinal data above (Figure 19) was a miscalibration of the Clarity coordinate system used to report the target positions. The Clarity system comes with a dedicated phantom that includes external markings for aligning to the room lasers and infrared reflectors that enable the Clarity system to accurately calculate the position and orientation of the phantom. The Room Setup calibration procedure uses the position and orientation of the phantom to define both the isocentre and the orientation of the Clarity coordinate system relative to the position and orientation of the stereoscopic cameras fixed to the ceiling of the simulation or treatment room.

In this case it was discovered subsequent to the work reported herein that the phantom could have been more accurately aligned to the room lasers, needing to be propped up very slightly at the superior end (three thicknesses of paper towel was sufficient). The Room Setup was repeated

prior to the data acquisition for Chapter 5, reducing the misalignment in the longitudinal axis very slightly. It was not deemed necessary to repeat this work as the effect on the results was minimal.

II. Rotational symmetry of refraction distortion

In Chapter 3 it was observed that a similar degree of distortion was apparent in both the lateral and vertical directions. This has been confirmed by the similar lateral and vertical offset behaviour in Figure 18 and Figure 20. The uncorrected differences show a linear trend in both figures with similar gradients. While difficult to explain given the very different internal geometry of the probe in each direction, with its sweeping 2D transducer, it supports the further development of the simple bi-layer refraction correction algorithm into 3D space.

4.5 Summary

The purpose of this study was to develop a two-dimensional (2D) correction algorithm that could account for refraction in the PMMA tank wall and phantom water, and then to compare corrected Clarity positional measurements with programmed displacements along each axis as reported by the Clarity system. The algorithm was developed in three phases: derivation, calibration and testing.

The calibrated 2D algorithm yielded sub-millimetre differences from nominal positions for measured data along each of the cartesian axes. Chapter 5 will extend the 2D algorithm developed here to 3 dimensions and use it to correct the positions of points measured throughout a clinically useful volume.

Chapter 5: Position correction algorithm for refraction in 3-dimensions

5.1 Introduction

In Chapter 4 a 2-dimensional refraction correction algorithm was developed and tested for Clarity positional data in the sagittal and coronal planes that include the Clarity isocentre. In this chapter the 2D vector algorithm will be derived and extended to the third dimension, enabling the correction of any measured position within the ultrasound imaging volume using a rotation matrix. This algorithm will then be tested on data collected throughout a clinically relevant volume and compared to the results of work by other investigators.

5.2 Method

The reverse 2D correction will be rederived in vector form to take as input the vector representing the position of the prostate analogue as perceived by the ultrasound (see section 5.2.1 below). The angle that the position vector makes with the vector normal to the surface of the tank will be found via Eq. (17). The refraction can initially be treated as though occurring in the coronal plane that includes the Clarity origin and corrected as per Chapter 4. The angle θ between the component of the position vector in the transverse plane and the positive left-right axis (Figure 25) can then be found using Eq. (23). It will be shown that a 3D rotation matrix applied to a 3D reference frame containing the coronal plane will bring the corrected point near to its nominal off-axis position (Figure 25).

5.2.1 Extending the 2D algorithm to 3D

The assumptions made for the 3D algorithm are the same as those made for the 2D algorithm in Chapter 4. The Law of Reflection states that the normal to the surface lies in the same plane as the incident and reflected rays called the plane-of-incidence. The 3D algorithm relies on the second part of the Law of Refraction which states that the incident, reflected, and refracted rays all lie in the same plane [66]. The Law of Refraction implies that the refracted ray also lies in the plane-of-incidence, and that this plane can be defined by just the two vectors representing the incident ray and the boundary surface. Therefore, since all refraction occurs in a plane a 2D algorithm can be used to correct for any refraction that occurs between two layers of different materials (i.e. bi-layer).

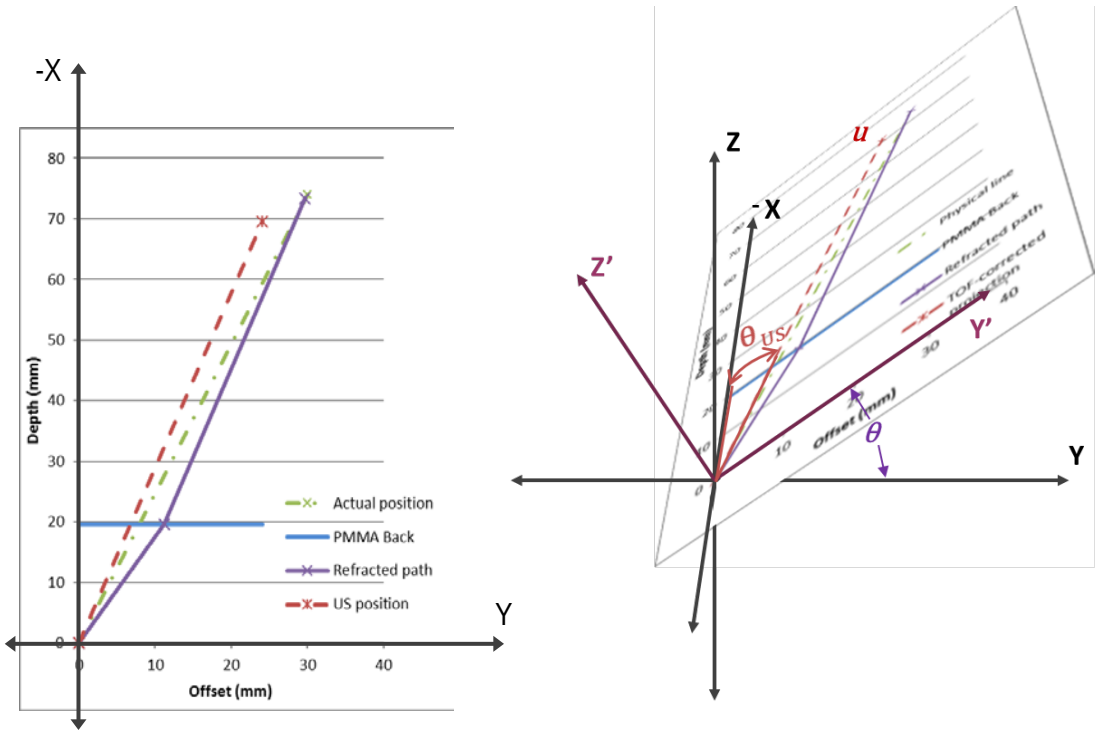

Figure 25: Rotation of the refraction plane about the X-axis.

In the coordinate system of the Clarity Autoscan the X-axis corresponds to the superior-inferior direction, the Y-axis to the left-right direction and the Z-axis to the anterior-posterior (AP) direction. In Chapter 4 the prostate analogue was initially centred on the isocentre as per the room lasers and the acquisition software was zeroed to this normalisation point. The distance, d, to the external (inferior) surface of the tank and the thickness, t, of the PMMA tank wall were both measured. The water component of the distance to the isocentre was $d_w = d - t$. Using the known speeds of sound in water, c_w, PMMA, c_{PMMA}, and soft tissue, c_{st}, the depth of the normalisation point as measured by the ultrasound, d_{US}, is calculated via:

$$d_{US} = c_{st} \times \left(tof_{PMMA,iso} + tof_{water,iso}\right) \tag{13}$$

where $tof_{PMMA,iso} = d_{PMMA}/c_{PMMA}$ and $tof_{water,iso} = d_w/c_w$ are the time-of-flight (TOF) to the isocentre of the ultrasound signal traversing the PMMA and water respectively. Note that for simplicity time-of-flight will be discussed throughout as though it were only in one direction, so all references to time-of-flight will be either outbound or inbound, not both.

The TOF-corrected depth of the Clarity origin, d_{US}, is used to translate the origin of the coordinate system to the front surface of the tank, at the point of contact with the probe using the TOF-corrected translation vector,

$$\mathbf{t}_{\mathrm{c}} = \begin{bmatrix} -d_{US} \\ 0 \\ 0 \end{bmatrix}. \tag{14}$$

For a position vector, $\mathbf{v}$, of a point of interest as reported by the Clarity system, the corresponding position in the translated coordinate system with its origin at the point of contact between the Autoscan probe and the tank wall is given by

$$\mathbf{u} = \mathbf{v} + \mathbf{t}_{\mathrm{c}}. \tag{15}$$

The magnitude, $|\mathbf{u}|$, can be used to determine the total flight time to $\mathbf{u}$:

$$tof_{total} = |\mathbf{u}|/c_{st}\,. \tag{16}$$

The unit vector pointing in the direction of $\mathbf{u}$ is $\hat{\mathbf{u}} = \mathbf{u}/|\mathbf{u}|$ and the unit vector normal to the inferior exterior surface of the tank is $\hat{\mathbf{n}} = \begin{bmatrix} -1 \\ 0 \\ 0 \end{bmatrix}$.

These can be used to calculate the angle that the Clarity-reported position vector in the translated reference frame makes with the normal to the surface of the tank:

$$\theta_{US} = cos^{-1}(\hat{\mathbf{n}} \cdot \hat{\mathbf{u}}). \tag{17}$$

As discussed above the refraction in the PMMA and water occurs in a plane that includes $\hat{\mathbf{u}}$ and $\hat{\mathbf{n}}$. The refraction-corrected position vector, $\mathbf{p}$, will therefore be found by first correcting in two dimensions using θ_{US} as the angle of incidence and then rotating the plane of refraction by the angle made between the plane of refraction and the Y-axis, θ, before translating back to the original coordinate system.

Based on the assumption from Chapter 4 that the angle of the ray perceived by the ultrasound unit is equal to the angle of the ray path in the tank water, we can use θ_{US} as the angle of incidence to find the refracted angle in PMMA, θ_{PMMA}, using Snell's law:

$$\theta_{PMMA} = sin^{-1}\left(\frac{c_{PMMA}}{c_w} \times sin\,\theta_{US}\right). \tag{18}$$

Define the path length to the point of interest through the PMMA as $l_{PMMA} = t/\cos\theta_{PMMA}$, and the time taken to traverse the PMMA in one direction as $tof_{PMMA} = l_{PMMA}/c_{PMMA}$. The time-of-flight in water on the way to the point of interest is therefore

$$tof_w = tof_{total} - tof_{PMMA}. \tag{19}$$

Now that the time-of-flight in water is known, the path length in water can be calculated via $l_w = c_w/tof_w$. Since the original X-axis lies within the plane of refraction, let X and Y' denote the two axes in the plane of refraction and let Z' denote a third axis orthogonal to both X and Y'. With the path lengths calculated in PMMA and water in the plane of refraction, the components of each path in the X, Y' and Z' axes can be calculated and summed to give the final position vector, $\mathbf{s}$, in the XY'Z' space:

$$\mathbf{s} = \begin{bmatrix} (u_x/|u_x|) \times (l_{PMMA}\,cos\,\theta_{PMMA} + l_w\,cos\,\theta_{US}) \\ (u_y/|u_y|) \times (l_{PMMA}\,sin\,\theta_{PMMA} + l_w\,sin\,\theta_{US}) \\ 0 \end{bmatrix}. \tag{20}$$

The 3-dimensional refraction-corrected position vector, $\mathbf{r}$, in the translated coordinate system can now be found by rotating the XY'Z' coordinate system about the X-axis by the angle, θ, made between the Y and Y' axes using the rotation matrix, $\mathbf{R}(\theta)$. That is,

$$\mathbf{r} = \mathbf{R}(\theta)\mathbf{s} \tag{21}$$

where

$$\mathbf{R}(\theta) = \begin{bmatrix} 1 & 0 & 0 \\ 0 & \cos\theta & \sin\theta \\ 0 & -\sin\theta & \cos\theta \end{bmatrix} \tag{22}$$

and

$$\theta = -\tan^{-1}(u_z/u_y). \tag{23}$$

The 3-dimensional refraction-corrected position vector, $\mathbf{p}$, in the original Clarity coordinate system can now be found by applying the un-corrected translation vector, $\mathbf{t} = [d \quad 0 \quad 0]^T$:

$$\mathbf{p} = \mathbf{r} + \mathbf{t}. \tag{24}$$

5.2.2 Experimental setup

The setup was almost identical to that reported in Chapter 4, however, this time the normalisation point was positioned more superiorly within the tank so that it was physically possible to move the prostate analogue more than 30 mm toward the front of the tank (i.e. toward the probe) from the normalisation point (Clarity origin). This allowed positional data to be acquired at least 30 mm in every direction from the normalisation point.

The approach taken to setup the initial longitudinal position was slightly different than was used previously. Since the origin of the tank coordinate system can be normalised to practically any point within the tank, the scanner control software enables the user to set limits on the motion of the mechanism in each direction so that the prostate analogue does not collide with the walls of the tank. The first step was to move the analogue as near as possible to the interior surface of the inferior wall of the tank and to set this point as the limit of motion. The analogue was then moved superiorly 30 mm and the normalisation point defined in the tank control software. The total distance from the exterior surface of the inferior wall to the normalisation point was 96 mm, compared to 74 mm used in Chapter 4.

5.2.3 Data acquisition

For this study the data were acquired for a 30 second interval at each point. A total of 28 'profiles' were acquired, in the longitudinal, lateral and two diagonal directions. These four profiles were each acquired in 7 horizontal planes, vertically spaced 10 mm apart. The scanning tank was programmed to acquire positional data at 5 mm intervals along each profile spanning 30 mm either side of the normalisation point. The intent was to acquire data throughout a 60 x 60 x 60 mm^3 region centred on the normalisation point; however, the software controlling the scanning system rescaled each profile based upon its depth relative to the isocentre, that is, the normalisation point, and corresponding distance to the target of the linac (1 m from the target to the isocentre). This resulted in a data range of -29.1 mm to +29.1 mm in the uppermost plane and -30.9 mm to +30.9 mm in the lowermost plane. While this vertical scaling can be a useful feature when measuring dose profiles in a radiation beam it was a nuisance for the purposes of this work.

The scanning system was programmed such that the 7 lateral profiles were acquired sequentially in alternating directions to allow the Clarity system to maintain tracking when moving between

profiles (Figure 26). This was then followed by the 7 longitudinal profiles, then the 7 diagonal profiles in one direction, followed by 7 of each of the diagonal profiles. The resulting data files would be processed individually by a MATLAB application discussed below.

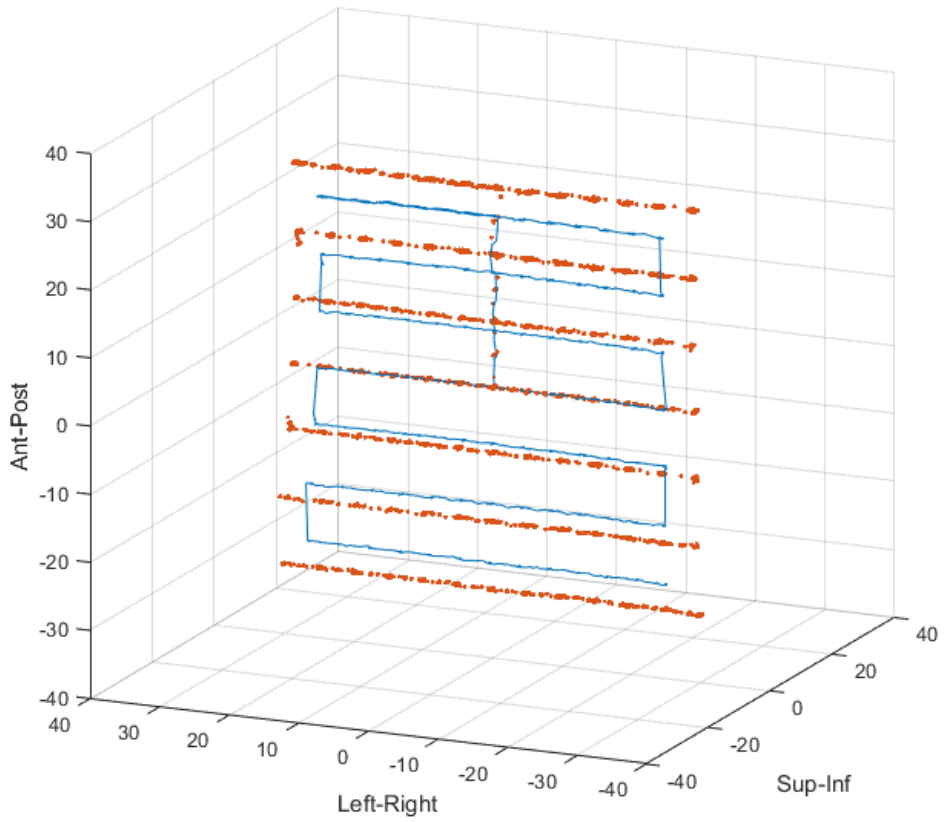

Figure 26: Acquisition of lateral profiles (blue) with corrected values (orange)

5.2.4 Implementation in MATLAB

A MATLAB application was developed to read in the output files generated by the Clarity software and calculate the refraction-corrected position vectors for each data point (Figure 27). These output files hold the date and time of acquisition for each data point along with a confidence level parameter and two sets of X-Y-Z coordinates for each point – one set ("Xshift, Yshift, Zshift") indicating the absolute prostate position in the Clarity coordinate system and the other set ("CouchRelativeX, CouchRelativeY, CouchRelativeZ") relative to the normalisation point and including any real-time couch shifts based on the Couch Position Indicator (CPI). The application

also takes as input the speeds of sound in water and PMMA, the thickness of the PMMA and the distance from the front face of the tank to centre of the prostate analogue.

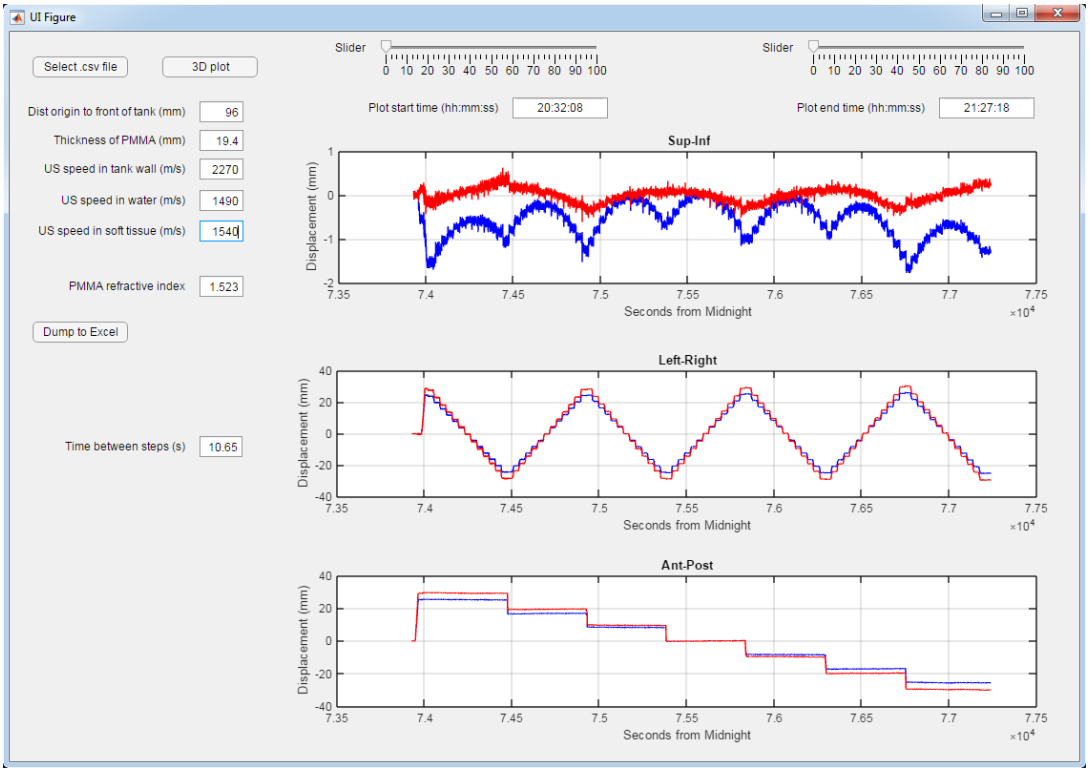

Figure 27: MATLAB application for calculating and displaying raw (blue) and refraction-corrected (red) Clarity position data

On loading the data file, the uncorrected positions are represented graphically in three plots, one for each of the Clarity X-, Y-, and Z-axes, and the refraction-corrected positions are automatically calculated and displayed in the same axes. Modification of any of the key parameters automatically triggers a recalculation of the corrected data. MATLAB is easily able to handle the simple matrix operations such as addition and subtraction of translation vectors. Each file contains thousands of data points, and each point requires a unique rotation matrix to be calculated. On a desktop PC with 8.0 GB of RAM, 4 processors and 64-bit operating system, the whole operation takes approximately 3 seconds, including the refresh of the graphical user interface (GUI).

5.2.5 Additional data processing

The MATLAB application applied the 3D refraction correction to every data point acquired throughout all 28 profiles. To find the average position within each 30 second hold interval as

described in Chapter 4, the corrected data were exported to a data visualisation program for ease of display and manual manipulation. The data from each of the files dumped from the MATLAB application were plotted on a curve with sufficient resolution to easily make out the individual 'steps' produced by the movement of the analogue. As the time taken for the analogue to move between positions was consistent, it was possible to determine an interval between the approximate mid-points of the data at each position. A relatively narrow window was chosen of 5 seconds either side if the mid-point able to exclude erroneous data resulting from the lag due to the finite sweep time of the transducer. The average values were plotted on the same curve and both plots were visually inspected to ensure that the newly created average values occupied the middle of each step. Error bars were also used to visually confirm that the range used for the average calculation sat well within the flat portion of each step.

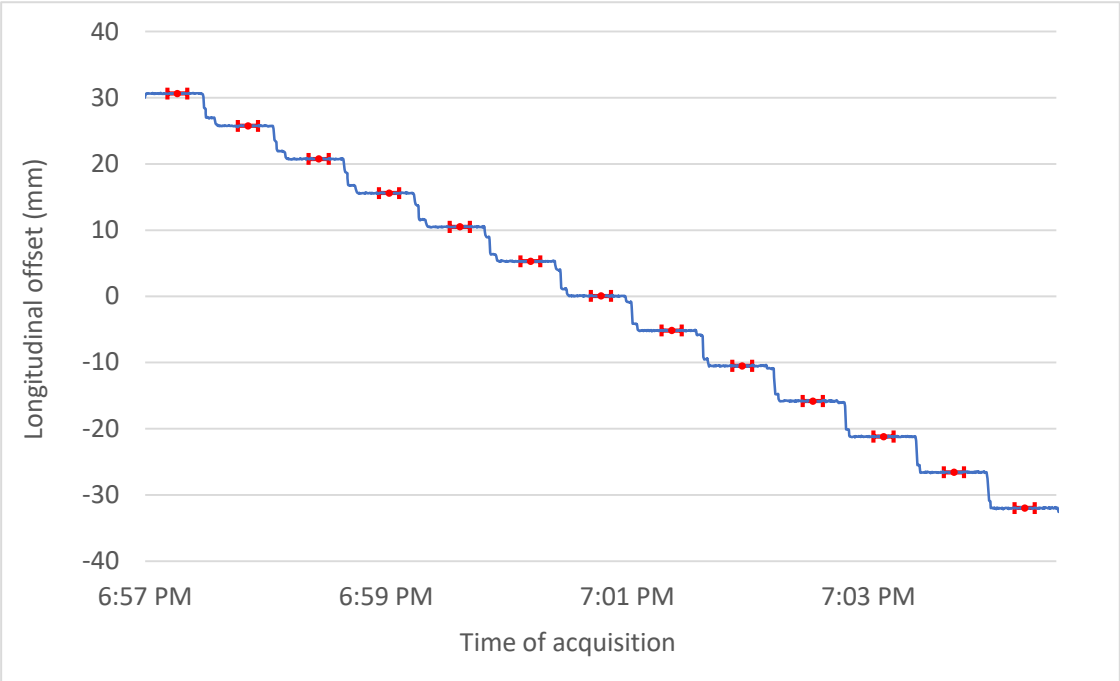

Figure 28: Profile example showing data windows used for mean position calculation

The average values at each position for both the corrected and uncorrected data were used to determine the geometric offset from the nominal positions as programmed into the control software of the scanning tank.

5.3 Results

Over 58,700 positional measurements were acquired throughout the programmed volume with 364 raw positions calculated using the 10 second windows. Each window contained on average approximately 50 data points, with a minimum of 39. This was a significant improvement on the minimum of 3 for the 2 second averaging window used in Chapter 4. The mean (±SD) error of the raw measurements from the nominal positions was 4.0±1.8 mm with a maximum of 9.3 mm. The bi-layer 3D refraction correction algorithm reduced this to 1.0±0.5 mm with a maximum of 3.4 mm. Figure 29 shows a vector plot of the corrected and uncorrected measurements from the nominal positions. Note that the volume that was sampled was virtually a cube, however the AP axis in Figure 29 has been compressed to aid visibility of all vectors.

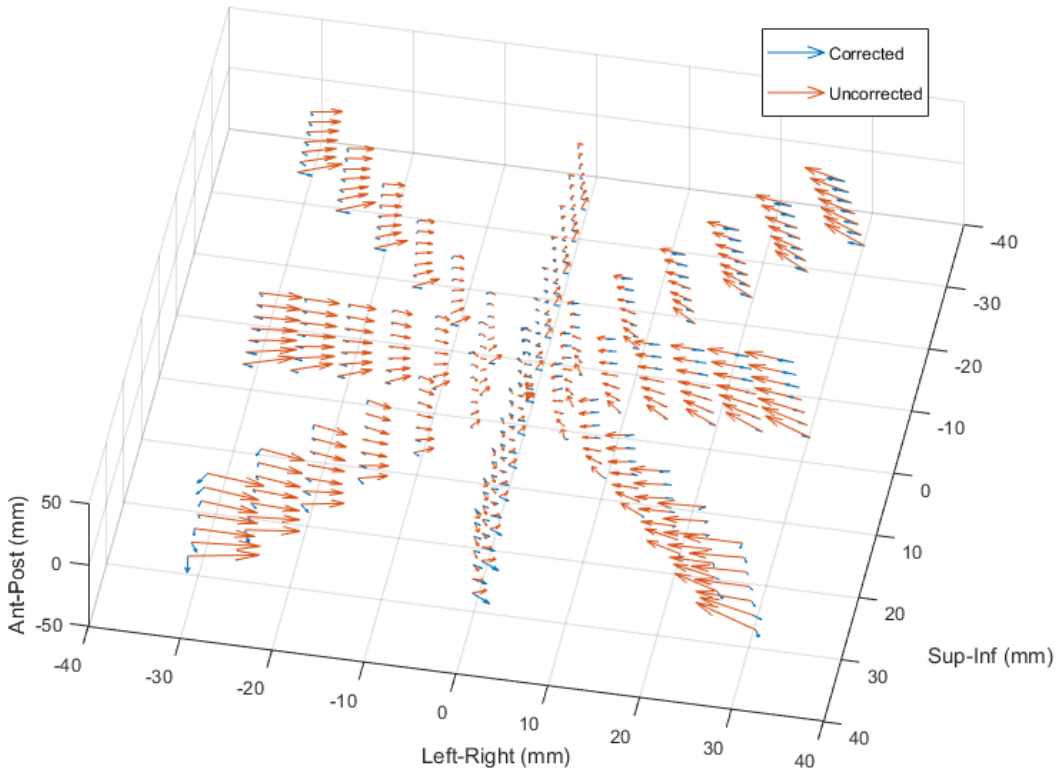

Figure 29: Vector plot showing difference from nominal before and after refraction correction

5.4 Discussion

By analysing the available data more deeply it may be possible to isolate factors contributing to the success or failure of the algorithm and thereby identify ways in which the process could be improved in the future. Therefore, we will attempt to determine if there was any correlation between the magnitudes of the geometric errors at the nominal positions and the distance to the Clarity origin, the distance to the Clarity probe, the angle made between the plane of refraction and the coronal plane, and the magnitude of the Clarity-reported quality factor.

5.4.1 Correlation of geometric error magnitude with distance from Clarity origin

The scanning mechanism of the water tank was programmed to move throughout a roughly cube-shaped volume extending ±30 mm in each of the cardinal directions from the Clarity origin, or normalisation point. This resulted in diagonal movements as much as 53 mm from the Clarity origin, in the four lowermost corners of the volume. Figure 30 shows a clear correlation between the distance of the nominal positions from the Clarity origin and the magnitude of the geometric errors at each position, both before and after correction. It is noteworthy that the geometric errors at all nominal positions within 30 mm of the Clarity origin are less than 2 mm after correction.

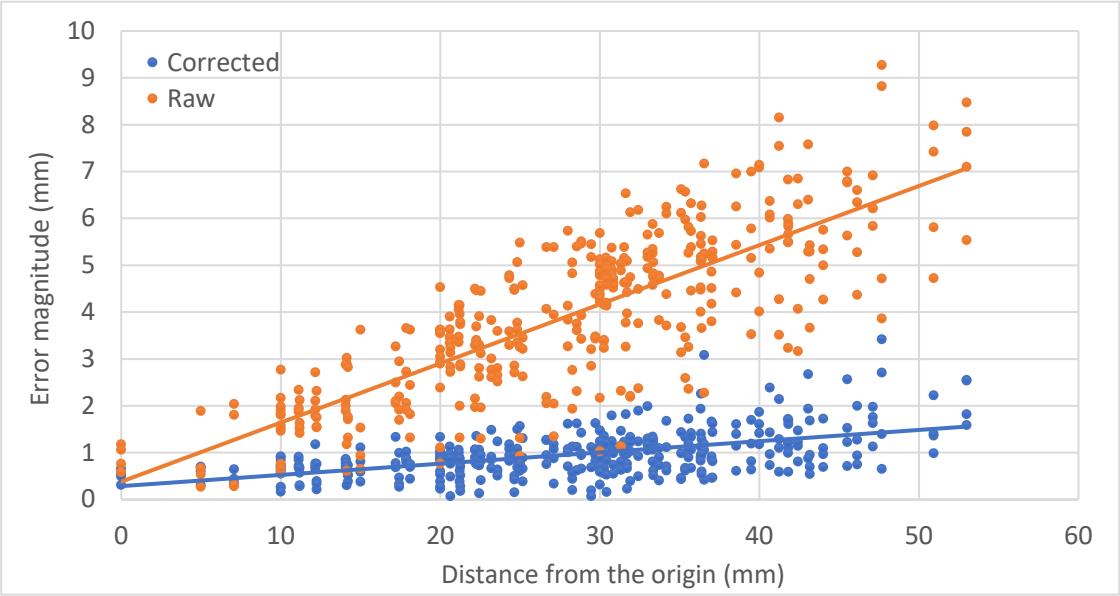

Figure 30: Error magnitude as a function of distance of nominal position from the Clarity origin

The correlation is strong both before and after correction, with Pearson correlation coefficients of R = 0.851 and R = 0.597 respectively. If the scale of the correction was a linear function of initial

distance from the Clarity origin the correlation coefficient would remain unchanged while the slope of the curve reduced. Therefore, since the correlation coefficient was reduced by refraction correction the correction had a disproportionate effect at different distances.

Figure 31 shows the cumulative distributions of geometric error after correction as a function of radial distance from the Clarity origin of all points with tracking confidence ≥ 0.5. The slope of the green line is indicative of the number of new points being added to the statistics with increasing radius. For example, the region above radius = 50 mm adding only the eight corner points of the measured volume.

Figure 32 compares the ratio of the corrected to the uncorrected geometric error magnitudes against the uncorrected geometric error magnitudes. For almost all positions with raw geometric error magnitude greater than 1.2 mm the refraction correction reduced the magnitude of the error by greater than 50%, with a subtle trend toward greater relative reduction with increasing raw error magnitude. However, for those positions with a raw geometric error magnitude of less than 1.2 mm, the relative effect of the refraction correction on the magnitude of the error diminished rapidly with reduced raw error magnitude, with several errors even increasing after correction.

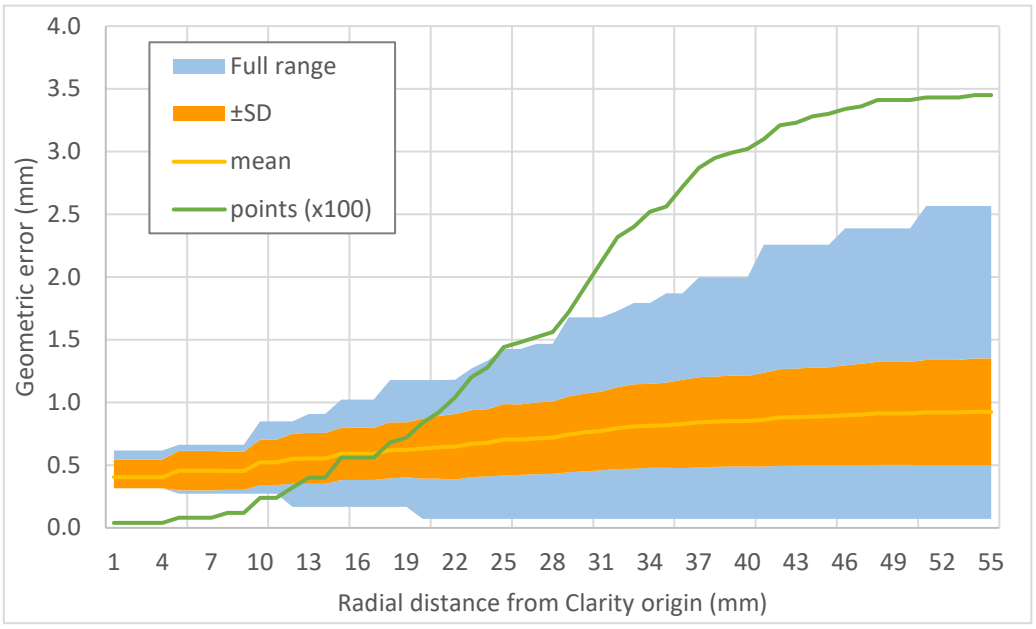

Figure 31: Corrected geometric error distribution of all points within the given radial distance from the Clarity origin (excluding points with tracking confidence < 0.5)

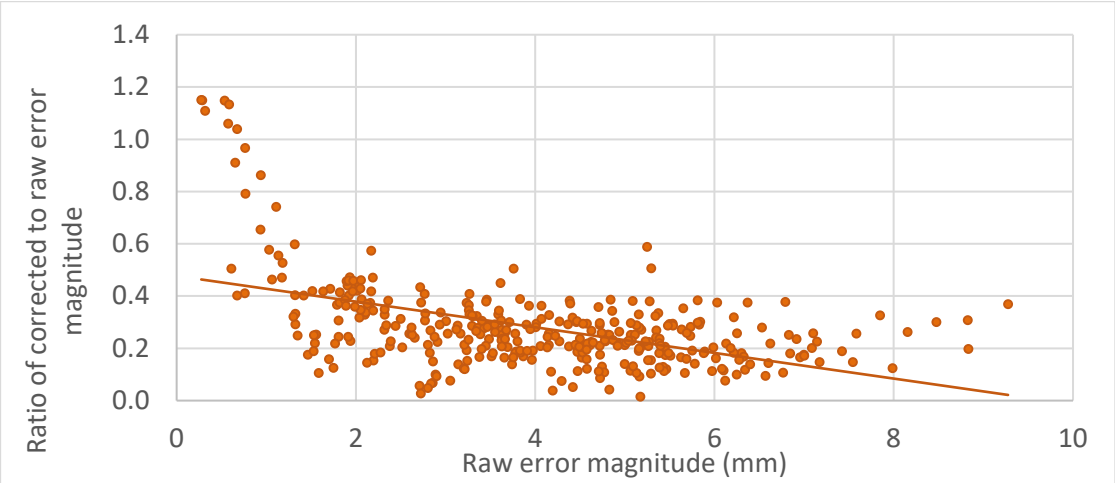

Figure 32: Ratio of corrected to raw geometric error magnitudes versus raw geometric error magnitude

This suggests that it would be inappropriate to use a single scaling factor to correct for refraction in the PMMA. Furthermore, a scaling factor would not be able to account for a change in direction of the error vectors following refraction correction, as is evident in Figure 29.

5.4.2 Geometric error magnitude uncorrelated with distance from Clarity probe

Considering instead the correlation between geometric error magnitude and the distance of the nominal positions from the assumed point source/receiver of the probe at the front of the tank, Figure 33 demonstrates that the magnitudes of the uncorrected error vectors were weakly negatively correlated, with R = -0.108; however, this correlation is reversed by the refraction correction, becoming positive (R = 0.120). The change in sign of both the slope of the linear trend in Figure 33 and the correlation due to the refraction correction suggests that it was effective at reducing the geometric error of the points that were subject to the greatest distortion, nearest to the inferior wall of the tank.

5.4.3 Correlation of geometric error with tracking confidence

As described in Chapter 4 (section 4.2.2), the output file containing the Clarity tracking data also included a quality index that described the level of confidence that the Clarity software had in each reported set of coordinates. Figure 34 compares the magnitude of the geometric error for each position after correction to the mean of the quality indices (QI) within the 10 second averaging

window used to find each position. Overall there is a moderate negative correlation between mean quality factor and corrected error magnitude (R = -0.327), however it is evident that there are at least two groupings in the data. The majority of points with QI > 0.9 appear to be uncorrelated whereas there appears to be a band of points grouped around the line given by y = 1 - 0.2x. Unfortunately, the reason for this could not be determined.

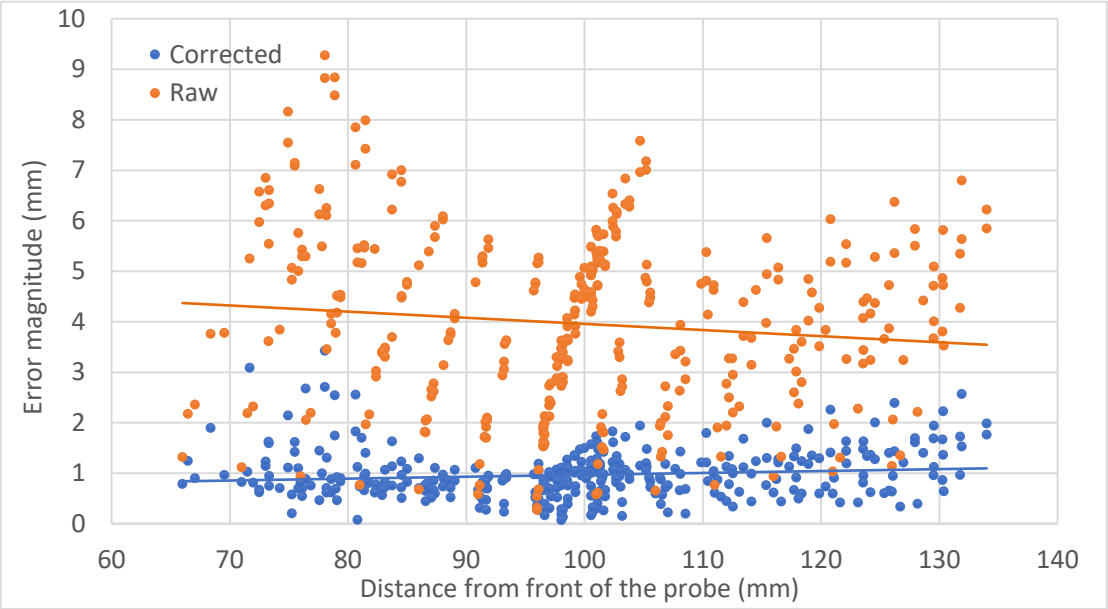

Figure 33: Error magnitude as a function of distance from Clarity probe

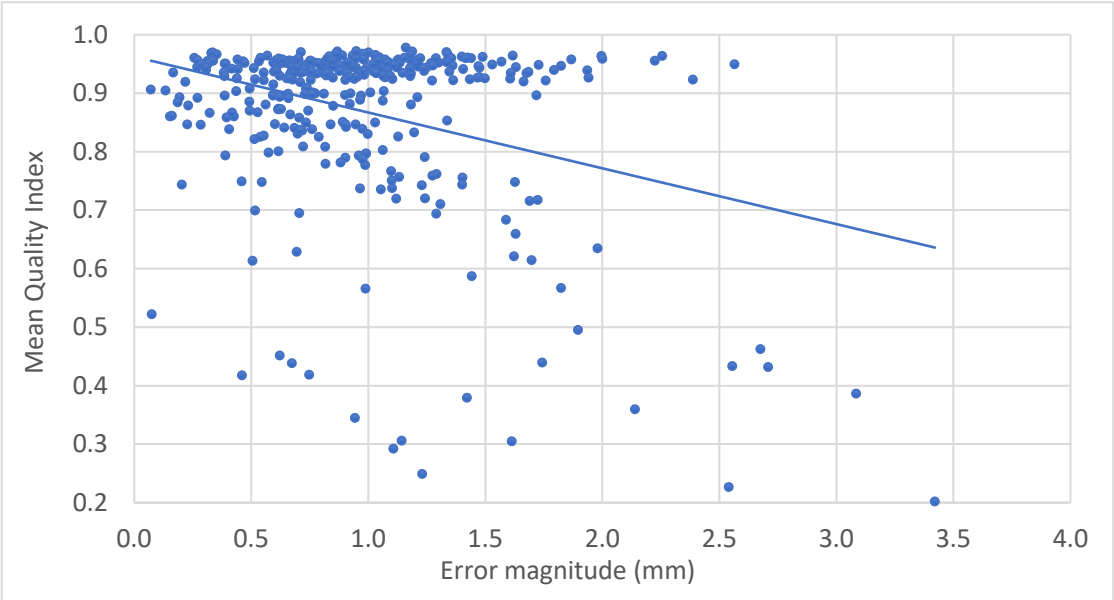

Figure 34: Correlation between error magnitude and mean quality index

There are 19 points with a mean quality index less than 0.5, which is the threshold at which the Clarity software will warn the user that tracking confidence is low. While there are a number of points with relatively low geometric error magnitude that had low tracking confidence, 6 out of 7 points with error magnitude greater than 2.5 mm also had low tracking confidence. The remaining point with very high confidence (0.95) and high corrected error magnitude (2.57 mm) corresponds to the point at the right-anterior-superior corner of the vector plot in Figure 29.

There are numerous points in the right-superior quadrant of Figure 29 with large geometric error and high tracking confidence which are not mirrored in the left superior quadrant, suggesting a misalignment in the experimental setup as described in Chapter 4. This demonstrates that despite taking great pains it is nearly impossible to perfectly align the coordinate systems.

5.4.4 Correlation of angle of refraction plane with geometric error magnitude

The relationship between the angle, θ, made between the plane of refraction and the positive Y-axis (see Figure 25), and the magnitude of the corrected geometric error can also be seen in Figure 35. All points with θ at or near to -180°, 0° or 180° are those whose nominal position lay in the coronal plane. All points at which θ is positive are those above the coronal plane and all negative angles are below it. The points clustered near 90° and -90° are those whose nominal position was in the sagittal plane, and the points lying along the -135°, -45°, 45° and 135° lines most notably include the points in the extreme corners of the volume, which happen to be among those with the highest error magnitude.

The points that are nominally in the sagittal and coronal planes generally do not appear to lie exactly in those planes following correction in Figure 35. Due to the discrete, well-spaced way in which the data were collected these points should lie either exactly on either 90° or -90°, or should be at least ≈10° away. The points highlighted red in Figure 35 were all among those that had a low quality index associated with them. If we disregard these points it appears that the maximum error magnitude below the coronal plane was approximately 2 mm, whereas the maximum point above the coronal plane (which had a quality index of 0.95) is above 2.5 mm.

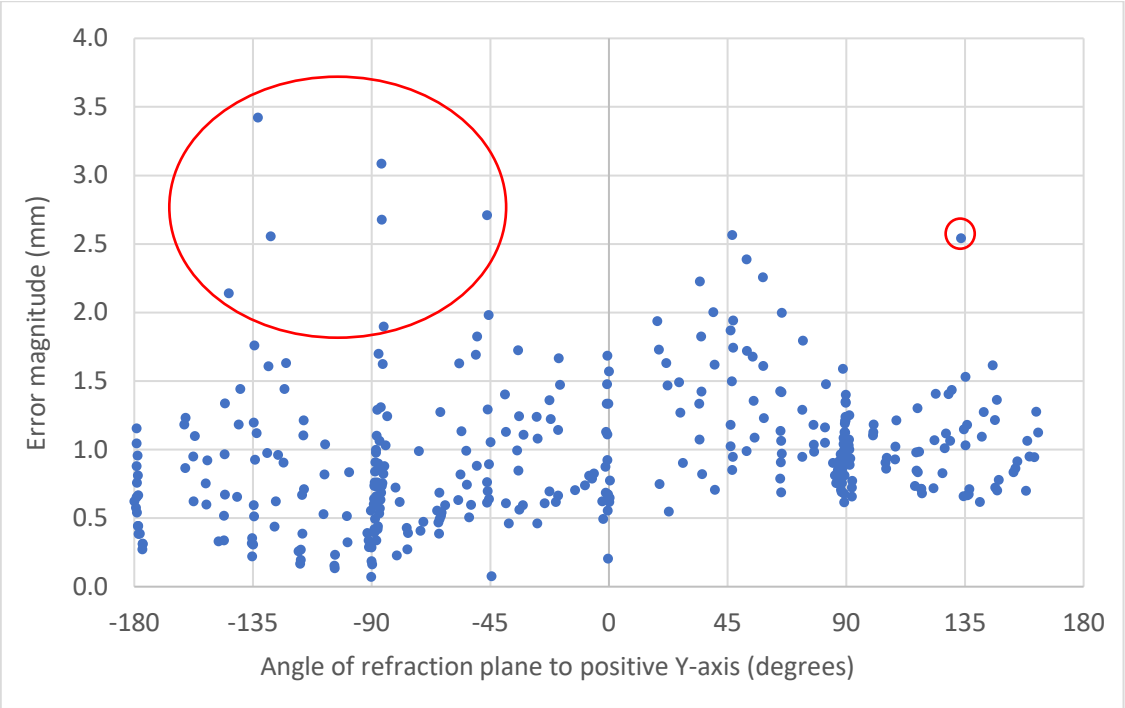

Figure 35: Relationship between θ and magnitude of corrected geometric error

Analysis of the raw data revealed that all points with $\theta \approx -180°$ nominally originated from the left half of the coronal plane, specifically the two half diagonals and the negative half of the left-right axis. It is noteworthy that they all fell in this region of the graph as this is indicative that they were not only measured to have a negative lateral coordinate, as expected, but also a negative vertical coordinate. That is, they all were measured to be slightly below the coronal plane. Note also the corresponding absence of points at the other end of the chart where $\theta \approx 180°$. If the coordinate systems had been more closely aligned then these points would be found evenly dispersed near both -180° and +180°. The points nominally from the positive half of the coronal plane are instead clustered near $\theta = 0°$.

The asymmetry about both the sagittal and coronal planes is consistent with a slight misalignment between the Clarity and the scanning tank coordinate systems and/or the alignment of the probe. If it can be determined through analysis of the asymmetry of the measured results what translations and rotations may have existed between the two coordinate systems then it might be possible to correct for these in a future version of the algorithm.

5.4.5 Dependence of lateral position on direction of mechanical sweep

During the acquisition of the lateral profiles it was observed that the real-time reported lateral position was varying slightly with a periodicity similar to the known frequency at which the transducer is swept laterally. Further inspection of the data exported from the Clarity server revealed a full-scale deflection of up to 1.3 mm with a period of approximately 2.5 seconds on top of the stepped features of the profile acquisition (Figure 36). As discussed in Chapter 4 (section 4.3.1), the average lateral position was affected differently across the volume from left to right as the widths of the peaks and troughs varied from left to right. This will have contributed to the uncertainty in the data and may have introduced a slight skew in the geometric errors across the volume.

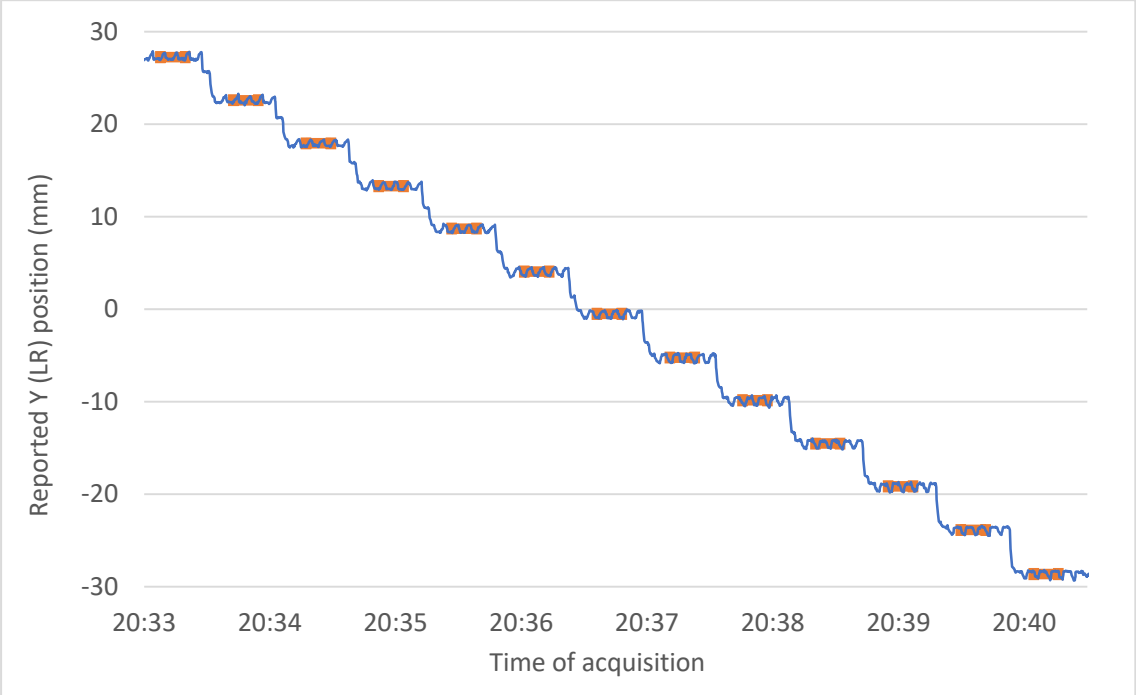

Figure 36: Example of lateral profile showing position dependence on sweep direction

The lateral profile shown in Figure 36 was the first of seven acquired sequentially, beginning with this uppermost profile at +30 mm in the vertical direction and ending with the lowermost at -30 mm (see Figure 26). Further analysis of the raw data revealed an apparent relationship between the vertical offset at which the profile was acquired and the magnitude of the scale deflection, regardless of the orientation of the profile (i.e. superior-inferior, left-right or diagonal). The maximum deflection within each of the 10 second windows was found and an average maximum

deflection determined for each of the profiles at the 7 depths. The +30 mm profiles were found to have an average maximum deflection of 1.0 mm, however the +20 mm profiles had a maximum average deflection of 0.7 mm, the +10 mm profiles had an average maximum deflection 0.5 mm and the profiles in the coronal plane had an average maximum deflection of 0.4 mm. The remaining 16 lower profiles also had average maximum deflections of 0.4 mm. As these profiles were acquired sequentially the dependence may be on acquisition time rather than vertical position, however prior to these profiles being acquired the system had been running for several hours and should have been well warmed up.

Following this discovery and unprompted by this work, the vendor for the Clarity Autoscan 4D-TPUS system released a field correction order (FCO: 345-05-CLA-003) which declared that at 100 mm from the probe an additional 0.4 mm uncertainty may be seen in the reported positions in the left-right direction. The central lateral profile above was acquired at a depth of 96 mm from the probe, therefore the vendor's FCO was taken as confirmation of these results.

5.4.6 Comparison with results from other investigations

Investigations into the tracking accuracy of the Clarity Autoscan system have been performed by other investigators [1-4, 34, 47, 48, 54], however each investigation has only looked at displacements from the normalisation point of ≤10 mm typical to a clinical scan. This study sought to cover a range of displacements that included both the worst-case situation of ±20 mm while also allowing for the target to be initially off-centre by up to 10 mm due to probe translation.

The experimental setup used for this study was unique. It does not appear as though the other investigators needed any corrections for their data as has been used here. Lachaine & Falco were the only other investigators to report a phantom study using nominal displacements of up to 10 mm. Considering only those points within 10 mm of the Clarity origin, the results of this work are in very good agreement with the findings of Lachaine & Falco. Similarly, the mean values reported herein for the entire volume are within the limits reported by Lachaine & Falco; however, as a result of the larger geometric errors farther from the origin, standard deviations determined in this work are somewhat larger for the larger sampling volume. Table 7 lists the findings of the other investigators as reported in Chapter 2.

5.5 Summary

The 2D refraction correction algorithm developed in Chapter 4 was rederived in vector form and extended to the third dimension using a rotation matrix, enabling the correction of any measured position within the ultrasound imaging volume. The 3D refraction correction algorithm was then tested on data acquired with the Clarity Autoscan 4D TPUS in a scanning water tank. Corrected results for points within ±10 mm are in agreement with the findings of other investigators.

The vectorised 3D refraction correction algorithm developed in this chapter enables the positional accuracy of the Clarity Autoscan 4D TPUS system to be validated using a scanning tank.

Table 7: Results of 3D refraction-corrected measurements compared to previous work

Study	*Method*	*Range of Motion*	*Result*
Lachaine & Falco 2013 [1]	U/S QC phantom on motion platform; optical tracking.	AP: ±10 mm LR: ±5 mm SI: ±4 mm	AP: -0.2 ± 0.2 mm LR: 0.2 ± 0.4 mm SI: 0.0 ± 0.2 mm
Abramowitz *et al*. 2012 [2]	Water phantom; RF beacons & optical markers on a stem.	Clinical prostate motion datasets from literature	Mostly within 1 mm (max 1.3 mm)
Yu *et al*. 2017 [3]	Pelvic phantom on motion platform; optical tracking.	LR/SI: ±3 mm	LR: 0.25 (0.23 RMS) mm SI: 0.18 (0.45 RMS) mm
Present work	Scanning water tank.	AP/LR/SI: ±30 mm (n = 345)	AP: -0.3 ± 0.6 mm LR: 0.0 ± 0.8 mm SI: 0.1 ± 0.3 mm Geometric error: 1.0 ± 0.5 mm
		AP/LR/SI: ±10 mm (n = 24)	AP: -0.2 ± 0.3 mm LR: 0.0 ± 0.4 mm SI: 0.0 ± 0.1 mm Geometric error: 0.5 ± 0.2 mm

Chapter 6: Dosimetric effect of interrupting the beam and shifting the patient

6.1 Introduction

Intrafraction prostate motion typically presents as either a gradual drift over time, or as a rapid but transient shift that can soon settle back to near the initial position. When a prostate excursion outside of the pre-defined threshold is detected by the Clarity Autoscan system during a patient treatment, the clinical procedure is to interrupt the beam and reposition the patient such that the target volume is once more centred within the treatment field. This will likely result in a change in both target depth and Source-to-Surface Distance (SSD) for at least some of the beam angles, which would be expected to have a measurable effect on the dose to the target. Hence the aim of this study was to quantitatively assess the effect of target drift during beam delivery as well as the effect on the dose delivered to the target due to the change in target depth.

Furthermore, the local procedure is to manually interrupt the beam when the Clarity Autoscan software registers an out of threshold prostate position. However, the recent addition of the Elekta Response gating system enables external devices such as Clarity Autoscan and the Elekta Active Breath Control (ABC) system used for the Deep Inspiration Breath Hold (DIBH) technique to automatically hold the beam. Therefore, this study will also attempt to quantify any difference to the dose delivered to the target between manual interruption and triggered beam hold.

6.2 Method

6.2.1 Experimental setup

The experimental setup was the same as for Chapter 5 with the prostate analogue replaced by an IBA FC-65G Farmer-type ionisation chamber (Figure 37). The chamber was connected to an electrometer for dosimetric measurement. To avoid repeating the simulation with the chamber instead of the table tennis ball, the same spherical volume defined in the Clarity Auto-Fusion and Contouring (AFC) workstation encompassing the ball was used at the linac to track the graphite thimble of the Farmer-type chamber (Figure 38).

Figure 37: Experimental setup for dose measurements

Figure 38: Clarity display showing tracking volume surrounding chamber thimble in sagittal (left) and coronal (centre) planes

Before attempting the dose measurements, it had to be confirmed that Clarity could track a sphere in which only some of the material in the volume would remain unchanged, since a spherical tracking volume around the chamber thimble would include water that can freely move in and out of the volume. Chamber displacements were programmed ±30 mm from the isocentre in each direction. Clarity was able to track the chamber position despite the water diffusing through the volume.

The only noticeable difference between the tracking of the table tennis ball and tracking the thimble ionisation chamber was the scale of the difference from the nominal displacements. Where the Clarity-reported position of the ball was approximately 24.5 mm for a nominal displacement of 30 mm, the displacement of the centroid position of the tracking volume around the Farmer-type ionisation chamber was reported to be approximately 26.1 mm. This was assumed to be a result of tracking a volume that was less susceptible to distortion effecting the centroid calculation. However, in order to trigger a target excursion of a known displacement the thresholds defined in the AFC workstation had to be scaled down. This was necessary because Clarity will under-report the displacement of the chamber due to the refraction and would therefore take longer to register a threshold excursion.

The local clinical thresholds are the same as the GTV-PTV margins used at the treatment planning stage: 5 mm in every direction except for posteriorly which is set to 3 mm to reduce rectal toxicity. Therefore, the thresholds were modified at the AFC workstation to 4.35 mm anteriorly and 2.61 mm posteriorly to compensate for the distortion due to refraction. Alternatively, the programmed target motion could have been scaled instead of the thresholds, however this would also have affected the dose measured by the ionisation chamber.

One aim of this experiment was to assess the dosimetric difference due to changes in depth and SSD to the target volume – i.e. not due to lateral excursions of the target volume outside the PTV. Lateral excursions were not being investigated here as any clinically relevant displacement would still have the chamber within the treatment volume. Therefore, a static 10 cm x 10 cm radiation field was used for all measurements. The gantry and collimator angles were also static throughout the experiment with both set to 0 degrees. Because of this configuration any measured dose differences are only relevant to non-arc delivery in which the motion is occurring parallel to the

beam axis. Furthermore, the difference will only apply to an individual field and may even be negated by an opposing field.

The initial ionisation chamber depth and SSD were set to 10 cm and 90 cm respectively in order to approximate patient treatment conditions. The front pointer typically used for setting the SSD could not be installed due to the presence of the tank, so this had to be performed using a non-standard approach. The ionisation chamber was first set to the correct depth in water, then the treatment couch on which the water tank was positioned was raised until the coronal laser was aligned with the effective point of measurement of the ionisation chamber. This will have introduced a slight uncertainty in the initial SSD but was deemed to have minimal impact on the results as the dose measurements will all be relative to a static measurement, with no chamber motion.

6.2.2 Data acquisition

All measurements were performed with the gantry and collimator set to 0°, and the field size set to 10x10 cm^2. The starting position for all measurements, both static and dynamic, was with a SSD of 90 cm and the chamber 10 cm deep. A total of six different configurations were used for the data acquisition, beginning with static, baseline dose measurements in the initial configuration as described above, against which the subsequent measurements could be compared. The remainder of the configurations involved target motion in only the vertical (anterior-posterior) direction during beam delivery with and without intervention such as beam interruption and 'patient' repositioning. Using only vertical movements simulated a displacement along the beam axis during a step-and-shoot IMRT field, which is relevant to any gantry angle for motion parallel to the beam axis. Following each of the non-static configurations the baseline measurements were repeated in order to confirm the stability of the linac output throughout the study.

A. Static baseline measurements

1000 monitor units were delivered to warm up the linac and measuring devices. The electrometer was zeroed for background radiation and/or leakage, and the water temperature and ambient barometric pressure were measured. 200 monitor units were delivered for each baseline measurement, and the charge accumulated in the ionisation chamber measured and recorded via the electrometer. The temperature and pressure would be used to correct the charge readings for atmospheric conditions.

B. Transient displacement with Response beam suspension – dose difference

The first of the non-static configurations was designed to simulate the situation seen occasionally in the clinic whereby a rapid prostate excursion due to, for instance, the patient coughing results in the beam being interrupted. Occasionally, after a brief wait, the prostate naturally returns to within the thresholds allowing treatment to continue without the need for remedial action such as repositioning the patient. To simulate this a rapid excursion of 10 mm in the anterior direction was performed from the linac control room midway through the delivery of a 200 monitor unit (MU) beam using the water tank control software. The Clarity software was allowed to trigger a beam hold when the 5 mm threshold was crossed via the Response system. Once the beam was held the chamber was programmed to move back to the initial position, after which the beam was resumed. Once the beam had terminated at 200 MU the total charge accumulated throughout the full 200 MU was recorded. This was repeated until ten measurements had been acquired, and then repeated for displacements in the posterior direction with the 3 mm threshold. The SSD and depth were the same as for the baseline measurements.

C. Transient displacement with Response beam suspension – delay

The third configuration was designed to determine the time delay as a function of MU delivered between the actual motion of the target volume outside of the threshold and when the beam was suspended. A 20 mm/s vertical movement was manually triggered as near as possible to the moment when the linac displayed that 50 MU had been delivered. Once the beam had paused, the MU that had been delivered was recorded. Unfortunately, this method includes several inherent uncertainties, such as the difficulty in accurately and repeatably triggering the movement at the 50 MU mark, and the fraction of the delay due to motion of the chamber before the threshold is crossed. However, at 20 mm per second it should have taken only 0.25 seconds for the volume to cross the anterior threshold. This arrangement was also repeated until ten measurements had been acquired, and then repeated for displacements in the posterior direction.

D. Continuous motion with no beam suspension

Fourthly, somewhat of a worst-case scenario was simulated, in which a steady target motion was programmed such that the target had moved approximately 20 mm toward the x-ray source without interruption by the end of the beam delivery. In order to achieve this the minimum speed of the

tank scanning mechanism and the linac dose rate had to be taken into consideration. The minimum speed of the scanning mechanism is 1 mm per second while the dose rate of the linac on the day that the measurements were taken was approximately 550 MU per minute. Therefore, the linac was programmed to deliver beams of 180 MU which would allow the chamber to move approximately 20 mm at 1 mm/s by the time the beam terminated. The chamber motion was triggered manually within the first 10 MU as the dose rate ramped up.

As with the previous configuration, there were inherent uncertainties in this procedure including human reaction time and minor variation in the linac dose rate; therefore, 10 measurements were taken for each of the anterior and posterior directions to try to reduce the impact of these variations.

E. Continuous motion with Response beam suspension and 'patient' repositioning

The fifth configuration was the same as described in *D*. except that this time Response was used to automatically suspend the beam after the deviation outside of the threshold had been detected by the Clarity software. The pre-programmed motion was allowed to continue with the beam still paused until an anterior displacement of 20 mm from the isocentre had been reached. Once the chamber had stopped moving the couch was moved down 20 mm based on the linacs digital display within the treatment room so that the chamber would once more be at 100 cm from the source (I.e. SSD = 92 cm, depth = 8 cm). The beam was then resumed until 180 MU had been delivered and the total accumulated charge recorded. This was repeated until ten measurements had been acquired, and then repeated for motion in the posterior direction.

The integration of the Clarity system with the Elekta linac enables the offsets reported by the Clarity software to feed directly into the linacs Couch Move Assist (CMA) module and thereby reposition the target remotely from the control room. However, this feature was not used here as it was known that the Clarity reported positions would not correspond with reality due to refraction in the tank wall as described above.

This configuration was designed to be compared to both the baseline values and those from section *D*. so that a comparison could be made between the same situation with and without operator intervention.

F. Continuous motion with manual beam suspension and 'patient' repositioning

The final arrangement was intended to determine whether there was a measurable difference in total dose delivered between manual beam interruption and Response automatic beam suspension. Hence the configuration was the same as the previous test with the exception that the Response unit was switched off and the beam interrupted manually when an excursion greater than the threshold was indicated by the Clarity software. Once again this introduced the uncertainty due to variation in human reaction time.

6.3 Results

Given that the following comparisons to this baseline reading are relative it was not necessary to convert the charge readings to dose; however, two key factors in calculating the dose may have changed across the several hours that these measurements were made: the atmospheric temperature and pressure affecting the response of the chamber and the dose rate variation of the linac. Therefore, at each stage the atmospheric correction factor, k_{TP}, was calculated and the charge re-measured with the chamber stationary. From Kahn [77], the atmospheric correction factor is given by

$$k_{TP} = \frac{p_0 \times (273.2 + T)}{p \times (273.2 + T_0)} \tag{25}$$

where $T_0 = 20° C$ and $p_0 = 101.325\ kPa$ are normal temperature and pressure, and T and p are the measured values. The k_{TP} -corrected mean ± SD baseline charge reading for 200 MU with the stationary chamber at 10 cm depth in water was 33.35 ± 0.02 nC after 8 consecutive measurements.

6.3.1 Transient displacement with automatic beam suspension – dose difference

A rapid 10 mm vertical movement was initiated midway through a 200 MU beam triggering the Clarity threshold and hence the Response beam interrupt. The chamber was moved back to its original position and the beam completed. The k_{TP}-corrected mean and standard deviations for both the vertical movements and the stationary measurements are presented in Table 8. The transient displacements in the beam axis outside the monitoring threshold resulted in a dose difference of a little over 1% in each direction. However, this will have depended on several factors

including the magnitude of the displacement, the time delay before Clarity and Response suspended the beam and the total beam duration. Therefore, the next section will attempt to estimate the delay between the threshold crossing and the suspension of the beam.

Table 8: Charge readings for transient vertical threshold crossing

	Stationary	*Up 10 mm*	*Down 10 mm*
Mean (nC)	33.37	33.81	32.96
SD (nC)	0.02	0.08	0.07
Difference from Stationary		1.3%	-1.2%

6.3.2 Transient displacement with automatic beam suspension – delay

This test did not require the dose to be measured, only the MU recorded once the beam had been suspended by the Clarity and Response systems. 50 MU was subtracted from each reading to yield the extra MU delivered after the movement was initiated. The extra MU varied considerably, ranging from 36 to 61, with mean ± SD of 49.3 ± 8.7. Figure 39 shows the approximate time delay in seconds for each reading, calculated using the known linac dose rate on the day of 552 MU per minute. The orange line indicates the approximate time that the movement was initiated. The calculated time delays ranged from 3.9 to 6.6 seconds and the mean ± SD was 5.4 ± 0.9 seconds.

While every effort was made to initiate the chamber motion as soon as the linac MU display reached 50 MU, as the linac output rate was approximately 9 MU per second there was likely a ±5-10 MU uncertainty due to human error. Furthermore, the threshold crossing would not have been instantaneous upon initiation of the chamber motion and would also likely have contributed up to 0.25 seconds to the delay timing. The combined effect may have added at most approximately 1 second to the delay.

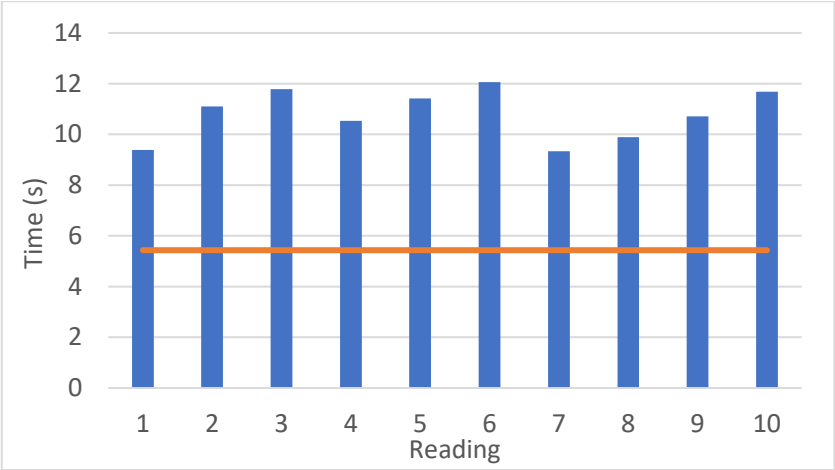

Figure 39: Response beam hold delay calculated from MU after beam hold triggered

6.3.3 Continuous motion with no beam suspension

This test was designed to simulate a worst-case scenario in which the target gradually moves 20 mm along the beam axis throughout the delivery. Only 5 readings were taken in each of the anterior and posterior directions as these readings were found to be quite stable. The readings were then scaled up to account for only 180 MU delivered, and corrected for atmospheric conditions. Subsequent stationary readings were made and the percent difference in charge readings calculated (see Table 9).

Table 9: Charge readings from uninterrupted movement along beam axis

	Stationary	*Up 20 mm*	*Down 20 mm*
Mean ± SD (nC)	33.34 ± 0.01	34.79 ± 0.02	31.95 ± 0.03
Charge difference from Stationary		4.4%	-4.2%

6.3.4 Continuous motion with automatic beam suspension and 'patient' repositioning

Accumulated charge in the ionisation chamber was measured while the chamber moved slowly along the beam axis as in section 6.3.3, however this time Clarity and Response suspended the

beam after the threshold was crossed. The chamber completed its programmed movement with the beam off, then the couch position was adjusted once the chamber had reached 20 mm. The remainder of the MU was delivered with the chamber stationary at 20 mm offset from its starting position. Table 10 shows that the means of the total accumulated charge readings in each direction were very similar to those in section 6.3.3, but with slightly higher variance. The mean ± SD MU when the beam was suspended are also shown for comparison with the manual beam suspension results to follow.

Table 10: Total charge readings from continuous motion with automatic beam suspension and 'patient' repositioning

	Stationary	*Up 20 mm*	*Down 20 mm*
Total Charge: Mean ± SD (nC)	33.34 ± 0.01	34.84 ± 0.07	31.98 ± 0.12
Interrupted: Mean ± SD (MU)		111.5 ± 4.6	87.1 ± 7.8
Charge Difference from Stationary		4.6%	-3.9%

6.3.5 Continuous motion with manual beam suspension and 'patient' repositioning

The Response gating kit was deactivated and the beams interrupted manually following the prompting by the Clarity software. The couch was repositioned and the remainder of the beam delivered. Table 11 shows the mean and standard deviation of total accumulated charge readings for each direction compared to the stationary measurements.

Table 11: Total charge readings from continuous motion with manual beam suspension and 'patient' repositioning

	Stationary	Up 20 mm	Down 20 mm
Total Charge: Mean ± SD (nC)	33.49 ± 0.01	34.89 ± 0.03	32.03 ± 0.11
Interrupted: Mean ± SD (MU)		117.9 ± 3.9	90.2 ± 5.8
Charge Difference from Stationary		4.2%	-4.2%

6.4 Discussion

As discussed in Chapter 2, numerous retrospective planning studies have been conducted investigating the dosimetric effect of intrafraction prostate motion on the target and organs-at-risk; however, none could be found that involved *in silico* direct dose measurements. The aims of this experiment were three-fold: firstly, to assess the effect on the dose to the target due to a transient excursion outside the threshold, to measure the change in target dose due to a slow target drift with and without intervention, and to see if there was a measurable difference in dose between automatic and manual beam interruption.

The transient excursion outside the threshold resulted in approximately 1.2% difference in measured dose; however, this result is highly dependent on several factors including the magnitude of the displacement, the linac dose rate and the total duration of the beam. Therefore, the most significant result here is the time delay between threshold crossing and beam suspension as this is independent of beam settings. If a flattening-filter-free (FFF) technique was employed with a 6 MV beam dose rate approximately 2.5 times greater, as much as 150 MU might have been delivered while the target was partially outside of the planned high-dose. Conversely, at a normal dose rate (500 – 600 MU/min.) with a larger total MU the dose difference would be lower as the delay would be a smaller fraction of the total beam-on time. The variation in the delays was not unexpected given the 2.5 second period of the mechanical sweep of the transducer, however it seems that the imaging plane may make at least two passes over the target before the beam hold is triggered.

Table 9 to Table 11 show that there was an approximately 4% difference in the dose to the target when it moved 20 mm during the delivery of a single field, but that there was little difference in dose to the target between intervention and no intervention. There did, however, appear to be a discernible difference in the average MU between automatic and manual beam suspension corresponding to approximately 0.5 seconds longer delay for manual interruption. While it is interesting that intervention had little effect on the total dose, the motivation for motion management is in maintaining target coverage in a highly conformal field and minimising dose to organs-at-risk by keeping them out of the high dose region.

The continuous motion tests were intended to mimic a worst-case effect on dose to the target in terms of the magnitude of the displacement and direction along the beam axis. This method has not examined the effect of lateral movement of the target out of field. This would be very difficult to achieve via direct measurement whilst monitoring motion with the Clarity 4D-TPUS. If the current setup were used, any clinically relevant lateral displacement would still have the chamber within the field. Furthermore, one could not simply use an array of diode or ionisation chambers as it would not be possible to include the Clarity system for monitoring in this arrangement.

The sagittal view in Figure 38 shows considerable artefact below the chamber due to reflection off the cross bar of the scanning mechanism. If the chamber had been oriented vertically, with thimble pointing upward, the cross bar of the scanning mechanism to which it was attached would have been well out of the way; however, the Farmer-type ionisation chamber is not typically be used in this orientation relative to the beam axis but might be OK for relative measurements. Possibly a different detector such as a photon diode could be used in this orientation, although being much shorter than the Farmer-type chamber the cross-bar artefact might still be in the ultrasound field-of-view.

6.5 Summary

The worst-case target drift during beam delivery was simulated and the effect of Clarity-triggered intervention on the dose to the prostate assessed. System latency due to mechanical sweeping of the transducer proved to be a significant factor. Manual versus automatic beam hold showed little dosimetric difference.

Similarly, repositioning following a target excursion along the beam axis had little effect on the dose to the centre of the target; however, motion will not always be parallel to the beam axis and multiple gantry angles employed.

Repositioning is still necessary in conformal and intensity modulated techniques used clinically to maintain target coverage: the dose to the centre of the volume may not change significantly but the periphery of the target volume may move outside of the treatment volume. Furthermore, as the target volume moves out of the treatment volume the organs at risk may move into the treatment volume thus negatively impacting dose minimisation to these organs.

Chapter 7: Conclusion

The purpose of this project was to determine whether a scanning water tank intended for linear accelerator dosimetry could be used to validate the positional accuracy of the Clarity Autoscan TPUS IGRT system throughout a clinically relevant volume. Initial testing was performed to demonstrate that a prostate analogue could be tracked through the side wall of the scanning tank despite the mismatch in acoustic impedance between PMMA and water. Testing not only confirmed that tracking was possible through the PMMA but also the expectation that the speed of sound in the two materials would need to be compensated for through time-of-flight and refraction corrections as it differed from that expected by the ultrasound system.

The refraction correction algorithm incorporating time-of-flight correction was developed through two rounds of algorithm development and empirical testing, firstly as a bi-layer 2D correction for points in the sagittal and coronal planes before being extended to 3D. This enabled the tank to be used for the verification of the of positions reported by the Autoscan system throughout a clinically useful range of motion by comparison with the programmed displacements from a normalisation point. The refraction and time-of-flight-corrected positional measurements were found to be in agreement with those reported by other investigators over a significantly smaller range of motion. Furthermore, lateral displacements of an ultrasound phantom of the same magnitude as those made in water confirmed the calibration of the algorithm. The ultrasound phantom was constructed of a material with speed of sound matching that of soft tissue negating the need for speed of sound or refraction correction.

Intrafraction motion management was also investigated using programmed displacements of the target object during beam delivery. Dose to the centre of a target volume was measured while stationary as well as during both rapid and gradual displacements outside of the Clarity intervention thresholds. Dose to the centre of the target volume was measured with and without intervention triggered by the Clarity system. Under the current experimental arrangement, it was found that there was little difference in dose to the centre of the target between allowing the target to continue to drift and suspending the beam to reposition the ‘patient’; however, this says nothing about the effect on overall target coverage and dose to organs at risk.

A dose comparison was also made between manual interruption by the user when prompted by the Clarity interface and allowing the Clarity system to directly interface with the linear accelerator and suspend the beam automatically. It was found that there was little difference to the dose to the centre of the target volume whether the beam between manual and automatic beam suspension. Finally, the latency between target motion outside the Clarity thresholds and actual beam suspension was assessed. It was found to be higher than expected at around 5 seconds.

In conclusion, it has been demonstrated that a scanning water tank can be used to verify the positional accuracy of the Clarity Autoscan 4D TPUS system with the application of appropriate corrections.

7.1 Future work

7.1.1 Speed of sound in the tank wall

One obvious source of uncertainty in this work surrounds the determination of the speed of sound in the PMMA of the tank wall. While this parameter has essentially been used herein as a calibration factor, ideally the true value would be used and an additional correction factor incorporated to account for all other sources of uncertainty. Given that there is a significant difference between the published values and that used in this work, it may be possible to devise a method that involves a range of positional measurements being made along the full range of the longitudinal axis and time-of-flight calculation. As discussed in section 3.4.4, normalisation of the initial starting point cancels out much of the effect of the time-of-flight in the tank wall along the longitudinal axis; therefore, it would be necessary to instead make distance measurements of the depth of the object in the ultrasound images, rather than using the Clarity-reported position. This would likely involve its own significant uncertainty, but it might be possible to determine which of the values reported herein is closer to the true value.

7.1.2 Improved modelling of probe internal geometry

A critical assumption of this work was the treatment of the Clarity probe as a point source and detector of the ultrasound waves: This is clearly not the case with the sweeping 2D transducer and hence this simplification may account for much of the difference in the speed of sound in PMMA used in this work compared to the IEC published value. Therefore, it may be instructive to more accurately model the geometry of the internal mechanism of the probe. This might be achieved by

treating the source point as being deeper within the probe, coinciding with either the pivot point of the transducer or merely at the point of intersection of the fan representing the acquired ultrasound slices. This would have the effect of distributing the source point across a finite width of the tank surface. It is noteworthy, however, that this geometry should require a smaller refraction angle in the PMMA which would correspond to an even lower speed of sound in PMMA compared to the published value.

7.1.3 Reducing analogue distortion due to refraction

One experimental change that might improve the positional measurements beyond a refractive layer would be to reduce the size of the prostate analogue, or more specifically the size of the tracking volume. This would have the effect of reducing the distortion of the analogue, which in turn should improve the accuracy of the tracking volume centroid position calculation. Furthermore, an alternative material to the water-filled table tennis ball that has significant contrast relative to water without the hard, reflective shell, might be more readily tracked.

It might also be possible to assess the error in the centroid position calculation if it were possible to access the 3D image data. A ray-tracing refraction correction akin to that developed by Fontanarosa *et al*. [42-44] could be propagated throughout the volume to determine the true centroid position and compare it to that reported by the Clarity system. While the Fontanarosa *et al*. correction relies on a CT dataset to perform the voxel-wise refraction correction, the simple geometry of the present experiment is fairly well known, and the correction could be applied to only the known boundaries. It would also be interesting to see the result of applying the bi-layer 3D refraction correction developed in this work to the 3D ultrasound image dataset and compare it to the known geometry of the experimental setup.

7.1.4 Algorithm correction for probe setup errors

As mentioned in section 5.4.4, it might be possible to improve the accuracy of the algorithm by correcting for errors in the setup of the probe, concerning its position and orientation relative to the tank wall and scanning axes. The positional data collected nominally in the sagittal plane might be used for this purpose. For instance, the corrected positions nominally along the longitudinal axis could be evaluated to determine the offsets and angles that could be introduced to put them (mostly) back on the axis. These corrections could be assumed to be due to probe positioning

uncertainty and therefore applied to the entire corrected dataset. Data at the upper and lower extremities of the sagittal plane could be used to assess roll rotations. Preliminary efforts have already been made to implement this, however it was found to be non-trivial due to the distributed nature of the algorithm as it has been implemented piecewise using multiple applications. The solution would be to fully implement the entire process end-to-end in MATLAB only, and incorporate one or more additional loops to post-process the corrected results.

7.1.5 Effect on tracking accuracy of focal depth selection

Throughout this work the default scanning parameter set was used, including the focal depth setting. The rationale for this was that a) it was sufficient for the needs of the project with regard to testing the utility of a scanning tank for positional accuracy verification, and b) many clinical operators of the system will not be expert in ultrasound imaging and will likely retain the default parameters if the image quality is sufficient. However, now that the utility of this method has been demonstrated it would be instructional to investigate the impact on tracking accuracy of the various imaging parameters, particularly the focus depth at it can directly affect lateral resolution due to the changes induced in the ultrasound beam profile.

Appendix: Supplementary Quality Control tests

Routine QC tests for the Clarity Autoscan system were established to supplement the recommendations of the manufacturer and existing clinical practice. In the absence of existing guidance concerning QC of 3D and 4D ultrasound systems, these tests were adapted largely from AAPM TG-128 [65] and TG-154 [78] to higher dimensional acquisition. TG-154 emphasises the motion monitoring aspect of systems such as the Clarity 3D transabdominal ultrasound, whereas TG-128 is focused on image quality for ultrasound-guided prostate brachytherapy. Additional guidance was taken from the academic community concerning system integrity [79, 80].

The tests have been divided into two groups: image quality, including geometric accuracy; and general system checks including positional tracking reliability. Many of the tests of image quality and system integrity recommended by TG-128 and TG-154 are either already part of routine linac QC, or are unnecessary for current clinical practice in the author's centre; therefore, these tests have been assigned a local test ID of 'N/A' (see Table 13 and Table 14) as the intent is to supplement existing clinical practice. These two elements will be discussed separately before the combined set of quality control tests is presented.

A.1 Image quality tests

The Clarity Autoscan system has three different acquisition modes that were used for image quality testing: the 2D "Live Guidance" mode that is used for improved probe positioning and repeatability; the 3D reference mode used for simulation and pre-treatment, and the 4D monitoring mode. Unlike typical diagnostic systems the Clarity acquisition station does not provide analysis tools such as an image freeze function or electronic calipers to perform measurements, and the 2D Live Guidance images cannot be retrieved for offline analysis. Therefore, only online, qualitative assessments can be performed in 2D mode such as those requiring only visual inspection of QC phantom images in real-time.

Some 3D data and snap-shots of 4D data can be accessed offline for analysis at the AFC workstation, however the ruler tool for length measurements in the AFC workstation is only available in the software during a registration session; otherwise, lengths may be estimated to within reasonable precision using the grid tool.

A CIRS general purpose ultrasound phantom (model number 054GS) was purchased for the image quality assessment, as it includes all the necessary elements for image quality analysis (Figure 40) to be discussed later.

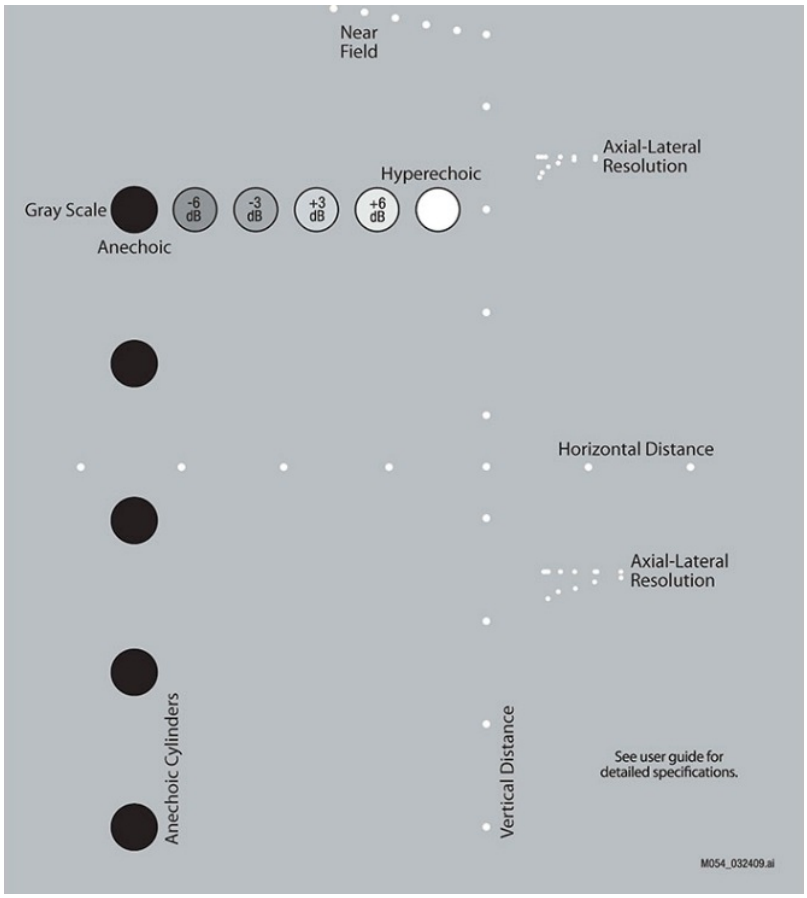

Figure 40: General purpose ultrasound phantom target diagram

Table 12 lists the image quality tests recommended by TG-154 to be performed by a Qualified Medical Physicist (QMP) semi-annually and section V.I. of the TG-154 report discusses how these can be determined using an ultrasound QC phantom.

Table 13 lists the image quality tests recommended by TG-128 including frequencies and action levels; however, a number of these tests either are not relevant or cannot be performed. Grayscale visibility as described by TG-128 is not possible as the Clarity user interfaces do not provide the necessary measuring tools, however the phantom provides a lower resolution method of analysis by the inclusion of 6 known contrast elements. Needle template alignment is only relevant to ultrasound for brachytherapy.

Table 12: TG-154 TABLE III. Image quality QA; performed by the QMP on a semi-annual basis.

Test	*Tolerance*	*Local Test ID*
Spatial Resolution	Compared to Baseline	IQ1
Low Contrast Resolution	Compared to Baseline	IQ2
Sensitivity	Compared to Baseline	IQ3
Hardware Degradation	Streaks/Artefacts	IQ4

Measurements of length, area and volume are also not possible at the acquisition cart as intended by TG-128; however, length and volume measurements can be performed offline using at the AFC workstation, so axial and lateral scaling measurements are achievable for 3D mode only. TG-128 provides tolerances which will provide a good starting point for establishing the new tests.

IQ1 – Spatial resolution

Axial resolution is assessed using the CIRS phantom via the two sets of wires labelled “Axial-lateral resolution” in Figure 40 by identifying the closest pair of wires that can be resolved vertically. Similarly, lateral resolution is assessed by identifying the closest pairs of neighbouring wires that can be resolved horizontally. The user manual provides tables of the spacings between each of the wires in both sets. For best results the ultrasound probe should be perpendicular to the phantom window and offset laterally such that it is centred over the sets of wires. The probe may be rotated 90 degrees to assess axial resolution in the reconstructed direction in 4D mode. 2D and 4D modes can be assessed under live scanning conditions without the need to export images to the AFC workstation.

IQ2 – Low contrast detectability

The anechoic cylinders arranged vertically to the left of Figure 40 can be used to assess low contrast target detectability. According to the phantom user manual, low contrast structures tend to appear smaller under ultrasound imaging than they actually are and may not be visible at all at

greater depth. Ideally, the live image would be frozen and the sizes measured at the acquisition station, however as this is not possible with the Clarity system it will suffice to count the number of cylinders that are visible.

Table 13: TG-128 TABLE II. Quality control tests: frequencies and action levels.

Test	*Minimum Frequency*	*Action Level*	*Local Test ID*
Grayscale Visibility	Annual	Change 2 steps or 10% from baseline	c.f. IQ5
Depth of Penetration	Annual	Change 1 cm from baseline	IQ3
Axial and Lateral Resolution	Annual	Change 1 mm from baseline	IQ1
Axial Distance Measurement Accuracy	Annual	Error 2 mm or 2%	c.f. IQ6
Lateral Distance Measurement Accuracy	Annual	Error 3 mm or 3%	c.f. IQ6
Area Measurement Accuracy	Annual	Error 5%	N/A
Volume Measurement Accuracy	Annual	Error 5%	N/A
Needle Template Alignment	Annual	Error 3 mm	N/A
Treatment Planning Computer Volume Accuracy	Acceptance Testing	Error 5%	IQ7

Table 14: TG-154 TABLE II. Quality assurance tests, tolerances and frequencies for U.S. guided radiation therapy.

Test	*Tolerance*	*Comments*	*Frequency*	*Performed by*	*Local ID*
Laser Alignment	1 mm	Required for subsequent testing	Daily	QMP or therapist	N/A
Daily Positioning Constancy	2 mm	Treatment room and simulator if applicable	Daily	QMP or therapist	N/A
Depth, Gain Controls	Functional		Daily	QMP or therapist	SI2
IR Camera Warmup	Manufacturer specifications	Verify proper warm up / calibration	Daily	QMP or therapist	N/A
Phantom Stability	1 mm		Quarterly	QMP	N/A
Monthly Positioning Constancy	2 mm	Similar to daily positioning constancy. Includes infrared camera calibration	Monthly	QMP	SI3
Phantom Offset Test	2 mm	Treatment room	Monthly	QMP	(SI4)
Laser Offset	2 mm	Sim room If applicable alternate between CT zero and offset position every other month.	Monthly	QMP	SI5
Image Quality Constancy	See Table III		Semi-annually	QMP	N/A
End-To-End Testing	2 mm		Annually or after software upgrade	QMP	SI6

IQ3 – Sensitivity/Depth of penetration

The Sensitivity is defined as the greatest depth at which echoes can be seen from the background material of the phantom. Unlike x-ray imaging, within the sensitive region of the image the background signal of an ultrasound image is predominantly due to echoes off the background material, more so than random noise. At the limit of the sensitive region the character of the background signal can be seen to change in live scanning mode since the electronic noise is continuously changing, while background echoes don't change if the probe is stationary. Critically, contrast elements such as wires may be seen *beyond* the depth of penetration so one cannot simply determine the sensitivity based on the last visible wire.

Unfortunately, it may be difficult to distinguish background echo from electronic noise in an exported image as the electronic noise will only be changing in the live images. Therefore, it may be necessary to estimate the sensitivity relative to the positions of the vertical distance wires online (Figure 40) rather than using the ruler or grid tools offline at the AFC workstation.

IQ4 – Image uniformity and artefact identification (hardware degradation)

A uniform region of the phantom is used to assess the lateral uniformity of the 2D image. When assessing the uniformity, it must be remembered that regions downstream of a high contrast inclusion will be shadowed due to signal attenuation. Conversely, low contrast elements have little or no attenuation, so the image is expected to be non-uniform beyond these elements.

Streaking can be caused by dead or under-performing transducer elements [52] and repeating noise throughout the image can indicate a poor electrical connection due to, for instance, a damaged signal cable. Visual inspection of the images may reveal hardware degradation so any artefacts observed should be noted in the final testing report.

IQ5 – Grayscale visibility

The grayscale visibility test described by TG-154 utilises a scale bar typically found on the display of a diagnostic ultrasound unit which is not present on the Clarity Autoscan system. However, the CIRS phantom has 6 contrast objects embedded that can be used to assess grayscale visibility. As with IQ1, all scanning modes can be assessed from the live imaging feed.

IQ6 – Axial and lateral scaling (3D and 4D only)

TG-128 recommends a test of the measurement accuracy of the electronic caliper function found on diagnostic ultrasound systems, which is not present on the Clarity Autoscan system. It is still considered important that the axial and lateral scaling of the images are accurate, so the vertical and horizontal distance wires will be used to assess the scaling with the grid tool at the AFC workstation.

IQ7 – Treatment planning computer (TPS) volume accuracy

The Clarity QC phantom (Figure 41) has two high-contrast spherical inclusions of known diameter (15 mm and 30 mm) that can be used to assess the volume accuracy of both the ultrasound and CT scans. The spheres can be contoured at the AFC workstation and the volumes compared to the known volumes (1.77 cc and 14.14 cc respectively).

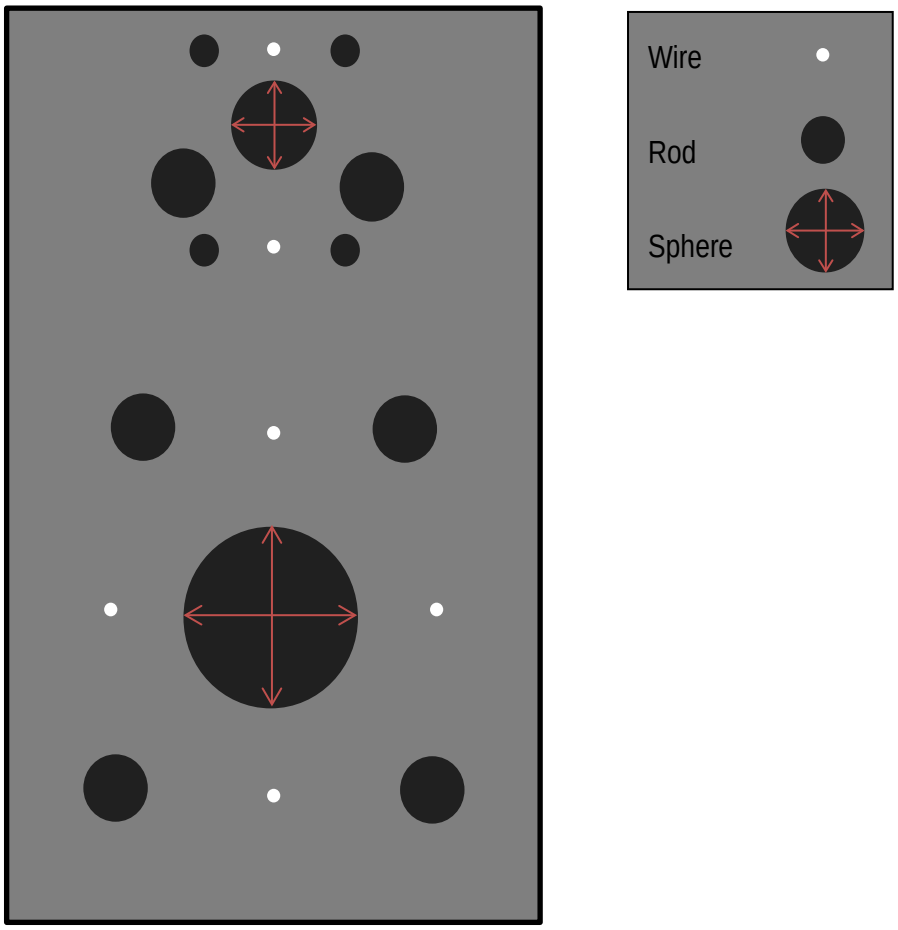

Figure 41: Transverse view of Clarity QC phantom showing internal structures (not to scale)

A.2 System integrity tests

Table 14 lists the tests recommended by TG-154 including image quality. Laser alignment won't be included in the list of supplementary tests as it is already a critical part of daily linac QC. Neither will daily positioning constancy be included as this is recommended by Elekta and hence it is assumed that this is already being performed. It involves the Clarity QC phantom, aligned to the room lasers, and a 3D ultrasound image acquired. The centroid position of the large sphere is determined by the software and compared to a calibration value with an action level of 1 mm.

To account for possible degradation of the phantom that might affect the QC results including sagging of the internal elements, Elekta recommends the phantom stability correction be performed every month. This involves a new CT scan of the phantom which is uploaded to the Clarity server

Clarity automatically analyses the CT images, calculating the positions of the internal structures relative to fiducial markers embedded in the outer housing of the phantom. This "phantom characterisation" is what is used by the software as the reference for the daily QC.

There are no physical knobs or switches to control the depth and gain; these are all embedded in the software so are very unlikely to malfunction. Therefore, this test has been retained in the list of supplementary tests but the frequency has been changed to monthly, forming part of the monthly physics QC tests. As for the daily IR camera warmup, the cameras for the Clarity system are never powered down, even when the linac and CT are, so they never require warming up. Finally, the phantom offset test is only necessary if Clarity is to be used in IGRT-mode, that is, the Clarity-determined shifts are to be used for pre-treatment patient positioning.

SI1 – Physical inspection

Ultrasound systems are susceptible to wear and tear due to the frequent handling of the transducer. Audits of diagnostic instruments [79, 80] have found a significant proportion of defective transducers, with nearly 40% showing an error in one study, and 8.4% with a break in the signal cable. The Clarity system also relies heavily on the integrity of the IR reflector arrays for positioning constancy. Therefore, a routine physical inspection of the IR reflectors and transducer cable for evidence of kinking or other damage is highly recommended.

SI2 – Depth and gain controls

Figure 42 shows the 8 image controls in the upper right corner of the acquisition interface. From top to bottom they are depth, pre-set dropdown list, overall image gain (i.e. brightness, c.f. window level), gamma (high gamma makes dark areas darker), dynamic range (c.f. window width) and near, middle and far-field gains. The controls will be tested monthly for functionality by a medical physicist.

SI3 – Positioning constancy

As described by TG-154, the monthly positioning constancy test includes the daily test described above, but is preceded by a recalibration of the isocentre position, or "Room Setup" in the Clarity parlance. The daily QC is performed first, following a routine check of the room lasers. This involves the Clarity QC phantom, which is carefully aligned to the room lasers via external etchings and the acquisition of a 3D US image of the internal structures of the phantom (Figure 41). The software automatically characterises the US images to find the positions of each of the structures. This US characterisation is then automatically registered to the CT characterisation described above to correlate the US structure positions to the location of the CT structures and thereby the fiducials found in the CT images and thereby the Clarity-measured position of the isocentre.

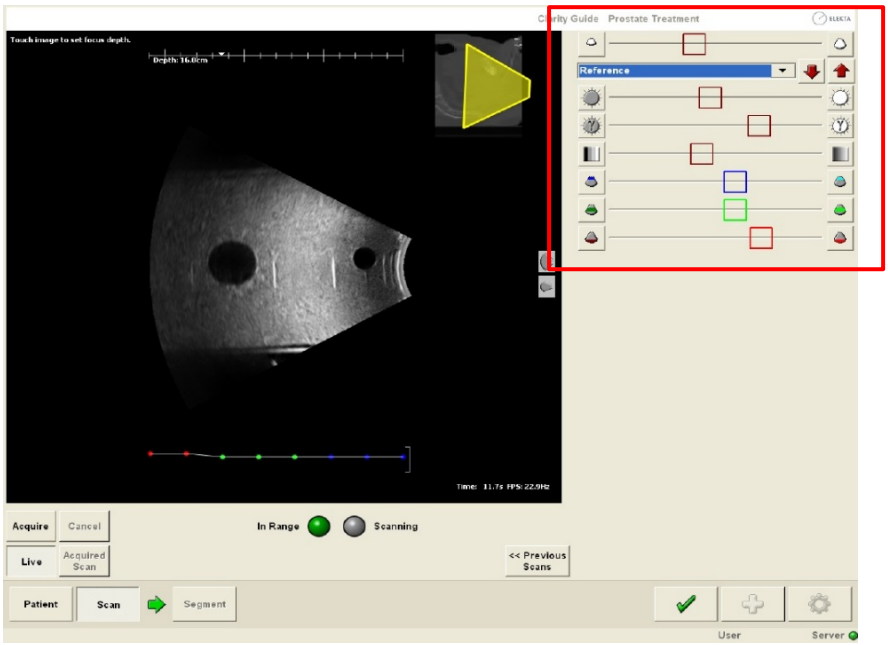

Figure 42: Clarity acquisition interface including imaging parameter controls

If the daily QC results in deviations of more than 0.5 mm in any direction the Room Setup calibration will be performed. This will reset all offsets to zero, redefining the location of the isocentre in the Clarity coordinate system. The daily QC will not be included in the list of supplementary tests because it is already prescribed by the manufacturer; However, while Elekta provides the built-in functionality to perform the Room Setup they do not prescribe a frequency. Furthermore, clinical experience has shown this to drift more than had been expected. Hence the monthly positioning constancy has been included in the supplementary QC list as a way of ensuring the calibration occurs when the action level is triggered.

As this item is intended to maintain the Clarity isocentre calibration, which is specific to each room in which Clarity is used, it will need to be performed on each linac and CT-Simulator every month.

SI4 – Laser offset (Optional)

In this test an offset is set in the lasers in the simulation room and the Clarity phantom aligned to the offset position. The phantom is then scanned by both CT and US and the datasets coregistered. The translations required to register the datasets should match the offsets in the simulation room lasers. This test is only relevant if moveable lasers are fitted in the simulation suite and are used for Clarity prostate simulation; therefore, it is important to confirm if laser offsets are routinely used during simulation. This is not the clinical practice at the author's facility so results of this test will not be reported below.

SI5 – Phantom offset test (Optional – Clarity IGRT mode only)

The Clarity phantom is initially positioned to the linac lasers and then offsets of several centimetres are introduced in all three axes. Clarity is then used to find the shifts necessary to re-centre the phantom and these shifts applied. According to TG-154 the phantom should return to within 2 mm of its starting position. As this test relates to the ability of the whole system – Clarity, linac software and hardware – to identify the necessary shifts and accurately apply them, it is only necessary if Clarity IGRT mode is to be used clinically. This, too, is not the clinical practice at the author's facility so results of this test will not be reported below.

SI6 – End-to-end testing (Optional – Clarity IGRT mode only)

In this annual or post-upgrade test, the Clarity QC phantom is subjected to the clinical patient workflow including simulation CT and reference US, registration and contouring, and positioning on the linac using the clinical IGRT method. It must be remembered that TG-154 is about US for IGRT, not intrafraction monitoring, so this test and the recommended tolerance only relate to the position of the phantom pre-treatment. If Clarity is not being used for IGRT then any pre-treatment differences will be zeroed out making this test redundant.

SI7 – tracking test

The task group reports do not deal with motion management, so it is necessary to include an additional test to cover the motion tracking functionality. The work covered in previous chapters has looked at the ability of the Clarity system to accurately track the target in 3D (Chapter 5) as well as the tracking latency (Chapter 6). It is noteworthy here that the latency testing did not require the ionisation chamber as part of the experimental setup and could have been done using the setup in Chapter 5.

These tests were extremely valuable for characterising the system as part of commissioning, however the experimental setup is far too onerous to justify performing them routinely. Therefore, it would be beneficial to devise a simpler test that can be performed routinely without adding significant time to the QC session. Three-dimensional tracking may be assessed using graph paper under the phantom and manual shifts for lateral motion, inserting and removing virtual/solid water of well-known thickness to raise and lower the phantom for vertical motion, and inserting and removing a gel bolus between the probe and phantom acoustic window while using the graph paper to measure longitudinal motion.

A.3 Combined supplementary test lists

Table 15 lists the combined supplementary monthly QC tests drawn from TG-128 and TG-154. Most of the image quality tests are to be performed in 2D mode only: this assumes that IQ8 confirmed similar results across imaging modes at commissioning. Table 16 lists the supplementary tests to be performed at commissioning and/or annually or following a system upgrade.

Table 15: List of supplementary monthly QC tests to be performed by QMP

ID	*Description*	*Imaging Mode*	*Phantom*	*Action Level*
SI1	Physical inspection	-	-	Physical damage found
SI2	US controls	2D	US QC	Functional
IQ1	Spatial resolution	4D	US QC	Baseline ±1 mm
IQ2	Low contrast detectability	2D	US QC	Baseline
IQ3	Sensitivity	2D	US QC	Baseline ±10 mm
IQ4	Uniformity / artefacts	2D	US QC	Consistent
IQ5	Grayscale visibility	2D	US QC	Baseline
IQ6	Scaling	3D	US QC	Axial: 2mm Lateral: 3mm Reconstructed: 3 mm
SI3	Positioning constancy (each linac/simulator each month)	3D	Clarity	>0.5 mm in any direction
SI4	Laser offset (optional)	3D	Clarity	2 mm
SI5	Phantom offset (optional)	3D	Clarity	2 mm

Table 16: List of supplementary annual QC and commissioning tests to be performed by QMP

ID	*Description*	*Mode*	*Phantom*	*Frequency*	*Action Level*
IQ7	TPS volume accuracy	3D	US QC	Commissioning	±5%
SI6	End-to-end (optional)	All	Clarity	Annually or after upgrade	2 mm displacement
SI7	Tracking accuracy	4D	Clarity	Annually or after upgrade	±1 mm

A.4 Data Acquisition

The Clarity workflow begins with a live 2D acquisition for positioning the probe, followed by the acquisition of the 3D reference image. At simulation this is all that is needed; however, for motion monitoring the workflow moves on to 4D acquisition. The image settings are modified during the live 2D acquisition and then are carried through to 3D and 4D imaging. The interface has a number of pre-programmed setting groups accessible in a drop-down list (Figure 42) which can then be modified as necessary using the slider bars. Baseline values for each of the image quality tests were acquired using the *Medium_Coarse* setting group (Figure 43), which refers to the medium focus depth and the coarse dynamic range (as opposed to "Smooth"). IQ2 and IQ3 required modification of the baseline scan settings in order to highlight the sensitive depth and visualise the deeper low contrast objects.

At the CT-simulator the probe and QC phantom were arranged as per Figure 7 and Figure 8 in Chapter 3, with the probe affixed to the baseplate, but with the QC phantom substituted for the Clarity phantom. The QC phantom was stood on its side so that the 2D imaging plane was perpendicular to the internal contrast objects, then phantom was moved laterally to align with the different elements within the QC phantom for each test. Scaling and spatial resolution were assessed with this setup, but then also assessed with the phantom rotated 90 degrees. This enabled these two items to also be assessed in the third dimension, in the direction of the transducer sweep. Two separate sessions were initiated, one for each phantom orientation, so that two reference datasets would be sent to the AFC workstation for further assessment.

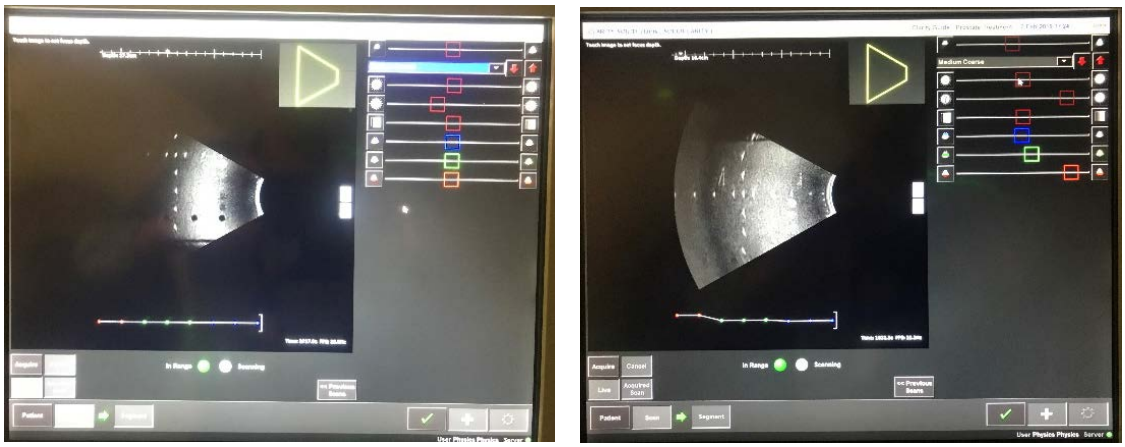

Figure 43: Medium_Coarse settings (left) and modified settings for sensitivity test (right)

At the AFC workstation the grid tool can be used to quickly assess the 3D reference images. For more precise measurement a registration session can be initiated in the software with the 3D US as the reference dataset, which will give access to the ruler tool. For 4D monitoring, only 3 orthogonal planar images are stored every 30 seconds for treatment review purposes; neither measuring tool can be used on these, however they are still useful for qualitative assessment of spatial resolution in the reconstructed 3rd dimension (i.e. direction of transducer sweep).

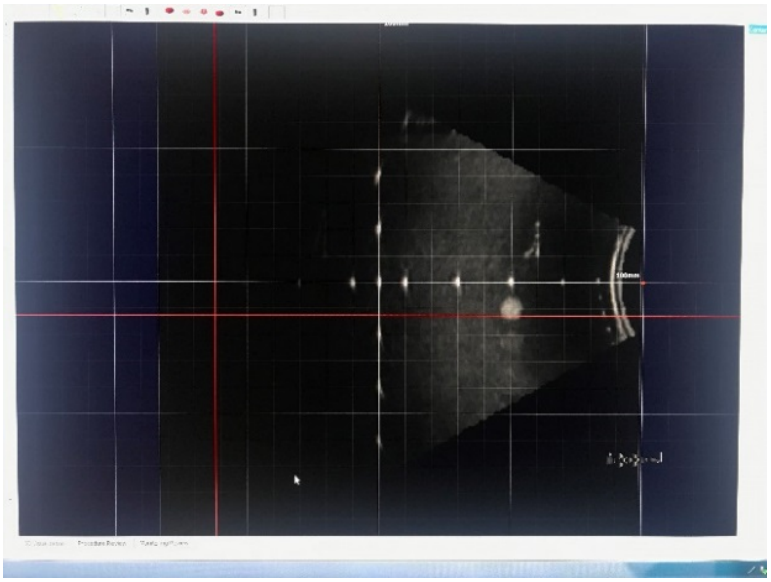

Figure 44: Axial and lateral scaling assessment at the AFC workstation using the grid tool

A.4 Baseline values

Only IQ1-7 and SI1-3 were conducted for this work, as the tests marked as optional are not relevant to the current clinical practice in the author's centre. Baseline values for the image quality tests are reported in Table 17. The physical inspection revealed no obvious damage, and the imaging controls were all found to be functional. The daily QC performed as part of SI3 revealed minor misalignment between the room lasers and the Clarity-calibrated 'isocentre' position, so the Room Setup was performed to remove the differences as per the manufacturers recommendations.

The spatial resolution in the reconstructed direction appears to be quite poor in comparison to the other two axes; however, it is heavily dependent upon the focus depth that has been chosen by the operator. This is because the beam profile in the 3rd dimension is shaped like that of a concave lens, with the narrowest point at the focal depth. The thickness of the voxels at a given depth depends on its axial position and the chosen focus depth. The result above might be reduced if

the focus depth were set to that of the axial-lateral resolution wires in the phantom (Figure 41), but the important thing for the QC tests is that it is always consistent.

The volume of the large sphere appeared 12.0% greater on CT (15.38 cc) than the calculated volume (14.14 cc), while it was 14.5% less than expected on US. Low contrast objects are known to appear smaller on US, and CT is known to produce larger volumes than US; so, it may not be reasonable to use the large anechoic sphere to assess the volume accuracy, given that the properties of a true prostate are not so dissimilar from its surroundings.

Table 17: Baseline image quality results

ID	*Description*	*Mode*	*Baseline*
IQ1	Spatial resolution	2D	Axial: 2-3 mm | Lateral: 1-2 mm
		4D	Axial: 1-2 mm | Lateral: 0.5-1 mm | Reconstructed: 3-4 mm
IQ2	Low contrast detectability	2D	5 contrast objects clearly discernible
IQ3	Sensitivity	2D	130-140 mm
IQ4	Uniformity / artefacts	2D	Pass
IQ5	Grayscale visibility	2D	5 grayscale objects clearly discernible; -3 dB barely visible
IQ6	Scaling (Figure 44)	3D	Axial: <1 mm | Lateral: <1 mm | Reconstructed: <1 mm
IQ7	TPS volume accuracy	3D	Large: 12.09 cc (calculated volume = 14.14 cc) Small: 1.80 cc (calculated volume = 1.77 cc)

Bibliography

1. Lachaine, M. and T. Falco, *Intrafractional prostate motion management with the clarity autoscan system.* MEDICAL PHYSICS, 2013. 1(1).
2. Abramowitz, M., et al., *Noninvasive real-time prostate tracking using a transperineal ultrasound approach.* International Journal of Radiation Oncology• Biology• Physics, 2012. 84(3): p. S133.
3. Yu, A.S., et al., *Intrafractional Tracking Accuracy of a Transperineal Ultrasound Image Guidance System for Prostate Radiotherapy.* Technology in Cancer Research & Treatment, 2017. 16(6): p. 1067-1078.
4. Han, B., et al., *Evaluation of transperineal ultrasound imaging as a potential solution for target tracking during hypofractionated radiotherapy for prostate cancer.* Radiation oncology (London, England), 2018. 13(1): p. 151-151.
5. Valier, H., *A History of Prostate Cancer*. Medicine and Biomedical Sciences in Modern History, ed. C.T.M. Worboys. 2016: Springer Nature.
6. Byrne, T.E., *A review of prostate motion with considerations for the treatment of prostate cancer.* Medical Dosimetry, 2005. 30(3): p. 155-161.
7. *NCI Dictionary of Cancer Terms*. 2019 [cited 2019 18/02/2019]; Available from: https://www.cancer.gov/publications/dictionaries/cancer-terms/def/image-guided-radiation-therapy.
8. Willoughby, T.R., et al., *Target localization and real-time tracking using the Calypso 4D localization system in patients with localized prostate cancer.* International Journal of Radiation Oncology*Biology*Physics, 2006. 65(2): p. 528-534.
9. Keall, P.J., et al., *Review of Real-Time 3-Dimensional Image Guided Radiation Therapy on Standard-Equipped Cancer Radiation Therapy Systems: Are We at the Tipping Point for the Era of Real-Time Radiation Therapy?* International Journal of Radiation Oncology*Biology*Physics, 2018. 102(4): p. 922-931.
10. Ten Haken, R., et al., *Treatment planning issues related to prostate movement in response to differential filling of the rectum and bladder.* International Journal of Radiation Oncology* Biology* Physics, 1991. 20(6): p. 1317-1324.
11. Crook, J.M., et al., *Prostate motion during standard radiotherapy as assessed by fiducial markers.* Radiotherapy and Oncology, 1995. 37(1): p. 35-42.
12. Forman, J.D., et al., *Evaluation of changes in the location and shape of the prostate and rectum during a seven week course of conformal radiotherapy.* International Journal of Radiation Oncology*Biology*Physics, 1993. 27: p. 222.
13. Ballhausen, H., et al., *Intra-fraction motion of the prostate is a random walk.* Physics in Medicine & Biology, 2015. 60(2): p. 549.
14. 83, I.R., *Prescribing, Recording, and Reporting Photon-Beam Intensity-Modulated Radiation Therapy (IMRT).* Journal of the International Commission on Radiation Units and Measurements, 2010. 10(1): p. NP-NP.
15. van Herk, M., et al., *The probability of correct target dosage: dose-population histograms for deriving treatment margins in radiotherapy.* International Journal of Radiation Oncology* Biology* Physics, 2000. 47(4): p. 1121-1135.
16. van Herk, M. *Errors and margins in radiotherapy*. in *Seminars in radiation oncology*. 2004. Elsevier.
17. Balter, J.M., et al., *Online repositioning during treatment of the prostate: a study of potential limits and gains.* International Journal of Radiation Oncology• Biology• Physics, 1993. 27(1): p. 137-143.
18. Sripadam, R., et al., *Rectal motion can reduce CTV coverage and increase rectal dose during prostate radiotherapy: A daily cone-beam CT study.* Radiotherapy and Oncology, 2009. 90(3): p. 312-317.
19. Zelefsky, M.J., et al., *High-dose intensity modulated radiation therapy for prostate cancer: early toxicity and biochemical outcome in 772 patients.* International Journal of Radiation Oncology*Biology*Physics, 2002. 53(5): p. 1111-1116.

20. Pawlowski, J.M., et al., *Reduction of Dose Delivered to Organs at Risk in Prostate Cancer Patients via Image-Guided Radiation Therapy.* International Journal of Radiation Oncology*Biology*Physics, 2010. 76(3): p. 924-934.

21. Ariyaratne, H., et al., *Image-guided radiotherapy for prostate cancer with cone beam CT: dosimetric effects of imaging frequency and PTV margin.* Radiotherapy and Oncology, 2016. 121(1): p. 103-108.

22. Zelefsky, M.J., et al., *Improved clinical outcomes with high-dose image guided radiotherapy compared with non-IGRT for the treatment of clinically localized prostate cancer.* International Journal of Radiation Oncology* Biology* Physics, 2012. 84(1): p. 125-129.

23. Crehange, G., et al., *Clinical impact of margin reduction on late toxicity and short-term biochemical control for patients treated with daily on-line image guided IMRT for prostate cancer.* Radiotherapy and Oncology, 2012. 103(2): p. 244-246.

24. Raziee, H., et al., *Improved outcomes with dose escalation in localized prostate cancer treated with precision image-guided radiotherapy.* Radiotherapy and Oncology, 2017. 123(3): p. 459-465.

25. Beltran, C., M.G. Herman, and B.J. Davis, *Planning target margin calculations for prostate radiotherapy based on intrafraction and interfraction motion using four localization methods.* International Journal of Radiation Oncology* Biology* Physics, 2008. 70(1): p. 289-295.

26. Li, J.S., et al., *Gains From Real-Time Tracking of Prostate Motion During External Beam Radiation Therapy.* International Journal of Radiation Oncology*Biology*Physics, 2009. 75(5): p. 1613-1620.

27. Litzenberg, D.W., et al., *Influence of intrafraction motion on margins for prostate radiotherapy.* International Journal of Radiation Oncology* Biology* Physics, 2006. 65(2): p. 548-553.

28. Pang, E.P.P., et al., *Analysis of intra-fraction prostate motion and derivation of duration-dependent margins for radiotherapy using real-time 4D ultrasound.* Physics and Imaging in Radiation Oncology, 2018. 5: p. 102-107.

29. Yartsev, S. and G. Bauman, *Target margins in radiotherapy of prostate cancer.* The British Journal of Radiology, 2016. 89(1067): p. 20160312.

30. Shah, A.P., et al., *Expanding the use of real-time electromagnetic tracking in radiation oncology.* Journal of Applied Clinical Medical Physics, 2011. 12(4): p. 34-49.

31. Lagendijk, J.J.W., et al., *MRI/linac integration.* Radiotherapy and Oncology, 2008. 86(1): p. 25-29.

32. Raaymakers, B.W., et al., *First patients treated with a 1.5 T MRI-Linac: clinical proof of concept of a high-precision, high-field MRI guided radiotherapy treatment.* Physics in Medicine & Biology, 2017. 62(23): p. L41.

33. Troels, B., et al., *Three-dimensional MRI-linac intra-fraction guidance using multiple orthogonal cine-MRI planes.* Physics in Medicine & Biology, 2013. 58(14): p. 4943.

34. Wallace, H., et al., *Autoscan Transperineal Ultrasound of the Pelvis for Prostate Gland Localization—A Feasibility Study.* International Journal of Radiation Oncology• Biology• Physics, 2012. 84(3): p. S373-S374.

35. Pang, E.P.P., et al., *Reduction of intra-fraction prostate motion – Determining optimal bladder volume and filling for prostate radiotherapy using daily 4D TPUS and CBCT.* Technical Innovations & Patient Support in Radiation Oncology, 2018. 5: p. 9-15.

36. Ophir, J., et al., *Elastography: A quantitative method for imaging the elasticity of biological tissues.* Ultrasonic Imaging, 1991. 13(2): p. 111-134.

37. Kwon, S.J. and M.K. Jeong, *Advances in ultrasound elasticity imaging.* Biomedical Engineering Letters, 2017. 7(2): p. 71-79.

38. Lattanzi, J., et al., *Ultrasound-Based Stereotactic Guidance in Prostate Cancer—Quantification of Organ Motion and Set-Up Errors in External Beam Radiation Therapy.* Computer Aided Surgery, 2000. 5(4): p. 289-295.

39. Tomé, W.A., et al., *Commissioning and quality assurance of an optically guided three-dimensional ultrasound target localization system for radiotherapy.* Medical Physics, 2002. 29(8): p. 1781-1788.

40. Bell, M.A.L., et al., *In vivo reproducibility of robotic probe placement for a novel ultrasound-guided radiation therapy system.* Journal of Medical Imaging, 2014. 1(2): p. 025001.

41. Salter, B.J., et al., *Evaluation of alignment error due to a speed artifact in stereotactic ultrasound image guidance.* Physics in Medicine & Biology, 2008. 53(23): p. N437.

42. Fontanarosa, D., S.v.d. Meer, and F. Verhaegen, *On the significance of density-induced speed of sound variations on US-guided radiotherapy.* Medical Physics, 2012. 39(10): p. 6316-6323.

43. Fontanarosa, D., et al., *Magnitude of speed of sound aberration corrections for ultrasound image guided radiotherapy for prostate and other anatomical sites.* Medical Physics, 2012. 39(8): p. 5286-5292.

44. Davide, F., et al., *A speed of sound aberration correction algorithm for curvilinear ultrasound transducers in ultrasound-based image-guided radiotherapy.* Physics in Medicine & Biology, 2013. 58(5): p. 1341.

45. Camps, S.M., et al., *The Use of Ultrasound Imaging in the External Beam Radiotherapy Workflow of Prostate Cancer Patients.* BioMed research international, 2018. 2018: p. 7569590-7569590.

46. Abramowitz, M.C., et al., *Noninvasive Real-Time Prostate Tracking Using a Transperineal Ultrasound: A Clinical Trial Comparison to RF Transponders With Visual Confirmation.* International Journal of Radiation Oncology • Biology • Physics, 2013. 87(2): p. S682.

47. Richardson, A.K. and P. Jacobs, *Intrafraction monitoring of prostate motion during radiotherapy using the Clarity Autoscan Transperineal Ultrasound (TPUS) system.* Radiography, 2017. 23(4): p. 310-313.

48. Grimwood, A., et al., *In Vivo Validation of Elekta's Clarity Autoscan for Ultrasound-based Intrafraction Motion Estimation of the Prostate During Radiation Therapy.* International Journal of Radiation Oncology*Biology*Physics, 2018.

49. AGENCY, I.A.E., *Strategies for the Management of Localized Prostate Cancer: A Guide for Radiation Oncologists*. IAEA Human Health Reports. 2014, Vienna: INTERNATIONAL ATOMIC ENERGY AGENCY.

50. Oldham, M., et al., *Cone-beam-CT guided radiation therapy: A model for on-line application.* Radiotherapy and Oncology, 2005. 75(3): p. 271.E1-271.E8.

51. Lattanzi, J., et al., *A comparison of daily CT localization to a daily ultrasound-based system in prostate cancer.* International Journal of Radiation Oncology* Biology* Physics, 1999. 43(4): p. 719-725.

52. Molloy, J.A., et al., *Quality assurance of US-guided external beam radiotherapy for prostate cancer: Report of AAPM Task Group 154.* Medical physics, 2011. 38(2): p. 857-871.

53. Robinson, D., et al., *An evaluation of the Clarity 3D ultrasound system for prostate localization.* Journal of Applied Clinical Medical Physics, 2012. 13(4): p. 100-112.

54. Fargier-Voiron, M., et al., *Evaluation of a new transperineal ultrasound probe for inter-fraction image-guidance for definitive and post-operative prostate cancer radiotherapy.* Physica Medica: European Journal of Medical Physics, 2016. 32(3): p. 499-505.

55. Zaragori, T., et al., *8. Monitoring of prostate cancer with a transperineal ultrasound probe: Impact on treatment margins.* Physica Medica: European Journal of Medical Physics, 2017. 44: p. 5.

56. Trivedi, A., et al., *Development of 3-dimensional transperineal ultrasound for image guided radiation therapy of the prostate: Early evaluations of feasibility and use for inter-and intrafractional prostate localization.* Practical radiation oncology, 2017. 7(1): p. e27-e33.

57. Li, H.S., et al., *Dosimetric consequences of intrafraction prostate motion.* International Journal of Radiation Oncology* Biology* Physics, 2008. 71(3): p. 801-812.

58. Langen, K.M., et al., *Correlation between dosimetric effect and intrafraction motion during prostate treatments delivered with helical tomotherapy.* Physics in Medicine & Biology, 2008. 53(24): p. 7073.

59. Langen, K.M., et al., *Dosimetric effect of prostate motion during helical tomotherapy.* International Journal of Radiation Oncology* Biology* Physics, 2009. 74(4): p. 1134-1142.

60. Langen, K.M., et al., *The dosimetric effect of intrafraction prostate motion on step-and-shoot intensity-modulated radiation therapy plans: Magnitude, correlation with motion parameters, and comparison with*

helical tomotherapy plans. International Journal of Radiation Oncology* Biology* Physics, 2012. 84(5): p. 1220-1225.

61. Adamson, J., Q. Wu, and D. Yan, *Dosimetric effect of intrafraction motion and residual setup error for hypofractionated prostate intensity-modulated radiotherapy with online cone beam computed tomography image guidance.* International Journal of Radiation Oncology* Biology* Physics, 2011. 80(2): p. 453-461.

62. Azcona, J.D., et al., *Assessing the Dosimetric Impact of Real-Time Prostate Motion During Volumetric Modulated Arc Therapy.* International Journal of Radiation Oncology*Biology*Physics, 2014. 88(5): p. 1167-1174.

63. Jermoumi, M., et al., *Does gated beam delivery impact delivery accuracy on an Elekta linac?* Journal of Applied Clinical Medical Physics, 2017. 18(1): p. 90-95.

64. Goodsitt, M.M., et al., *Real-time B-mode ultrasound quality control test procedures. Report of AAPM Ultrasound Task Group No. 1.* Medical physics, 1998. 25(8): p. 1385-1406.

65. Pfeiffer, D., et al., *AAPM Task Group 128: Quality assurance tests for prostate brachytherapy ultrasound systems.* Medical Physics, 2008. 35(12): p. 5471-5489.

66. Hecht, E., *Optics, 4th.* International edition, Addison-Wesley, San Francisco, 2002. 3: p. 2.

67. Marczak, W., *Water as a standard in the measurements of speed of sound in liquids.* the Journal of the Acoustical Society of America, 1997. 102(5): p. 2776-2779.

68. Smith, A. and A. Lawson, *The velocity of sound in water as a function of temperature and pressure.* The journal of chemical physics, 1954. 22(3): p. 351-359.

69. *Speed of Sound in Water*. Engineering Toolbox [online] 2004 13/9/2018]; Available from: https://www.engineeringtoolbox.com/sound-speed-water-d_598.html.

70. *Poly(methyl methacrylate)*. Wikipedia contributors. [online] 10 September 2018 16/09/2018]; Available from: https://en.wikipedia.org/wiki/Poly(methyl_methacrylate).

71. Christman, D.R., *Dynamic properties of poly (methylmethacrylate)(PMMA)(Plexiglas)*. 1972, GENERAL MOTORS TECHNICAL CENTER WARREN MI MATERIALS AND STRUCTURES LAB.

72. Hartmann, B. and J. Jarzynski, *Immersion Apparatus for Ultrasonic Measurements*, W.O. NAVAL ORDNANCE LABORATORY, MD, Editor. 1972.

73. Carlson, J.E., et al. *Frequency and temperature dependence of acoustic properties of polymers used in pulse-echo systems*. in *IEEE Symposium on Ultrasonics, 2003*. 2003.

74. Xia, W., et al., *A new acoustic lens material for large area detectors in photoacoustic breast tomography.* Photoacoustics, 2013. 1(2): p. 9-18.

75. *Ultrasonic Sound Velocity Table*. Class Instrumentation Ltd [online] 2013 16/09/2018]; Available from: http://www.classltd.com/sound_velocity_table.html.

76. *Sound Speeds in Water, Liquid and Materials*. [online] 2018 2018 16/09/2018]; Available from: http://www.rshydro.co.uk/sound-speeds/.

77. Khan, F.M., *The Physics of Radiation Therapy*. 2010: Lippincott Williams & Wilkins.

78. Molloy, J.A., et al., *Quality assurance of U.S.-guided external beam radiotherapy for prostate cancer: Report of AAPM Task Group 154.* Medical Physics, 2011. 38(2): p. 857-871.

79. Mårtensson, M., et al., *High incidence of defective ultrasound transducers in use in routine clinical practice.* European Journal of Echocardiography, 2009. 10(3): p. 389-394.

80. Sipilä, O., V. Mannila, and E. Vartiainen, *Quality assurance in diagnostic ultrasound.* European Journal of Radiology, 2011. 80(2): p. 519-525.